Solid-State NMR: Investigations of Biomolecular Structure

Elizabeth April Louie

A dissertation
submitted in partial fulfillment of the
requirements for the degree of

Doctor of Philosophy

University of Washington

2005

Program Authorized to Offer Degree:
Department of Chemistry

INFORMATION TO USERS

The quality of this reproduction is dependent upon the quality of the copy submitted. Broken or indistinct print, colored or poor quality illustrations and photographs, print bleed-through, substandard margins, and improper alignment can adversely affect reproduction.

In the unlikely event that the author did not send a complete manuscript and there are missing pages, these will be noted. Also, if unauthorized copyright material had to be removed, a note will indicate the deletion.

ProQuest Information and Learning Company
300 North Zeeb Road
P.O. Box 1346
Ann Arbor, MI 48106-1346

University of Washington
Graduate School

This is to certify that I have examined this copy of a doctoral dissertation by

Elizabeth April Louie

and have found that it is complete and satisfactory in all respects,
and that any and all revisions required by the final
examining committee have been made.

Chair of Supervisory Committee:

Gary P. Drobny

Reading Committee:

Gary P. Drobny

Bruce H. Robinson

Philip J. Reid

Date: September 29, 2005

In presenting this dissertation in partial fulfillment of the requirements for the doctoral degree at the University of Washington, I agree that the Library shall make its copies freely available for inspection. I further agree that extensive copying of the dissertation is allowable only for scholarly purposes, consistent with "fair use" as prescribed in the U.S. Copyright Law. Requests for copying or reproduction of this dissertation may be referred to Proquest Information and Learning, 300 North Zeeb Road, Ann Arbor, MI 48106-1346, to whom the author has granted "the right to reproduce and sell (a) copies of the manuscript in microform and/or (b) printed copies of the manuscript from microform."

Signature 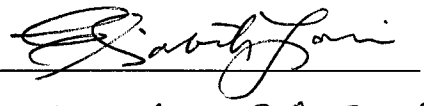

Date September 29, 2005

University of Washington

Abstract

Solid-State NMR Investigations of the Structure of Biomolecules

Elizabeth April Louie

Chair of the Supervisory Committee:
Professor Gary P. Drobny
Department of Chemistry

Solid-state nuclear magnetic resonance methods were used to characterize the structure of biological molecules in lyophilized and hydrated environments with and without the presence of other molecules such as drugs, lipids, and surfaces. Revealing the structure of biomolecules by mimicking its natural environment, information about their potential function may be realized. Several small model compounds and double-stranded DNAs were synthesized with an unique phosphorous label and either a single fluorine or trifluoromethyl label. The distance between the phosphorous and fluorine(s) where measured using the heteronuclear REDOR experiment to determine enhancement of dipolar coupling due to a trifluoromethyl group as compared to a single fluorine group. Due to increased dephasing of the trifluoromethyl group it is a promising labeling method to determine drug and biological molecule interactions. In using methods to measure distances between atoms, changes in the secondary

structure of a dsDNA in the presence of an antibiotic drug can be monitored. The secondary structure of peptides were also determined but with implementing double quantum DRAWS experiments. These homonuclear dipolar recoupling experiments were implemented to determine torsion (ϕ and ψ) angles of a peptide in a lipid bilayer environment as well as peptides adsorbed on a charged surface. The secondary structure of an amphipathic peptide was compared when it was covalently attached to a resin versus adsorbed to a charged surface.

Table of Contents

List of Figures

List of Tables

Preface

Solid-state nuclear magnetic resonance is a spectroscopic technique able to determine structure of biological molecules in their natural environments. The functions of biological molecules such as nucleic acids and proteins can be interpreted by determining their structures and their interactions with other molecules. Biological molecules do not work in isolation but are surrounded by other molecules. The understanding of how biological molecules work in concert is of great importance in the field of drug discovery, biomaterials, and analytical molecular isolation. This dissertation illustrates the usefulness of solid-state NMR as a technique to help solve biological structures in various environments.

Acknowledgements

I would like to express my gratitude to my graduate advisor, Dr. Gary P. Drobny, for the opportunity to work in his laboratory. His inspiration, understanding, patience, and expertise added considerably to my graduate experience. I would like to thank my committee members, Dr. Philip J. Reid, Dr. Bruce H. Robinson, and Dr. D. Michael Heinekey for the assistance they provided to the research projects. I would like to thank Dr. Brian J. Reid and Dr. Kevin E. Conley for their attendance to my general and final examinations, respectively. I would also like to thank our collaborators Dr. Snorri Th. Sigurdsson and Dr. Patick S. Stayton for expertise in their fields and the merging of scientific ideas. I wish to thank Dr. J. Michael Schurr for all his fruitful discussions. I would like to thank the post-doctoral fellows that I worked with in the Drobny Lab, Dr. Matthew E. Merritt, Dr. Joanna R. Long, and Dr. Myriam L. Cotten, who guided me through my various research projects. In addition, I would like to thank the past and present Drobny Group members: Dr. Mary Hatcher, Dr. John A. Stringer, Dr. Totte Karlsson, Dr. James Gibson, Dr. Gil Goobes, Dr. Rivka Goobes, Dr. Wendy Shaw, Dr. Gary Meints, Dr. Nathan Oyler, Dr. Karen Lo, Jennifer Popham, Gregory L. Olsen, Vinodh Raghunathan, Paul A. Miller, Zahra Shajani and Debrorah Chang for all their help, daily interactions, and advice.

I would like to thank Dr. Bethany Barham and Dr. Penny Rowe for their comradery during our graduate education and their continual friendship.

I would also like to thank my family for the support they provided me throughout the course of my life. I am grateful for their encouragement to pursue my passions and believe in me as they are my greatest mentors: my mother, sister, and brother, Lily, Jackie and Tony, respectively.

In conclusion, I recognize that this research would not have been possible without the financial assistance of the NIH, NSF, and the University of Washington Chemistry Department.

Dedication

To my loving mother and the memory of my father

Introduction

In the last several decades, solid-state nuclear magnetic resonance (NMR) spectroscopy has experienced significant advances due to the need to study biological samples that can not be well characterized in forms other than the solid state. When studying macromolecules (oligonucleotides, polymers, or proteins), it is not always possible to obtain a crystalline form for characterization by X-ray crystallography and sample solubility may preclude solution studies. Also, the structure of membrane bound proteins may be better characterized using solid state NMR techniques than solution state NMR. Solid-state NMR does not rely on rapid molecular orientation for line narrowing whereas solution state NMR methods are hampered by the slow correlation times of lipids. Solid state NMR is a valuable tool that can provide important structural information without limits imposed by molecular weight and can be applied to crystalline, microcrystalline, and amorphous systems as well as hydrated and unhydrated forms.

This dissertation presents three projects applying solid state NMR to biological systems: i) measurement of internuclear distances in nucleic acids utilizing a trifluoromethyl group, ii) measuring torsion angles to determine the secondary structure of membrane proteins, and iii) identifying changes in secondary structure of an amphipathic peptide adsorbed to a charged surface.

Chapter 1: Biological Aspects

1.1 Biomolecular Structure and Function

By determining structural information of biomacromolecules (DNA, RNA, and proteins), their corresponding biological functions can be rationalized through the knowledge of the molecules three-dimensional structure. Detailed insight into the structural basis of nucleic acid and protein interactions can provide a more reliable platform for rational drug design, the engineering of novel protein functions, and biomaterials.

1.2 Nucleic Acids

DNA, a carrier of genetic information, is responsible for the transmission, expression, and conservation of genetic information. With the fiber diffraction patterns provided by Rosalind Franklin and Maurice Wilkins (1953) and the base complimentarity observed by Chargaff (1950), the double-helical structure of DNA was presented by Watson and Crick in 1953. Thus, over the years, the understanding of the complexity of DNA structure has grown. DNA is more than a monotonously uniform helix and is a dynamic molecule with variable helical structures as evidenced by solution NMR studies.

Even though the outer surface of DNA is a monotonous phosphate backbone protecting the atoms of the bases from environmental chemical modifications, proteins can recognize general structural features of DNA, such as the grooves of DNA. Due to the variability of DNA secondary structures, proteins recognize these structural changes and thus, play an important role with DNA replication, transcription, condensation, and modification.

Small molecules, drugs or ligands have been discovered to associate with DNA or disrupt the synthesis of DNA beyond repair. One such discovery is the chemotherapy agent cisplatin. Another anti-neoplastic agent is etoposide which contributes to the platinum-DNA protein complex and synergystically reinforces the activity of cisplatin. By determining the structure of DNA complexes with drugs, peptides or proteins, and molecules that bind DNA can reveal information regarding mechanism of action.

The standard B-form of DNA has two distinct grooves, major and minor, as shown in Figure 1.1. Small antibiotic or anti-cancer drugs are known to interact with DNA and it has been found that such small ligands such as distamycin, Hoechst 33258 and netropsin Figure 1.2 bind to the minor groove of DNA with AT rich regions. Minor groove binders inhibit the sequence selective binding of various transcription factors to DNA and thus significant efforts [1-3] have been made to design small molecules with structural and chemical characteristics to recognize the features of DNA and bind with specificity.

The binding of small ligands to DNA and proteins differ greatly. Popular models of binding such as lock and key, induced fit [4] have explained protein/enzyme-drug binding as well as the role of hydrophobic effects. However, the binding models of proteins are not sufficient to explain the interactions of DNA-drug systems since DNA does not per se have a formal active site, unlike enzymes. In essence there are two principally different modes that drugs bind non-covalently to DNA which are groove binding and intercalation. A typical minor groove binder possesses a crescent shape very similar to the shape of the groove and binding is facilitated by van der Waals interactions. Hydrogen bonding of the drugs to the bases bind particularly to N3 of adenine and O2 of thymine, thus most minor groove binders bind to DNA of

A/T rich sequences. Thus, by identifying structural features of DNA binding properties and characteristics can contribute to the understanding of DNA-drug recognition.

1.3 Proteins

The diversity of the biological functions in proteins is due to the various combinations and sequences that the same 20 amino acids can build. In addition, proteins vary greatly in size from 50 to 25,000 residues. The functional properties of proteins can be best understood when the three dimensional structure is known. Knowing the amino acid sequence does not provide adequate information to draw conclusions about a protein's structure and function unless comparisons can be made between it and a protein of known structure with a similar sequence.

Proteins can exist in solution or be associated with membranes. Associated membrane proteins such as integral membrane proteins are immersed in the membrane bilayer with some or none of the polypeptide chain exposed to the aqueous sides of the membrane bilayer. Membrane proteins mediate some of the most important functions carried out by the cell. These functions, such as intracellular communication, signal transduction across the membrane bilayer, secretion of toxins, and transport of ions and nutrients, make them important potential drug targets.

The difficulty in determining the structure of membrane proteins is mainly due to the lipids being necessarily bound to the proteins non-polar surfaces and thus, the membrane proteins do not readily form three dimensional crystals [5]. Knowledge of the structure of membrane proteins is a priority for understanding their functional mechanisms.

1.4 Biomaterials

Biomaterial science comprises a growing field in the aid of designing materials to be devices that are not of a biological origin. After implantation of a device in a living system, proteins have been observed on biomaterial surfaces within less than a second [6]. Thus, adsorbed proteins play a role in the biological response to biomaterials.

Protein adsorption occurs before cells reach the surface of the biomaterial device. So, cells do not come in contact with the surface but the layer of proteins adsorbed to the device surface. Cells react specifically to proteins and thus controls the events of the bioreaction sequences to follow to the implant. The biological responses that can impair the usefulness of implants include clotting of blood and the foreign body reaction.

Interactions of proteins with surfaces are studied to understand the binding of the protein to the surface and to decipher or predict adsorption patterns. As proteins bind to biomaterial surfaces, it has been generally accepted that the proteins denature and thus lose their functionality.

1.5 Biological Structure Determination Methods

The present methods used to study biomolecular structure include but are not limited to X-ray crystallography, neutron scattering, solution-state nuclear magnetic resonance (NMR), electron paramagnetic resonance (EPR), and fluorescence resonance transfer (FRET).

X-ray crystallography, neutron scattering, and solution state NMR have found the most use in solving structural problems. Scattering techniques are of limited use for amorphous systems, and for large macromolecular systems it is difficult to obtain high quality crystals. Solution state NMR studies are problematic for high molecular weight systems because of limited solubilities

and spectral crowding. Other techniques include electron paramagnetic resonance (EPR) and fluorescence energy transfer (FRET) which can measure long-range distances between molecules however, spin and fluorescent labels, respectively, must be incorporated and dilute solutions are necessary to ensure intra-molecular measurements do not interfere.

Solid-state NMR is a complementary technique to the ones described above in determining the structure of biological molecules. The aspects of solid-state NMR that differ from the other techniques are the various environments and forms in which the molecules may be studied. Solid-state NMR is capable of probing hydrated as well as dry samples along with heterogeneous samples and thus has great versatility.

1.6 Biological Applications of Solid-State NMR

Solid-state NMR is being recognized for its utility in many applications in a wide range of biological systems. The strength of the technique is in its application to macromolecular complexes, to yield both structural and dynamic information in systems such as nucleic acids, ligand receptor interactions, membrane bound peptides and proteins, enzyme reaction mechanisms, protein structures, and biological surface interactions.

This dissertation will focus on several of the above biological applications using solid-state NMR as applied to structure determination of nucleic acids, a membrane bound peptide, and peptide adsorbed to surface.

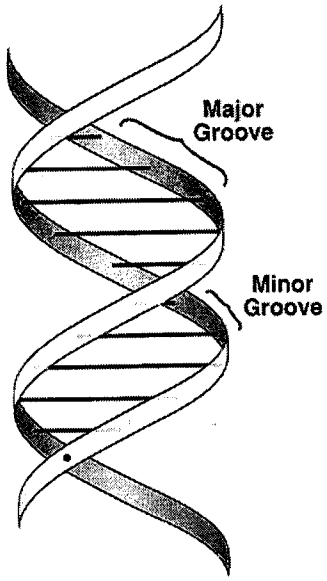

Figure 1.1 Standard B-form DNA showing major and minor groove (adapted from [7]).

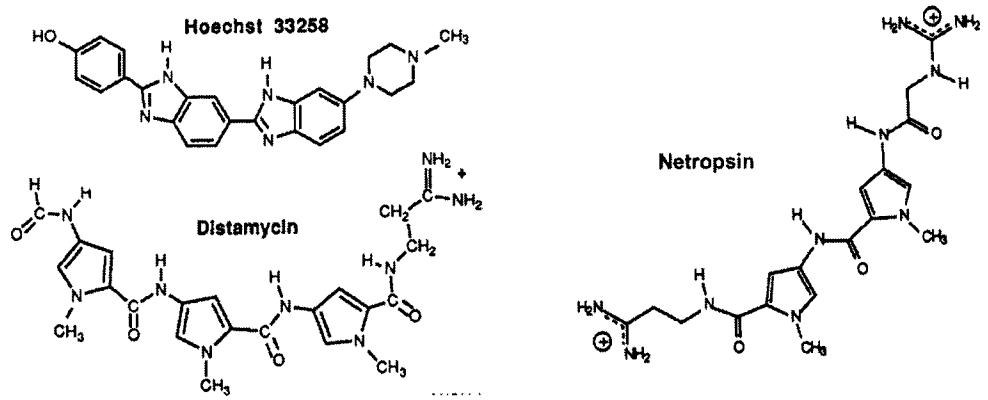

Figure 1.2 Structures of minor groove binders: Hoechst 33258, distamycin, and netropsin.

Chapter 2: Brief Description of Solid-State NMR

2.1 Introduction

In 1946, the NMR phenomenon was discovered by two different groups, Bloch, Hansen, and Packard (Stanford University) and Purcell, Torey, and Pound (Harvard University). [8,9] In 1952 Bloch and Purcell were awarded the nobel prize for discovering that when nuclei in a strong magnetic field are exposed to radiofrequency (rf) electromagnetic radiation, nuclei of the sample absorb energy at specific frequencies and the absorption of energy leads to an NMR signal [10]. Even though the NMR signals are relatively weak, NMR is able to investigate materials and living systems without significantly disturbing them and thus, yield detailed information in a noninvasive manner.

Nuclear magnetic resonance (NMR) is a versatile spectroscopic tool. It has become an essential analytical and structural technique in chemistry, molecular biology, biochemistry, physiology, and medicine. There have been applications in fields as diverse as archeology, oil prospecting, and veterinary science. NMR also plays a large role in the medical community and it is used as a diagnostic tool that is called Magnetic Resonance Imaging, MRI. Research is also being done on other clinical applications such as MRS (Magnetic Resonance Spectroscopy) and MRSI (Magnetic Resonance Spectroscopy Imaging) to detect levels of metabolites in a noninvasive manner. Few areas of scientific endeavor remain untouched by NMR.

2.2. The Nuclear Magnetic Resonance Phenomenon

Of the various phenomena important to NMR, the two of particular importance are the Zeeman effect and the existence of nuclear moments. At the end of the last century, Zeeman first observed the strange behavior of certain

nuclei subjected to a strong magnetic field which is now called the "Zeeman effect." In 1924 Pauli proposed that atomic nuclei may posses an intrinsic angular momentum (spin) and, parallel to its orientation, a magnetic moment. Thus, the spin angular momentum confers a magnetic moment on the nucleus, and therefore, it shows a given energy in a magnetic field. When the nuclear spin is placed in a magnetic field, it has energy that varies with orientation to the field. The NMR absorption is a consequence of transitions between the energy levels stimulated by applied radiofrequency radiation.

2.2.1 NMR Interactions

In order to understand solid-state NMR, there needs to be a brief introduction to the Hamiltonians that describe the interactions which the nuclear spins experience. The Hamiltonian is an operator that describes the energy of a system. The interactions present are commonly separated into two types, internal and external,

$$H = H_{ext} + H_{int} \tag{2.1}$$

The external interactions involve perturbations resulting from fields originating outside the sample, such as the applied static field (H_z) and applied radiofrequency (rf) field (H_{rf})

$$H_{ext} = H_Z + H_{rf} \tag{2.2}$$

H_Z also known as the Zeeman Hamiltonian describes the energy of a spin when placed into a magnetic field, $\vec{B}_0$. Thus H_Z can be written as

$$H_Z = -\gamma_I \hbar \vec{B}_0 I_Z = -\omega_0 I_z \tag{2.3}$$

where, ω_0 is the Larmor frequency, $\hbar$ is Planck's constant, γ is the gyromagnetic ratio and I_z is the spin angular momentum along the z-axis. The eigenvalues of

the Zeeman Hamiltonian are $E \pm m\gamma\hbar B_0$, where m equals *I, I-1,....-I.* When I = ½ as in a spin-1/2 nuclei, *E* can result in two possible energy levels ($E = \pm \frac{1}{2}\gamma\hbar B_0$) or eigenstates. These two energy eigenstates can be described as the $|\uparrow\rangle$ and $\langle\downarrow|$ basis sets. These basis sets are the low and high energy states that correspond to the two particular orientations of the spin's magnetic moment relative to the static field. For a spin-1/2 nucleus, the energy level diagram under the Zeeman interaction is depicted in Figure 2.1.

Internal interactions are from the interaction of the nucleus to fields generated within the sample such as the chemical shift anisotropy (CSA), dipolar (DD), quadrupolar (Q), and J coupling (J) interactions.

$$H_{int} = H_{CSA} + H_{DD} + H_Q + H_J \tag{2.4}$$

The quadrupolar interaction pertains to nuclei with a spin quantum number greater than ½ and thus is not relevant to the nuclei in this study which are spin ½ nuclei (^{31}P, ^{19}F, ^{13}C). J coupling describes the interaction between a spin and another spin via through bond coupling. The J coupling interaction will be neglected here because in solids it is typically much smaller than the interaction of interest. The CSA interaction Hamiltonian is

$$H_{CSA} = -\gamma\hbar\mathbf{B}_0 \bullet \boldsymbol{\sigma} \bullet \mathbf{I} \tag{2.5}$$

where $\boldsymbol{\sigma}$ is the chemical shift tensor, **I** is the spin angular momentum operator, γ is the gyromagnetic ratio of the spin, and $\hbar$ is Planck's constant. The spherical coordinate description of the chemical shift Hamiltonian is

$$H_{CSA} = \omega_0 I_Z[\sigma_{iso} + \frac{1}{2}(3\cos^2\theta - 1)(\sigma_{33} - \sigma_{iso})] \tag{2.6}$$

where θ is the angle of the sample with respect to the magnetic field and ω_0 is the Larmor frequency. The first term of Equation 2.6 corresponds to the isotropic chemical shift and the second term is due to the anisotropic interactions with the field. In this study, one interaction of interest is the heteronuclear dipolar interaction. The dipolar interaction expressed in spherical coordinates is

$$H_{DD} = -\frac{\hbar\gamma_S\gamma_I}{r^3}(1-3\cos^2\theta)I_Z S_Z . \tag{2.7}$$

Another interaction of interest is for the case when $I = S$ (the homonuclear case), the homonuclear dipolar interaction in the MAS NMR experiment is

$$H_{DD} = -\frac{\hbar\gamma_S\gamma_I}{r^3}(1-3\cos^2\theta)(3I_Z S_Z - \boldsymbol{I}\bullet\boldsymbol{S}) . \tag{2.8}$$

2.3. Practical Aspects

In the very early days of NMR, solid-state NMR was just as popular as liquid-state NMR because the relatively inhomogeneous magnets then available showed inherently broad NMR lines in solids but not the narrow lines known to exist in liquids. With the discovery of the chemical shift interaction and the importance of this tool to elucidate chemical structure, liquid-state studies took precedence because the lines where sharp enough to reveal chemical structure information. Due to the broad resonances observed in solids, one might regard the NMR of solids as not helpful in obtaining structural information. Therefore, the development of NMR spectroscopy in solids has been much slower than that of liquids due to difficulties associated with the immobility of the nuclei in solids. However, the broad NMR signals from solid samples did not discourage scientists from discovering methods to attain narrow lines in solid state spectra, in order to obtain unique chemical information.

2.3.1. The Broad Lines of Solids

The major causes of the broad spectrum in solid-state NMR are anisotropic interactions, such as the dipolar coupling and the chemical shift anisotropy. Dipolar couplings are due to the direct through-space coupling interactions between two nuclei. In solids, the dipolar couplings are not averaged to zero by molecular tumbling as in isotropic liquids. The resulting effect are very broad resonances, often tens of kHz wide.

Another cause of line broadening is chemical shift anisotropy. The chemical shift of a nucleus depends on the orientation of the molecule with respect to the magnetic field, B_0, such that the effective field, B_{eff}, at the nucleus is:

$$B_{eff} = B_0 - \sigma B_0, \tag{2.9}$$

where σ is the chemical shift tensor. The chemical shift tensor is a second rank tensor and is characterized by the three principal elements, σ_{11}, σ_{22}, σ_{33}. In the gas or liquid phase, due to rapid, isotropic, molecular motion, a nucleus is subjected to an average value of σ, $\bar{\sigma}$, the isotropic chemical shift, which is represented by the trace of the tensor such that

$$\bar{\sigma} = \frac{1}{3} Tr(\sigma) = \frac{1}{3}(\sigma_{11} + \sigma_{22} + \sigma_{33}) \tag{2.10}$$

In general, $\sigma_{11} \neq \sigma_{22} \neq \sigma_{33}$. In solutions, only the isotropic part of the tensor survives. In solids, the effect of the chemical shift anisotropy (CSA) is not averaged out by isotropic molecular tumbling and leads to line broadening of thousands of Hz.

2.3.2 Line Narrowing Techniques

NMR spectra of solids can be very broad. By using a combination of techniques, such as magic angle spinning, cross polarization and decoupling dipolar interactions, more narrow lines are possible.

2.3.2.1 Magic-Angle Spinning (MAS)

In solution NMR, the rapid isotropic motion averages dipolar interactions and chemical shift anisotropy to zero, allowing the observation of sharp lines at the isotropic chemical shift. In solid-state NMR, both the dipolar couplings and the CSA contain an angular dependence of the form $3\cos^2\theta - 1$ which are shown in the Hamiltonian equations of 2.6-2.8. By making use of the solution to the expression $(3\cos^2 \theta - 1) = 0$, where $\theta = 54.7°$, and setting the spinning axis to this magic angle of 54.7°, the rapid rotation at this angle successfully averages the second rank tensor components of the CSA and dipole-dipole interactions.

Spinning a sample at the magic angle, with respect to the main magnetic field, B_0, is known as magic-angle spinning (MAS). In 1958, Andrew and co-workers [11] and Lowe [12] showed that high-speed spinning of the sample at the magic angle could be an effective tool for averaging out dipolar broadening. In addition to MAS, there are other experimental techniques that have been employed and/or combined to provide line-narrowing methods in solids such as increasing the spinning rotation rate, decoupling dipolar coupling interactions, and multi-pulse methods.

The breadth of the CSA is often a few kHz and many MAS experiments can be conducted using rotation frequencies of about 20 kHz. When the CSA is larger than the spinning frequency in an experiment, a set of sharp lines spaced at the rotation frequency are observed. As a result, the intensity of the individual

components maps the amplitude of the CSA pattern at that spinning frequency and the isotropic chemical shift is usually at the maximum of the CSA pattern. Figure 2.2 illustrates that for a change in rotation frequency, the spinning side bands are separated by the spinning speed. A high resolution spectrum can be acquired if the interactions are smaller than the spinning speed.

In addition, magic-angle spinning sharpens dipolar coupled lines if the rotation rate is greater than the linewidths. The dipolar couplings will be averaged to zero in a similar fashion as molecules tumble in solution. However, for some samples, the ^{13}C lines are too broad to permit MAS alone to generate useful sharpened lines because samples must spin fast enough to average the large dipolar interactions. For instance, dipolar couplings between ^{13}C and ^{1}H are 20 kHz or more, and so the rotation must be fast enough to remove them completely. In practice, the rotation rate is limited by the mechanical strength of the sample container and the rotor speed.

2.3.2.2 Cross Polarization (CP)

Thus far, in order to obtain resolved spectra, magic angle spinning is used to eliminate the anisotropic part of the chemical shift. A strong heteronuclear decoupling field is used during acquisition in order to eliminate the broadening due to the dipolar coupling with protons. In addition, to enhance sensitivity, cross polarization (CP) is used to take advantage of the coupling of the low γ rare S spins (e.g. ^{13}C) with the high-γ I spins (e.g. ^{1}H). This technique relies on the polarization transfer from the abundant spins, for example ^{1}H, to the rare spins like ^{13}C through matching the B_1 rf field of the ^{1}H's and ^{13}C's. The matching of the rotating frame precession frequencies is referred to as the Hartman-Hahn match condition which is:

$$\gamma_H(B_1)_H = \gamma_C(B_1)_C \pm \nu \cdot \text{spinning speed} \qquad (2.11)$$

where $\nu = 1, 2, 3...$ and B_{1H} and B_{1C} are the rotating radiofrequency fields for proton and carbon, respectively. Cross polarization occurs as a result of a recoupling process and the signal intensity is increased by a factor of γ_I/γ_S, which is about 4 for $^1H/^{13}C$.

2.3.2.3 CP/MAS

The cross polarization (CP) technique combined with magic-angle spinning (MAS) is called CP/MAS. For about two decades, the MAS technique was largely ignored until Stejeskal, Schaefer, and Waugh [13] in 1977 showed that more realistic rotational rates (3-5 kHz) capable of averaging chemical shift anisotropy combined with high-power decoupling to remove the ^1H dipolar broadening could be extremely effective in obtaining high resolution ^{13}C spectra from solids. Stejeskal, Schaefer and Waugh published the first CP/MAS spectra of ^{13}C in organic solids and polymers with proton decoupling, magic angle spinning, and cross polarization which is the CP/MAS technique that is now widely used. CP/MAS spectra and pulse sequence are shown in Figures 2.2 and 2.3, respectively.

2.3.2.4 Decoupling Dipolar Couplings

In 1972, a method of line narrowing was developed by Pines et al. [6] The broadening caused by the heteronuclear dipolar coupling with protons was averaged out by decoupling the protons and enhancing the low natural signal of ^{13}C by cross polarization (see below) with the protons. Because dipolar couplings are often 20 kHz or more and the rotation is not be fast enough to remove them completely, these dipolar interaction effects can often be eliminated by heteronuclear decoupling but very high decoupling powers are

needed for large couplings. For dipolar decoupling in solids, the power level may be as high as a kilowatt.

2.4 Coherences

The coherence order is the number of quanta energy between spin states. In addition to single quantum coherences involving only one spin, two spin transitions are also possible. As illustrated in Figure 2.4, there are four quantized energy levels for a coupled two spin-1/2 system. In NMR, single quantum coherences are detected directly where zero and double quantum coherences can be detected indirectly.

2.4.1 Single Quantum Coherence

When applying an rf field at the Larmor frequency where $\omega = \gamma B_0$, the spins resonate, there is a state of coherence with a net magnetization in the x-y plane. By applying a 90° pulse to an ensemble of spin-1/2 nuclei, the result will be a net magnetization from the z-axis to the transverse plane.

2.4.2 Double Quantum Coherence

By exciting pairs of strongly coupled spins, double quantum coherence can be generated. A double quantum coherence can be excited by a $\pi/2$-τ-$\pi/2$ pulse sequence. The first $\pi/2$ pulse generates a single quantum coherence that corresponds to transverse magnetization and under the dipolar coupling is evolved during τ in which terms in the density operator which describes the spin system are created where the second $\pi/2$ pulse converts them into double quantum terms, $I_xS_y + I_yS_x$. A quantized energy level diagram is shown in Figure 2.5 for a two coupled spin-1/2 nuclei. In Chapter 3, there is a discussion regarding the use of double quantum coherence in the DQ DRAWS experiment as a means to filter natural abundance background while measuring the rate of double quantum coherence between coupled spins.

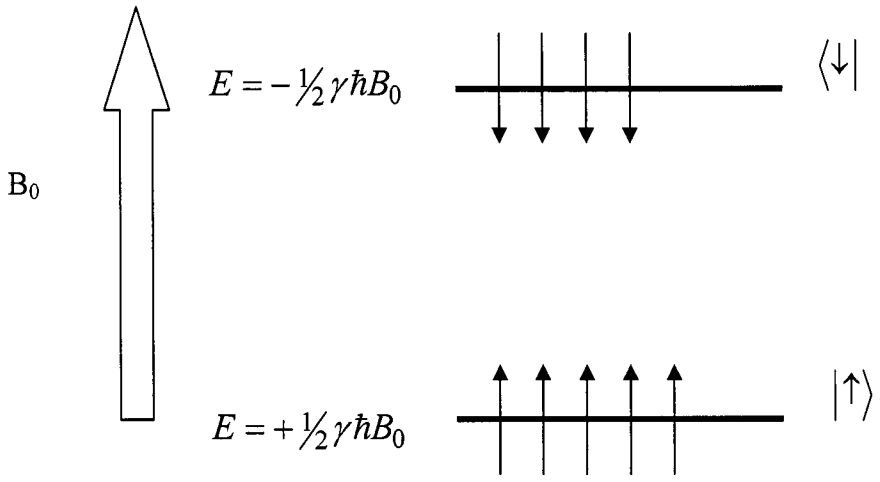

Figure 2.1 The energy level splitting due to the Zeeman interaction for a spin-1/2 nucleus. The energy levels are $E = \pm \frac{1}{2}\gamma\hbar B_0$. The low and high energy states are $|\uparrow\rangle$ and $\langle\downarrow|$, respectively.

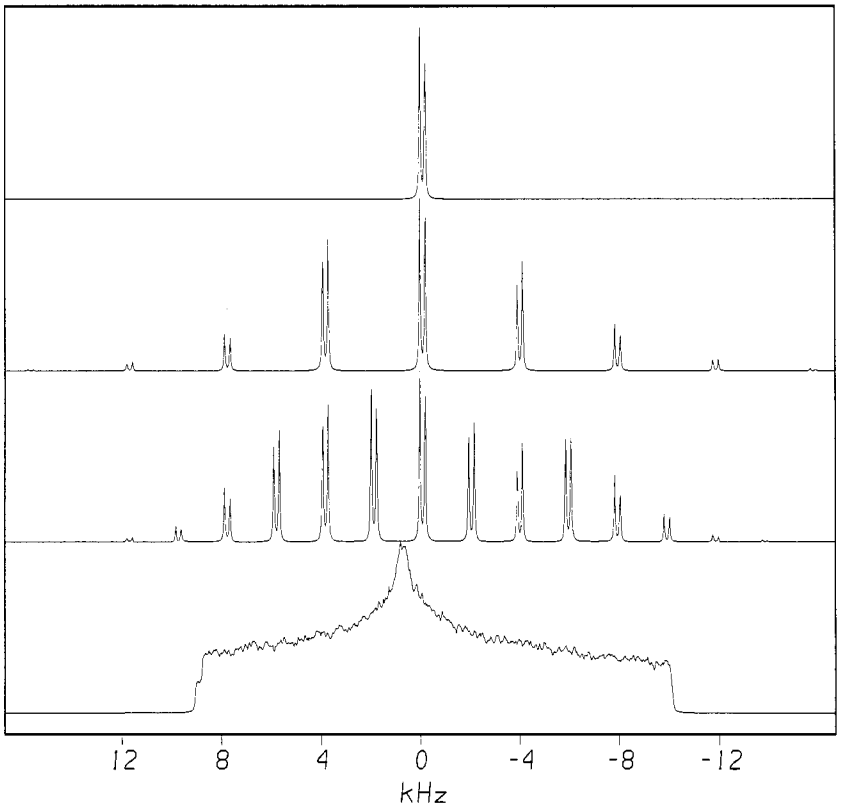

Figure 2.2 ^{13}C CPMAS simulation of spinning side bands at various rotation speeds of a peptide (*A*GG) with two backbone carbonyl carbons ^{13}C enriched. Bottom to top: spinning speeds of 0, 2, 4, and 22 kHz. (Adapted from N. A. Oyler University of Washington Thesis 2000)

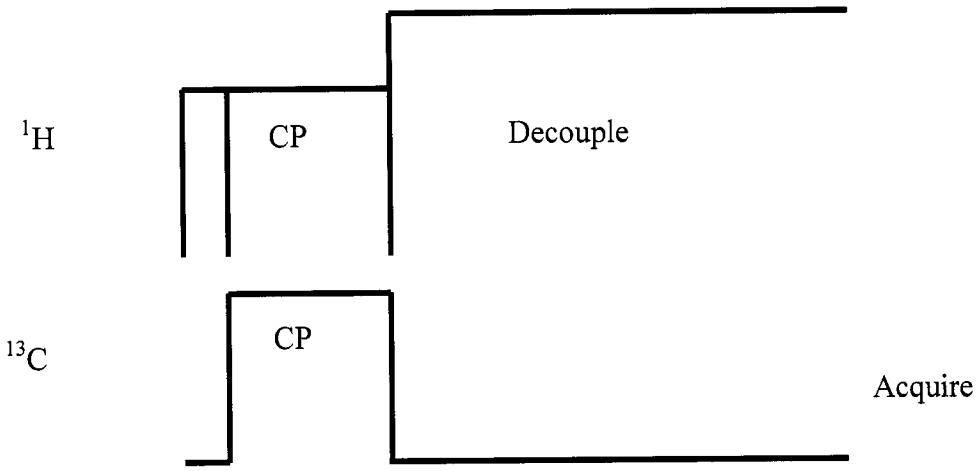

Figure 2.3 CP/MAS pulse sequence.

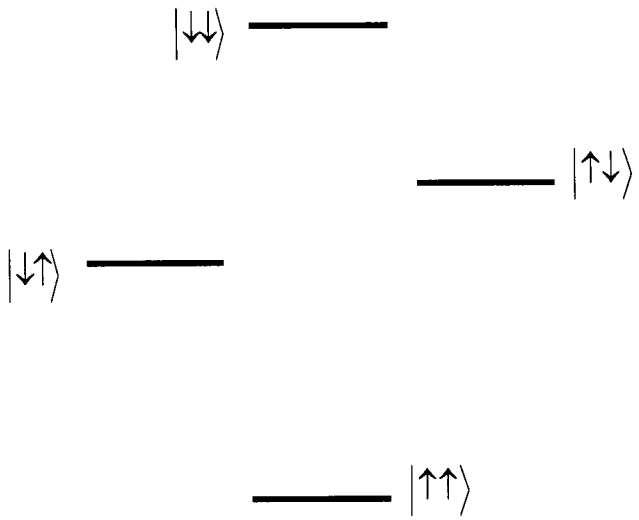

Figure 2.4 Four energy levels of a a two spin-1/2 system.

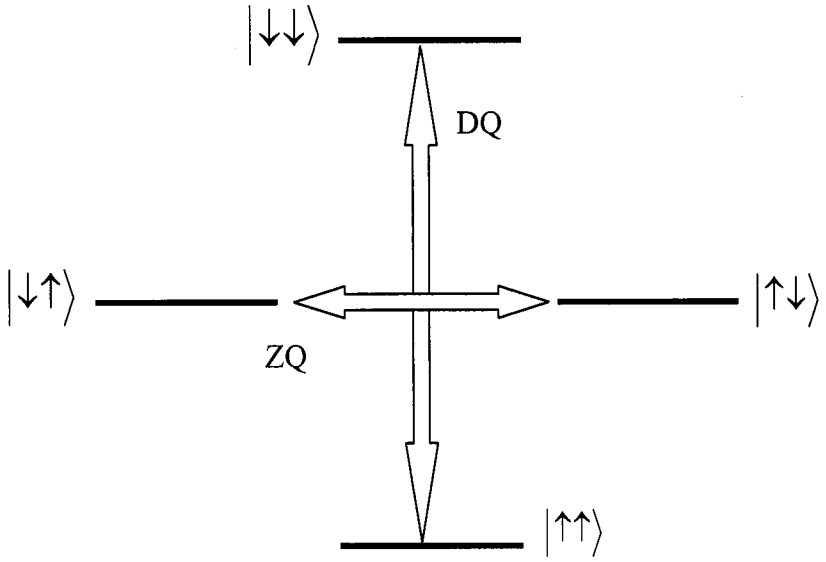

Figure 2.5 Quantized energy level diagram for a two spin-1/2 system where a double quantum coherence is a coherent superposition between the energy states $|\uparrow\uparrow\rangle$ and $|\downarrow\downarrow\rangle$ whereas a zero quantum coherence is a coherent superposition between $|\uparrow\downarrow\rangle$ and $|\downarrow\uparrow\rangle$.

Chapter 3: Dipolar Recoupling Methods

3.1 Introduction

There are several high resolution magic angle spinning (MAS) techniques that exist for the accurate determination of distances between pairs of spin 1/2 nuclei and they are listed in Table 3.1. By estimation of the dipole-dipole coupling constant, ν_D, between coupled spin pairs, internuclear distances between nuclei can be obtained by MAS NMR. The dipole-dipole coupling constant is inversely proportional to the cube of the internuclear distance, r as shown below,

$$\nu_D = \frac{h\gamma_I\gamma_S}{4\pi^2 r_{I-S}^3} \tag{3.1}$$

where γ is the gyromagentic ratio of the spin and h is Planck's constant.

The heteronuclear recoupling method used in this project is REDOR (Rotational Echo Double Resonance) due to its ease of implementation and straight forward analysis of the data [14]. The basis of the experiment is simple trains of rotor-synchronous π pulses. The data analysis is independent of relaxation effects, chemical shift anisotropy, and isotropic chemical shifts when using an XY8 phase cycling pulse sequence which compensates for these effects [14].

The homonouclear recoupling technique used is DRAWS (Dipolar Recoupling with a Windowless Sequence) for the advantage of being able to compensate for large CSAs [15].

3.2 Heteronuclear Dipolar Recoupling with REDOR

For a sample spinning at the magic angle, the dipolar coupling between an I-S heteronuclear spin pair is a function of time. Under MAS conditions, the dipolar coupling in hertz is

$$\nu_D(\alpha,\beta;t) = \frac{\nu_D}{2}[\sin^2\beta\cos 2(\alpha + 2\pi\nu_R t) - \sqrt{2}\sin 2\beta\cos(\alpha + 2\pi\nu_R t)] \quad (3.2)$$

where $\nu_D = \frac{h\gamma_I\gamma_S}{4\pi^2 r_{I-S}^3}$, ν_R is the rotor speed in Hertz, α is the azimuthal angle, and β is the polar angle defined by the internuclear vector, γ_I and γ_S are the gyromagnetic ratios for the I (observe spin) and S (dephase spin) spins, respectively, and r_{I-S} is the internuclear separation. The observed REDOR dephasing (S/S_0) is calculated by performing the standard powder average.

$$\frac{S}{S_0} = \frac{1}{4\pi}\int_{\alpha=0}^{2\pi}\int_{\beta=0}^{\pi}\cos[\frac{N_c\nu_D}{\nu_R}2\sqrt{2}\sin 2\beta\sin\alpha]d\alpha\sin\beta d\beta \quad (3.3)$$

where N_c is the number of rotor cycles.

REDOR [16,17] is a magic-angle spinning experiment for measuring internuclear distances between heteronuclear spin pairs. The REDOR experiment recovers heteronuclear dipolar interactions by using simple rotor-synchronized π pulses to recover the heteronuclear dipolar interaction. For a spin pair such as ^{31}P-^{19}F, REDOR involves the dephasing of transverse ^{31}P-spin magnetization by rotor synchronized ^{19}F-spin π pulses. By comparing ^{31}P-spin echo intensities with and without ^{19}F-spin dephasing pulses leads to the strength of the ^{31}P-^{19}F dipolar coupling, and thus, ^{31}P-^{19}F distances. The pulse sequence employed in the REDOR experiment is XY8-REDOR and it can be viewed in Figure. 3.1. The XY8 phase cycling scheme is used to minimize resonance

offset effects and compensate for pulse imperfections [18,19]. Following generation of ^{31}P magnetization by cross-polarization from the protons, the ^{31}P's are subjected to a series of 180° refocusing pulses. This full echo spectrum is designated S_0. In the second half of the experiment, in addition to the ^{31}P refocusing pulses, ^{19}F 180° pulses are added at the middle of the rotor period. These fluorine dephasing pulses reintroduce ^{31}P-^{19}F dipolar couplings averaged by magic angle spinning (MAS), and cause a dephasing of the observed ^{31}P signal. The second half of the spectrum is referred to as S, and the ratio of S/S_0 provides a dephasing curve that can be fit to theoretical equations which directly relates the dipolar coupling, $D_{P\text{-}F}$, between the ^{31}P and ^{19}F spins. Given the $D_{P\text{-}F}$, the internuclear distance, $r_{P\text{-}F}$, can be easily calculated from $r_{P\text{-}F} = [(\gamma_P\gamma_F h)/4\pi^2 D_{P\text{-}F})]^{1/3}$ where γ_P and γ_F are the gyromagnetic ratios of the P and F spins, respectively, h is Planck's constant, and D is in hertz.

3.2.1 Dephasing with multiple spins

Goetz and Schaefer [20] have presented closed form numerical algorithms for REDOR dephasing by multiple spins in the presence of molecular motion. The calculation assumes that the ^{19}F -^{19}F homonuclear interaction does not affect REDOR dephasing. For a trifluoromethyl group, fast rotation about the C_3 axis ensures that the three fluorine nuclei have identical, motionally averaged chemical shifts. For a rapidly rotating trifluoromethyl group, there are three spins moving relative to the ^{31}P observe nucleus. As long as the trifluoromethyl group rotates faster than the ^{19}F-^{19}F dipolar coupling strength, the strong ^{19}F-^{19}F homonuclear interaction does not need to be included when calculating REDOR dephasing by ^{19}F in a rotating -CF_3 group [20-22]. A non rotating -CF_3 group would immobilize the fluorine nucleus in the sample and thus the phosphorous couples to each fluorine instead of the fluorines as a unit.

A static $-CF_3$ group would suppress the dephasing curve and incomplete dephasing would occur due to the homonuclear recoupling of the fluorine spins.

In this case, each fluorine contributes one cosine term and the dephasing can be described as

$$\begin{aligned}\frac{S}{S_0} = \frac{1}{8\pi^2}\int_{\psi}^{2\pi}\int_{\theta}^{\pi}\int_{\phi}^{2\pi} & \cos\left[\frac{4\sqrt{2}N_c}{N\nu_R}\sum_{i=1}^{N}\nu_D^i[\hat{n}'(i)\cdot\hat{y}][\hat{n}'(i)\cdot\hat{z}]\right] \\ & \times\cos\left[\frac{4\sqrt{2}N_c}{N\nu_R}\sum_{i=1}^{N}\nu_D^i[\hat{n}'(i)\cdot\hat{y}][\hat{n}'(i)\cdot\hat{z}]\right] \\ & \times\cos\left[\frac{4\sqrt{2}N_c}{N\nu_R}\sum_{i=1}^{N}\nu_D^i[\hat{n}'(i)\cdot\hat{y}][\hat{n}'(i)\cdot\hat{z}]\right] \\ & \times d\phi\sin\theta\, d\theta\, d\psi\end{aligned} \tag{3.4}$$

where N_c is the number of rotor cycles, N is the number of steps that the S spin moves through its trajectory, and the unit vector from the I spin to the S(i) spin is $\hat{n}(i) = \mathbf{r}_{IS}^i / \left|\mathbf{r}_{IS}^i\right| = (\hat{x}(i), \hat{y}(i), \hat{z}(i))$. Rotation of this unit vector by (ϕ, θ, ψ) gives a new vector, $\hat{n}'(i)$, defined by

$$\hat{n}'(i) = \mathbf{A}(\phi,\theta,\psi)\cdot\hat{n}(i), \tag{3.5}$$

where $A(\phi, \theta, \psi)$ is the 3×3 Eulerian rotation matrix. After the rotation, projections of the rotated unit vector are expressed in terms of α and β as

$$\begin{aligned}\hat{n}'(i)\cdot\hat{x} &= \sin\beta^{(i)}\cos\alpha^{(i)} \\ \hat{n}'(i)\cdot\hat{y} &= \sin\beta^{(i)}\sin\alpha^{(i)} \\ \hat{n}'(i)\cdot\hat{z} &= \cos\beta^{(i)}\end{aligned} \tag{3.6}$$

By assuming an Euler rotation in the Rose convention,

$$\hat{n}'(i)\cdot\hat{z} = [\sin\theta\cos\phi]\hat{x}(i) + [\sin\theta\sin\phi]\hat{y}(i) + [\cos\theta]\hat{z}(i) \tag{3.7}$$

and

$$\begin{aligned}\hat{n}'(i)\cdot\hat{y} = &[-\cos\psi\sin\phi - \cos\theta\cos\phi\sin\psi]\hat{x}(i)\\ &+[\cos\psi\cos\phi - \cos\theta c\sin\phi\sin\psi]\hat{y}(i)\\ &+[\sin\psi\sin\theta]\hat{z}(i).\end{aligned} \tag{3.8}$$

Now the argument of the cosine term of equation 3.3 can be evaluated using

$$\begin{aligned}\sin 2\beta^{(i)}\sin\alpha^{(i)} &= 2\cos\beta^{(i)}\sin\beta^{(i)}\sin\alpha^{(i)}\\ &= 2[\hat{n}'(i)\cdot\hat{y}][\hat{n}'(i)\cdot\hat{z}].\end{aligned} \tag{3.9}$$

The multiple-spin REDOR expression in Equation 3.4 has a product of three cosines, one for each fluorine. The cosine arguments are sums of terms which depend on the positions of the fluorines as a function of time [20]. The number of steps of the trajectory, N, was determined by increasing the number of steps until the calculated REDOR dephasing converged. Fast rotation about the C_3 axis for a trifluoromethyl group ensures that the three fluorine nuclei have identical motionally averaged chemical shifts. The time-averaged commutator $\langle[S^i,S^j]\rangle$ is strictly zero as long as the trifluoromethyl group rotates faster than the F-F dipolar coupling strength [20]. Thus, the strong F-F homonuclear interaction does not need to be included when calculating REDOR dephasing by ^{19}F in a -CF_3 group [20].

3.3 Homonuclear Dipolar Recoupling with DRAWS

The Dipolar Recoupling with a Windowless Sequence (DRAWS) experiment is a homonuclear dipolar recoupling experiment developed in the Drobny Lab [23]. The need for experiments by solid-state NMR are being explored for their use in determining structure of heterogeneous biological systems. Initially the first experiments with the DRAWS sequence were used on model compounds and DNA. Within the last several years, the DRAWS experiment has been implemented in its use to determine dipolar couplings in peptides where the peptides are adsorbed or covalently bound to surfaces, and

peptides in membranes [24-30]. The DRAWS pulse sequence is shown in Figure 3.2A. In the sequence, there are two 90 degree pulses in each rotor period which effectively defeats the averaging of the dipolar coupling. The sequence can be viewed as having five components comprised of three x-phase continuous rf pulses and two periods of y-phase pulses. The 90 degree pulses divulge a time dependence to the spin Hamiltonian and therefore recouples the dipolar Hamiltonian. A single DRAWS cycle is unable to completely suppress the chemical shift however, by applying a supercycle of the DRAWS sequence as shown in the bottom of Figure 3.2, the chemical shift Hamiltonian is suppressed to zero [31].

In the DRAWS experiment, by rotating the initial $I_y + S_y$ state with the I_xS_x, the antiphase state, $I_xS_z + I_zS_x$, is created which is non-observable at the end of each rotor period. In addition, within each rotor period, the 360° pulses rotate the magnetization on a shorter time scale [23].

3.3.1 Filtering with Double Quantum DRAWS

The double quantum DRAWS (DQDRAWS) experiment is a variant of the DRAWS experiment and becomes quite useful when natural abundance signal are significant and perhaps overlap with the peak of interest.

DQDRAWS, a homonuclear recoupling technique can be used to measure the distance between adjacent carbonyl carbons in the peptide backbone for determination of the backbone torsion angle φ. The rate at which double quantum coherence is generated is measured as a function of the DRAWS mixing time which allows the determination of the distance between two spins. This experiment has lower sensitivity compared to the DRAWS experiment, however, the advantage of the DQDRAWS experiment is that it filters out the contributions from the natural abundance background.

In the 2D DQDRAWS experiment, CSA-CSA correlations are achieved in a coherent manner as opposed to a spin diffusion fashion [32]. The t1 evolution is sensitive to the relative orientation between CSA tensors. Thus, for a two spin system, the Fourier transform of the t1 dimension (called a DQ projection) shows spinning sidebands with the isotropic located at the tensor sum of the two CSA isotropics and the relative intensities of the sidebands reflect the sum of the chemical shift and the dipolar interaction.

Table 3.1 Homonuclear and heteronuclear recoupling methods.

Homonuclear Recoupling Techniques	**Heteronuclear Recoupling Techniques**
Rotational Resonance (R2)	Dipolar Exchange-Assisted Recoupling (DEAR)
Synchronized Radiofrequency Pulse Cycles Combined in a Sevenfold-Symmetric Phase Shift Scheme (C7)	Rotational-Echo Double Resonance (REDOR)
Dipolar Correlation Spectroscopy (DICSY)	Transfer-Echo Double Resonance (TEDOR)
Dipolar Recovery at the Magic Angle (DRAMA)	Rotational-Echo, Adiabatic Passage Double Resonance (REAPDOR)
Dipolar Recovery with a Windowless Sequence (DRAWS)	Transfer of Populations in Double Resonance (TRAPDOR)
Radiofrequency Driven Dipolar Recoupling (RFDR)	
Simple Excitation for the Dephasing of Rotational-Echo Amplitudes (SEDRA)	
Melding o the Spin-Locking and DRAMA (MELODRAMA)	

A) S_0 experiment

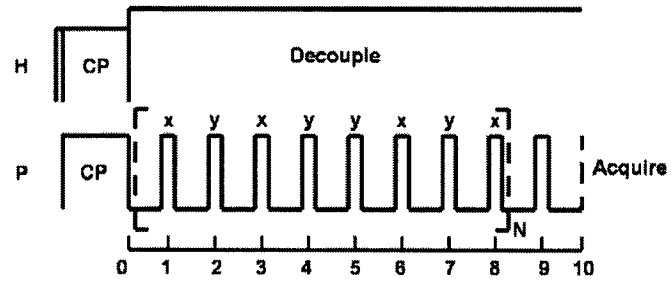

B) S experiment

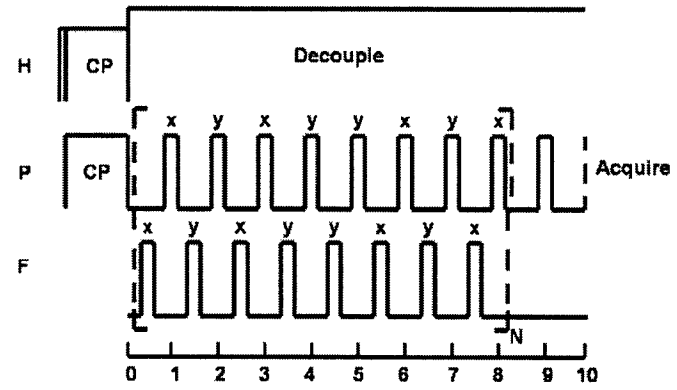

Figure 3.1 The XY8–REDOR pulse sequence for measuring ^{31}P-^{19}F dipolar couplings. A) The S_0 (full echo) experiment shows that following cross polarization (CP) from ^{1}H to ^{31}P, the phosphorus signal is refocused by a series of π pulses following the XY8 phase cycling. B) On alternate scans, the S (reduced echo) experiment is collected. The ^{19}F π pulses are used to recouple the fluorine to the phosphorous nuclei. N is the number of XY8 cycles.

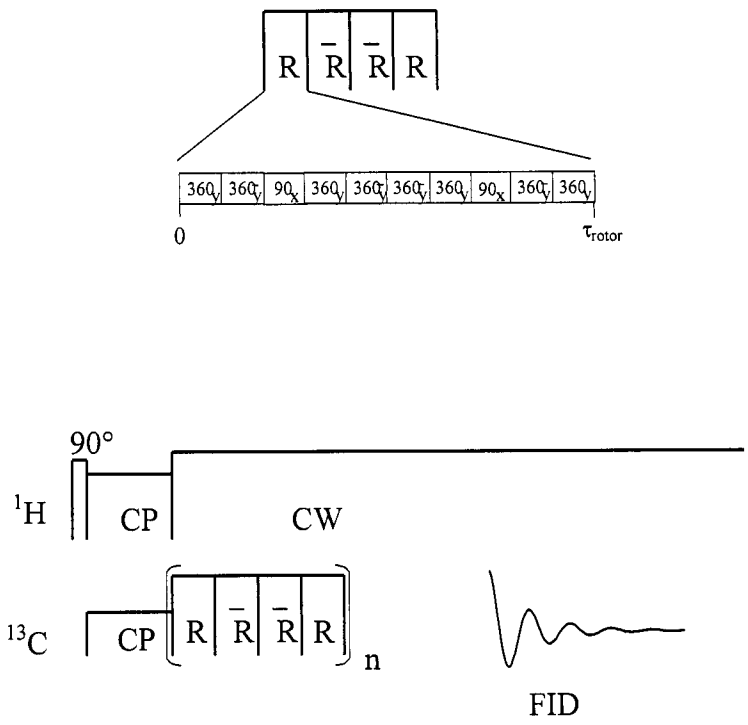

Figure 3.2 A) Top: Magnified view of a DRAWS cycle where R represents one DRAWS cycle which is contained in a single rotor period. A supercyle is composed of four DRAWS cycles, $R-\bar{R}-\bar{R}-R$. Bottom: Pulse sequence of DRAWS where n is the number of DRAWS supercycles.

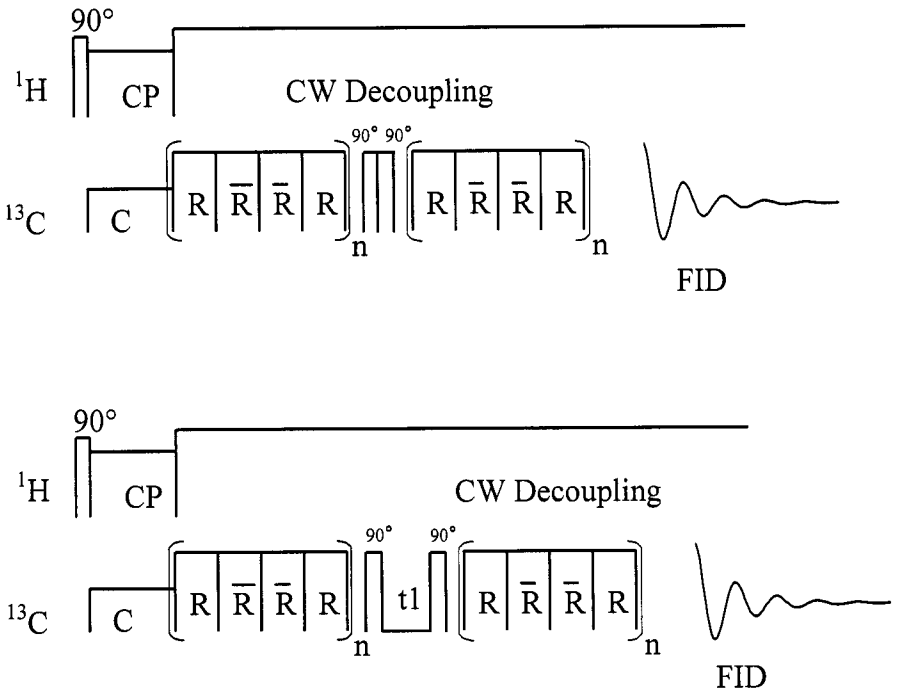

Figure 3.2 B) Pulse sequence of DQ DRAWS (top) and 2D DQ DRAWS (bottom). The 2D DQ DRAWS sequence has a t1 delay between the two $\pi/2$ pulses.

Chapter 4: Materials, Synthesis and Methods

4.1. Small Model Compounds

The synthesis of the small model compounds (**1-4** in Figure 4.1) were performed by Dr. Panadda Chirakul in the Sigurdsson laboratory. In general, the procedure for the synthesis of the small model compounds (**1-4**) is outlined in Figure 4.1 [33]. Briefly, a fluorinated/trifluoromethylated phenol group was reacted with 2-cyanoethyl diisopropylchlorophosphoramidite. The resulting phosphoramidite was reacted with 2-hydroxypropionitrile in acetonitrile at room temperature with ethylthiotetrazole and then oxidized with an iodine solution to yield a phosphodiester. The single fluorinated phosphodiester product was deprotected by concentrated aqueous ammonia at room temperature for 16 hours to generate the desired phosphate where as the trifluoromethylphosphates were deprotected with potassium carbonate in methanol. To get the product in a disodium phosphate form, the phosphate product was treated by cation exchange chromatography.

CF_3 umbellifereone disodium phosphate, 5-F dU CE phosphoramidite, and 2'F dT CE phosphoramidite were purchased from Sigma.

4.2. General outline of solid phase DNA synthesis

The chemistry of the DNA synthesis is composed of several synthetic steps: condensation, capping, oxidation, and cleavage/deprotection. The first nucleoside on a solid support is deprotected (detritylated), where the dimethoxytrityl group, is removed with trichloroacetic acid in methylene chloride. The role of tetrazole is to catalyze the coupling reaction of the deprotected monomer on the support with a cyanoethyl phosphoramidite monomer in solution to yield a fully protected dimer on the support. Unreacted

support bound monomers will be present and need to be capped or acetylated by acetic anhydride/lutidine so that they can no longer react and condense with phosphoramidite monomers in solution. The capping step is extremely important. In each cycle approximately 1.5 % of the nucleotide chains on the glass beads fail to react with the activated monomer, and if this is not addressed, a complex mixture of truncated sequences would accumulate where the majority would be one nucleotide shorter than the correct product. After the capping step, the dimer is oxidized with aqueous iodine (I_2/THF/pyridine/water) to convert the phosphite triester into a phosphate triester. Then the entire cycle of detritylate, condense, cap, oxidize continue for as long as the desired oligomer is to be. The final step is to deprotect the base and phosphate groups, and cleave the oligomer from the resin which occurs in concentrated aqueous ammonia for 55° C for 8 hours.

4.2.1 Synthesis of protected 5-CF_3 dU CE phosphoramidite

The reaction of 4,4'-dimethoxytrityl chloride (DMT-Cl) with 2'-Deoxy-5-(trifluoro-methyl)uridine is highly selective for the primary, 5'-hydroxyl group over the secondary, 3'-hydroxyl group. By using a slight excess of DMT-Cl, the reaction is usually complete with 1 hour using 4-dimethyl aminopyridine (DMAP) as a catalyst. The product is purified using silica gel chromatography.

Under vacuum, the following reagents: 2'-Deoxy-5-(trifluoromethyl)uridine (0.94mmol (0.279g), DMT-Cl (0.4550g), and DMAP (6 mg) were placed in a dry round bottom flask and dried overnight. Next, under argon, anhydrous pyridine (10 mL) and trimethylamine (TEA) (0.4 mL) were added and the reaction mixture stirred. The reaction was followed by thin layer chromatography (TLC) and more DMT-Cl and TEA was added if the reaction

was not complete by 2 hours. The solvent mixture for the TLC developing chamber was methylene chloride:methanol (50:1).

When the reaction was completed, an equal volume (12 mL) of water was added and the product was extracted with 50 mL of ether three times. The ether layers were combined and concentrated by rotary evaporation.

The product was purified by using silica gel column chromatography. The column was packed in methylene chloride and eluted first with CH_2Cl_2 and then CH_2Cl_2:CH_3OH (50:1).

^{1}H NMR ($CDCl_3$) δ (ppm) 1.9 (m, 1, H-2'), 2.16 (m, 1, H-2"), 2.88 (m, 1, H-5'), 3.29 (m, 1, H-5"), 3.8 (m, 7, H-4',O-CH_3), 4.3 (m, 1, H-3'), 6.3 (m, 1, H-1'), 6.8, 7.3, 7.4 (m, 13, H-phenyl), 8.2 (s, 1, H-6).

4.2.2 Phosphoramidite synthesis:

Tritylated CF_3 uridine (0.5mmol) was dried over night under vacuum. Under argon, diisopropylethylamine (4 eq., 0.35 mL) and anhydrous CH_2Cl_2 (1 mL) was added. The reaction was stirred until dissolved followed by injection of 2-cyanoethyl diisopropylchlorophosphoramidite (1.5 eq, 0.167 mL) over 20 seconds. The reaction mixture was checked by TLC using 45:45:10 ethylacetate:methylene chloride: triethylamine. If the reaction had not gone to completion more phosphitylating reagent was added.

The excess phosphitylating agent was quenched with anhydrous methanol.

The crude product was transferred to a separatory funnel and diluted with 11 mL ethyl acetate and 0.5 mL TEA. The product was washed twice with 10 mL of 10% aqueous sodium carbonate (Na_2CO_3), then the organic phase was

dried over anhydrous sodium sulfate (Na_2SO_4), filtered, and solvent was evaporated.

The product was purified using silica gel column chromatography. The solvent mixture used to pack the column and as an eluant was 45:45:10 ethylacetate:methylene chloride: triethylamine. The product was collected and dried in a amber bottle.

Before use on the DNA synthesizer, the pure product was filtered using a 0.5um filter with anhydrous acetonitrile and dried.

^{1}H NMR (CD_2Cl_2) δ (ppm) 1.2 (m, 12, CH_3), 1.4 (m, 4, CH_2), 2.3 (m, 4, N-CH_2), 2.4 (m, 1, H-2'), 2.6 (m, 1, H-2"), 3.4 (m, 1, H-5'), 3.45 (m, 1, H-5"), 3.82 (s, 6, O-CH_3), 4.2 (m, 1, H-4'), 4.48 (m, 1, H-3'), 6. (m, 1, H-1'), 6.85, 7.3, 7.4 (m,13, H-phenyl), 8.2 (s, 1, H-6).

^{31}P NMR (CD_2Cl_2) δ (ppm) 148.2(s) and 147.7 (s).

4.2.3 Synthetic DNA details

Synthesis of 5'-d(CGCATT-(pS)-TT$^{5\text{-}F}$UGCG)-3', 5'-(dCGCAAAAATGCG)-3', and 5'd(CGCAAAAATG(pS)CG)-3'

All DNA were synthesized on an Applied Biosystems Model 394 synthesizer using either acetyl (Ac) or ultramild protecting groups (Glen Research) and CPG resin.

DNA incorporated with 5-fluorodeoxyuridine (5-FdU) (Glen Research) and phosphorothioate (pS) utilized the acetyl (Ac) protected dT, dG, dA, and 5-F dU CE phosphoramidites (Glen Research). Incorporation of a phosphorothiate into a DNA is done at the oxidation step where a sulfurizing agent (Glen Research) is used in place of an iodine solution. Unlabeled DNA were synthesized using acetyl protected phosphoramidites. Single fluorine,

phosphorothioate, and unlabeled DNA were deprotected and cleaved from resin by using concentrated aqueous ammonia at 55 °C for 16 hours.

Synthesis 5'd(CGCATT-(pS)-TT$^{5\text{-}CF3}$UGCG)-3' and 5'd(CGCATTTT $^{5\text{-}CF3}$UTGCG)-3'

Initial synthesis of incorporating a -CF_3 group into a DNA utilizing the above protected acetyl phosphoramidites resulted in the conversion of the -CF_3 to a -CN group (Figure 4.2) due to the presence of a strong base (conc. aq. ammonia) during the deprotection step [34]. Thus, the following synthesis procedure was used which allows for a more mild deprotection step.

The trifluoromethyl was incorporated into the DNA by using the 2'-deoxy-5-(trifluoromethyl)uridine protected cyanoethyl phosphoramidite The protected cyanoethyl phosphoramidites used were phenoxyacetyl (Pac) protected dA, 4-isopropyl-phenoxyacetyl (iPr-Pac) protected dG, acetyl (Ac) protected dC, and protected dT which were purchased from Glen Research. The phosphorothioate was incorporated by using a sulfurizing agent in place of the oxidizing solution (I_2 in pyridine/THF/H_2O). By utilizing the protected Pac, iPr-Pac, and Ac phosphoramidites allowed for ultramild deprotection. Cleavage from the resin and deprotection was carried out in 2 hours at room temperature with 0.05 M potassium carbonate in methanol. The single-stranded oligonucleotide with the 5' dimethoxytrityl group still attached was purified by reverse-phase high performance liquid chromatography (HPLC). The dimethoxytrityl group was then removed by using 80% acetic acid, and the DNA was repurified by HPLC (gradient and solvent: 10 umol DNA was brought up to 8 ml by 100 mM Et_3NHOAc prep-HPLC: buffer A: 100 mM Et_3NHOAc, buffer B: Acetonitrile, 10 ml/min, λ 260, 2 ml loop: 0-13 min @ 2%B, 13-25

min @ 2-15%B, 25-35 min @ 15-35 %B, 35-48 min @35%B, 48-53 min @ 35-2 %B, 53-62 min @ 2%B.)

Synthesis of DNAs with a 5-FdU (fluorodeoxyuridine) or 2'-FdT (fluorodeoxythymidine) were synthesized on an Applied Biosystems Model 394 synthesizer utilizing the 5-F dU CE phosphoramidite or 2'F dT CE phosphoramidite and incorporated them in to the following sequences. The incorporation of a phosphorothiate into a DNA is done at the oxidation step where a sulfurizing agent is used instead of the iodine solution.

The DNA sequence [5'-d(CGCATTTTTGCG)], with a trifluoromethyl and a phosphorothioate, was synthesized with an Applied Biosystems Model

4.3 Experimental Methods for small model compounds and DNA

In the following section, the preparation of the biological samples used in the studies of chapter 5 are described. In addition, the NMR spectroscopy parameters for the studies are presented.

4.3.1 Sample preparation of model compounds.

To dilute the spins, 5 – 10 mg of 1-4 were dissolved in deionized water and diluted with solutions of KBr and/or benzoic acid, lyophilized, and packed in a 5 mm rotor. 60 μL H2O was added to 5 mg (3) and the liquid sample was then placed in a 5 mm rotor with tight end caps.

4.3.2 Sample preparation of DNA

In general, the DNAs were salted with 10% (w/w) NaCl and 10% (w/w) Na_2EDTA, annealed at 85 °C for ten minutes, lyophilized, and packed in 5 mm ceramic rotors, and placed in an 85% hydration chamber to yield at least 11 waters per nucleotide by weight which ensures that the DNA is in B form [35].

4.3.3 NMR spectroscopy.

All CPMAS and REDOR experiments were performed on a 4.7 T (200 MHz proton Larmor frequency) magnet, homebuilt MAS triple resonance (^{1}H, ^{19}F, ^{31}P) probe [36,37] and homebuilt console [38]. The ^{1}H $\pi/2$ pulse was set at 5 μs and the ^{31}P and ^{19}F π pulses were 10 μs and 7 μs, respectively. The ^{1}H and ^{31}P cross polarization (CP) time was 2 ms and at 50 kHz field. ^{1}H decoupling was set at 100-120 kHz during evolution and 80 kHz during acquisition. Hydrated DNA or samples diluted in water were run at low temperature which ranged from –16° to –27° C with a spinning speed of 5988 Hz. The model compounds **1-4** were run at a spinning speed of either 4505 Hz or 5988 Hz. The pulse sequence employed was XY8-REDOR [17] as shown in Figure 3.1 and is a version of REDOR with multiple pulses on the observe and dephase channels with XY-8 phase cycling.

4.4 General outline of solid-phase peptide synthesis

The labeled peptides (using FMOC protected amino acids) can be prepared by using solid phase peptide synthesis on an automated Applied Biosystems 433A peptide synthesizer. Peptides are cleaved from the resin and purified using HPLC (C-18 reverse phase column). Peptide fractions are lyophilized and analyzed using matrix assisted laser desorption (MALDI)/ionization mass spectrometry.

4.4.1 Isotopically labeled FMOC amino acids

The labeled amino acids were prepared using FMOC chemistry for the synthesis of the labeled peptides of gramicidin A and LK*a*-14. Carbonyl ^{13}C-labeled amino acids (leucine, glycine, and alanine) were purchased from Cambridge Isotope Laboratories and FMOC-protected using standard protocols.

4.4.2 Synthesis of peptides

Two adjacent carbonyl carbons were ^{13}C labeled as noted in bold in the following peptide sequences of gramicidin A, HCO- L-Val-**$^{13}C_1$-Gly-$^{13}C_1$-L-Ala**-D-Leu-L-Ala-D-Val–L-Val-D-Val-L-Trp-D-Leu-L-Trp-D-Leu-L-Trp-D-Leu-L-Trp-$NHCH_2CH_2OH$, and LKa-14, Ac-LKKLLK-**$^{13}C_1$-L-$^{13}C_1$-L-**KKLLKL-NH_2.

The peptide, gramicidin A, was synthesized by solid-phase peptide synthesis using a 433 ABI peptide synthesizer. FMOC protected amino acids were used the carbonyl ^{13}C labeled amino acids were prepared according to standard FMOC protocol. Resin for the gA synthesis was purchased from BaChem. After cleavage from the solid support, the peptide was modified with an ethanolamine and formyl termini. The purity was assessed by HPLC and characterized by electrospray mass spectrometry as described by Fields et al. [39,40]

The LKα-14 peptide was synthesized on a 433 ABI peptide synthesizer. FMOC amino acids,^{13}C labeled FMOC L-leucines, and an MBHA resin were used. The peptides were cleaved from the resin using 95% trifluoroacetic acid with 2.5% triisopropysilane and 2.5% water. The crude peptide was purified using a Waters HPLC C-18 reversed-phase column with a water/acetonitrile solvent system containing 0.1% trifluoroacetic acid. To determine isotope incorporation and purity, the peptide fractions were lyophilized and analyzed by electrospray mass spectrometry. Figure 4.3 shows a ^1H solution spectrum of gA in $CDCl_3$.

4.5 Experimental Methods for Peptides

DMPC lipids purchased from Avanti Polar Lipids. Microsphere functionalized polystyrene purchased from Polysciences, Inc.

4.5.1 Adsorption Studies by Fluorimetry

An unlabeled LKα-14 peptide stock solution of 2.3μmol/10mL was made by dissolving LKα-14 peptide in distilled water. The resulting pH was 7.2. There was further dilution for adsorptions studies which yielded 11 samples with concentrations in the range of $5.75e^{-6}$ μmol – $1.15e^{-4}$ μmol peptide. 200μL of each diluted peptide solution were added to 80 μL of plain polystyrene and functionalized polystyrene beads of 0.2 μm. The peptide and functionalized polystyrene bead solutions were allowed to equilibrate in a shaker at 38 °C for 24 hours. Beads were centrifuged at 11,000 rpm and 200 μL. Aliquots of 250 μL unbound solution top layer were taken and stored in a 2 mL eppendorf tube to determine amount of peptide adsorbed by measuring the unbound peptide concentration.

A Hitatchi fluorescence spectrophotometer F4500 was used for the fluorimetry experiments where the excitation wavelength was at 360 nm and the emission wavelength measured at 445 nm. The scan speed was 240 nm per mininute. Just before taking fluorimetry measurements, 100 μL unbound peptide solution was pipetted into a 10 mm pathlength cuvette cell and 1000 mL fluoraldehyde was added. Figure 4.4 illustrates the peptide derivatization with fluoraldehyde for the fluorimetry experiments. Fluorescence measurements were taken 60 seconds after fluoraldehyde was added to peptide solution. When measurements were taken on different days, a new peptide concentration vs. intensity calibration curve was made for the very dilute peptide solutions.

4.5.2 Sample Preparation for Dynamic Light Scattering

LKα-14 peptide with and without carboxylated polystyrene beads (0.2 μm) samples were diluted. Samples were prepared with PBS buffer pH 7.4 and without. Carboxylated polystyrene beads were also checked and compared to

manufactureer's specifications. Particle sizing was performed on a Brookhaven Instruments Corporation (BIC) PALS.

4.5.3 NMR Studies

Sample Preparation: Hydrated samples of gA in lipid bilayers were prepared by codissolving gA with DMPC (1:8 mole ratio of peptide:lipid) in methanol with 3 freeze thaw cycles. The solution was frozen in liquid nitrogen and lyophilized. The lyophilized sample was hydrated with nanopure water to reach a hydration of 30% water by weight in 45 degree oven for 4-5 days until peptide/lipid sample was transparent white, then sealed with epoxy in rotor glass tube insert.

For unhydrated samples, NMR experiments were performed at room temperature, 23 degrees C. For hydrated samples, NMR experiments were performed at low temperature of -40 degrees C due to better cross polarization match, thus enhancing signal intensity. DQ DRAWS experiment equipment and parameters. spinning speed 4000 Hz, 9.7 T superconducting magnet, homebuilt console, Chemagnetics HX probe.

All CPMAS, DRAWS, DQ DRAWS, 2D DQ DRAWS experiments were performed on a 9.4 T (400.26 MHz proton Larmor frequency) magnet, Chemagnetics MAS double resonance HX probe [36,37] and homebuilt console [38]. The ^{1}H $\pi/2$ pulse was set at 5-6 μs and the ^{13}C $\pi/2$, π, and 2π pulses were calibrated for the DRAWS experiments to be 7.35μs, 15.05 μs, and 29.4 μs respectively for a 4000 Hz spinning speed. The ^{1}H and ^{13}C cross polarization (CP) time was 2 ms. ^{1}H decoupling was set at 120 kHz during evolution and acquisition. Hydrated DNA or samples diluted in water were run at low temperature which ranged from –16° to –27° C with a spinning speed of 4000

Hz. For the 2D DQ DRAWS experiments, the t1 was set at 25 μs and n was determined from the DQ DRAWS buildup curve to be 3-4.

4.5.4 NMR Simulations

DQDRAWS buildup and 2D DQDRAWS data were simulated using C++ code operating in a Matlab environment written by Nathan Oyler [32]. Simulations incorporated the observed CSAs, experimental parameters, principal axes of the CSA relative to the amide bonds (molecular frames), and relaxation parameters. CSAs were determined by modeling the observed isotropic and side band intensities using Herzfeld Berger Analysis [41]

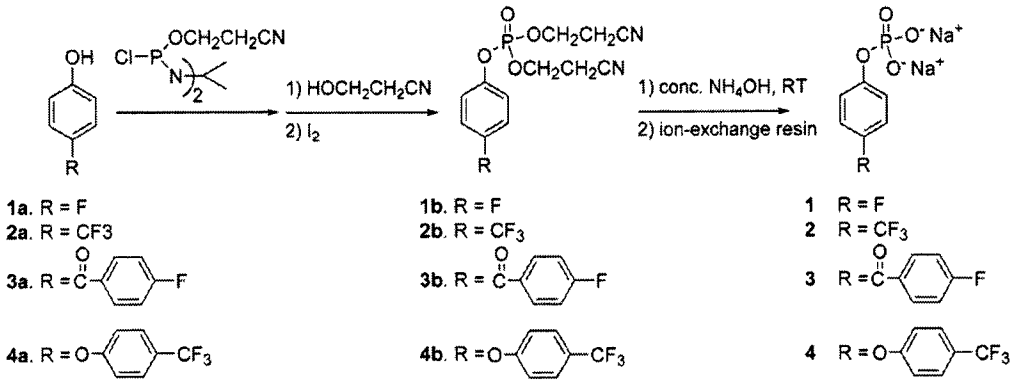

Figure 4.1 Synthesis scheme for small model compounds (**1-4**). The CF_3 molecules were deprotected with potassium carbonate in methanol while the singly fluorinated molecules were deprotected in concentrated aqueous ammonia.

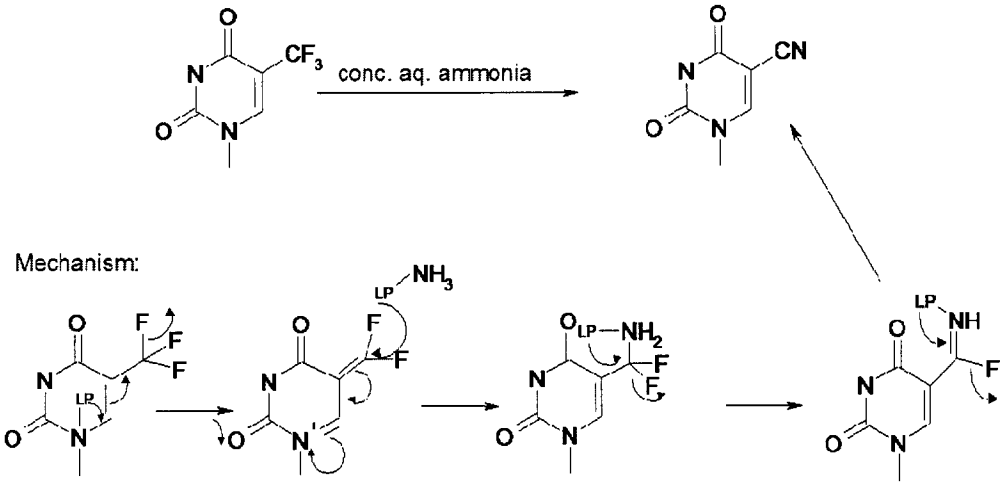

Figure 4.2 Conversion of trifluoromethyl (-CF_3) to nitrile (CN) group under basic conditions.

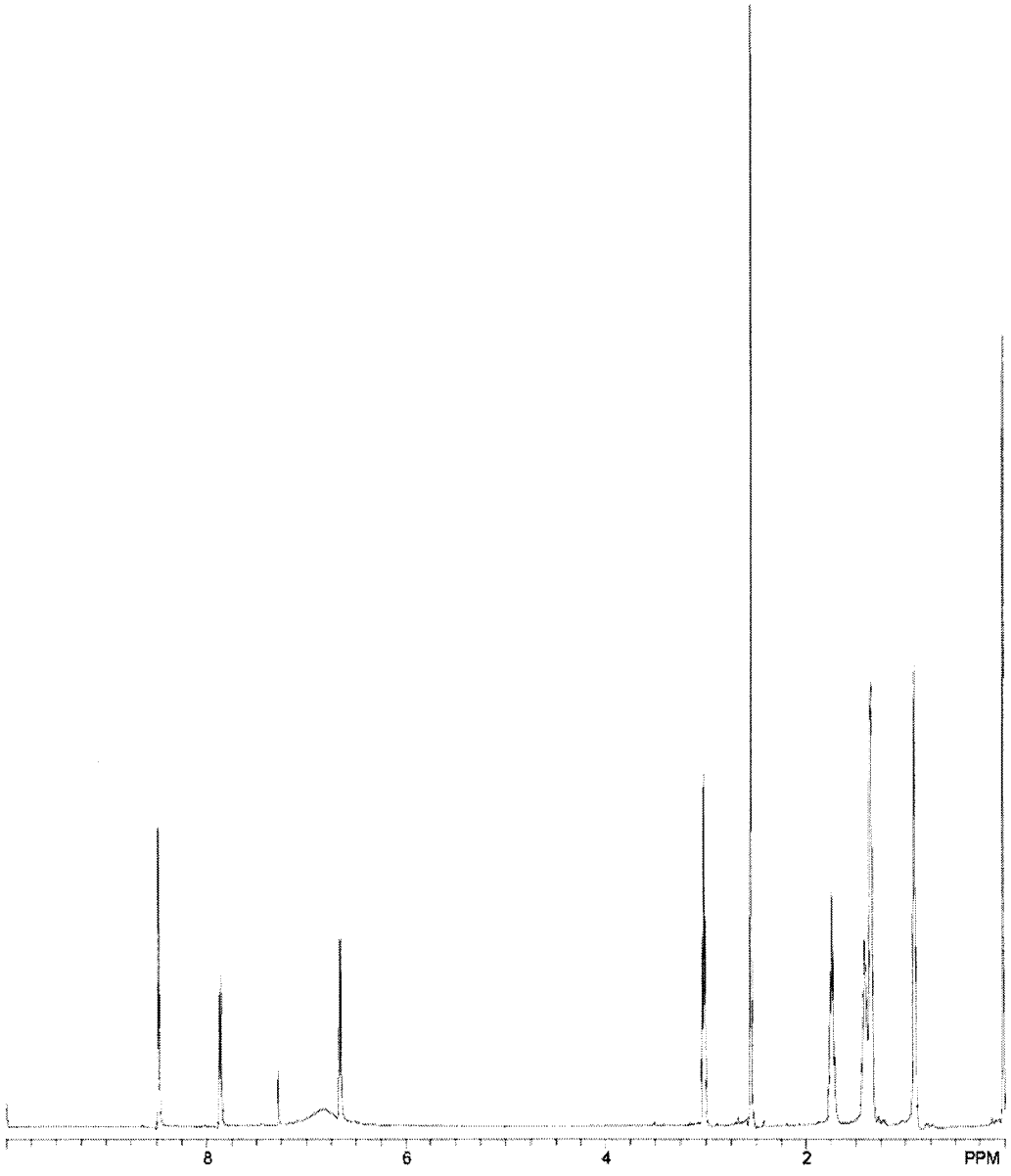

Figure 4.3 ^{1}H NMR of gA in $CDCl_3$ with TMS

Fluorimetric Analysis for Adsorption Studies:

Derivatization with *o*-phthaladehyde

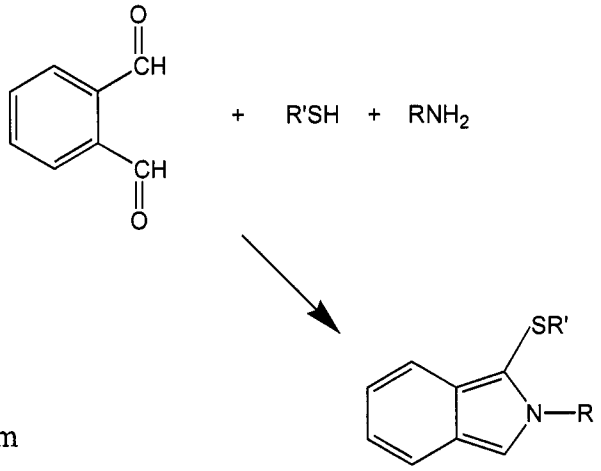

excitation: 360 nm

emission: 445 nm

Figure 4.4 Schematic of peptide derivatization for fluorimetry experiments.

Chapter 5: Using $^{31}P\{^{19}F_3\}$ REDOR NMR to Determine Long-Distance Measurements of Model Compounds and Nucleic Acids modified with a Unique Phosphorous and Trifluoromethyl Group

5.1 Introduction

REDOR, as introduced in chapter 3, is an experiment widely used in solid-state NMR to measure dipolar couplings between two nuclei. This coupling is quantified as a dephasing of spin coherences on an observed nucleus caused by a coupled spin. The amount of dephasing observed is directly related to the internuclear distance of the two spins from the dipolar coupling. Because the dipolar coupling constant, D, is measured in the REDOR experiment, the internuclear distance, r, between spin pairs can be determined by the inverse relationship of D and r as shown in the following expression

$$D \propto \frac{\gamma_I \gamma_S}{r_{I-S}^3} \tag{5.1}$$

where γ is the gyromagnetic of the spin. The dipolar coupling constant is proportionally related to the gyromagnetic ratio of the coupled spins and spins with large gyromagnetic ratios leads to measurement of long distances.

The phosphorous nucleus not only has a high gyromagnetic ratio and is 100 % naturally abundant in its NMR active form but also is found in biological molecules such as nucleic acids and enzymes. A few examples of internuclear distances greater than 10 Å that have been reported for biomolecules using $^{31}P\{^{19}F\}$ REDOR include a protein binding site [42,43], double stranded DNA

[44] and DNA-drug complex [45] with measured internuclear distances of approximately 16, 12, and 13 Å, respectively. Thus, ^{31}P NMR is a useful nucleus for the study of biological molecules.

This work presents the technique of measuring long-range internuclear distances by $^{31}P\{^{19}F\}$ REDOR by taking advantage of the natural abundance of the phosphorous spin and the high gyromagnetic ratio of fluorine. By dephasing with three fluorines from a rotating $-CF_3$ group instead of a single fluorine, the use of $^{31}P\{^{19}F\}$ REDOR for molecules containing a $-CF_3$ group allows the measurement of long distance restraints, greater than 10 Å and less than 20 Å, which is useful in global structure determination of biological systems especially those with phosphoruous as in nucleic acids. $^{31}P\{^{19}F\}$ REDOR experiments were performed on small model compounds and model biomolecules to determine a difference in ^{31}P-^{19}F dephasing due to the presence of a trifluoromethyl group. Thus, this study 1) compares the difference in dephasing between a single fluorine and three fluorines of a rotating trifluoromethyl group for several distances, 2) describes situations when substituition of –F with $-CF_3$ group is advantageous, and 3) estimates the potential maximum distance that a phosphorous coupled to three fluorines in a rotating $-CF_3$ group can measure using $^{31}P\{^{19}F\}$ REDOR.

5.2 $^{31}P\{^{19}F_3\}$ REDOR

5.2.1 Orientation and Theoretical Dephasing Curves of $-CF_3$ group

The orientation of the fluorines from a $-CF_3$ group with respect to the phosphorous atom can range from 0° to 90°. Figure 5.1A depicts the 0° orientation where the ^{31}P atom lies along the C_3 axis of the $-CF_3$ group while the 90° orientation shown in Figure 5.1B is where the ^{31}P atom is in the plane of the

three fluorines. In both orientations, the distance simulated is from the center of mass of the three fluorines to the ^{31}P atom.

The simulated $^{31}P\{^{19}F\}$ REDOR dephasing curves for P-F and P-CF_3 are compared at several distances 6, 9, and 12 Å as shown in Figure 5.2. For each distance, there are three simulated curves, where the solid line represents the dephasing for a given distance between a ^{31}P atom and a single ^{19}F atom. The dotted and dashed lines describe the P-CF_3 simulations where the C_3 axis of the -CF_3 group is oriented at its extreme of either 0° or 90° with respect to the ^{31}P atom, respectively. At 6 Å, the P-F and P-CF_3 dephasing curves are similar to one another, while in the 12 Å case the dephasing curves for the P-CF_3 are much more dephased than for the P-F case.

5.2.2 P-F and P-CF_3 Model Compound REDOR Results

Several model compounds were synthesized and investigated in this study. The purpose of the model compounds was to find a suitable setup compound for calibration of experimental parameters and to ensure the accuracy of the distances measured by $^{31}P\{^{19}F\}$ REDOR.

The first column of Table 5.1 shows the model compounds (**1-7**) that were synthesized or purchased where each compound contains either a unique fluorine atom or –CF_3 group and phosphorous atom. The compounds **1** and **2** were specifically designed such that the internuclear distance between ^{31}P and ^{19}F would be set and would not vary due to bond rotations. Compounds **3** and **4** were synthesized to measure a longer distance than **1** and **2**, however, the theoretical distance for both **3** and **4** have an approximate 1.5 Å range measureable due to possible rotation of C-O bond of the phosphate group. The phosphoramidites, **5** and **6** were also measured using REDOR prior to being incorporated into the DNA molecules. Another model compound, **7** was also

studied since it fulfilled the requirements of having a CF_3 group and phosphate and thought to be a good candidate as a model compound.

Two separate sources were used to determine the theoretical ^{31}P to ^{19}F distances of the model compounds used. The first method was a structural minimization using a semi-empirical AM1 closed shell calculation with software provided by Cambridge Soft Corporation [46]. In addition, the Cambridge Structure Database (CSD) was searched for compounds or fragments of compounds similar to **1-7**. The distances on the basis of the CSD data for structurally similar fragments were in good agreement with the minimized structures from the AM1 calculations. Thus, the AM1 calculations were sufficient for theoretical distances of the model compounds (**1-7**) and are shown in Table 5.1.

The REDOR dephasing curves of the P-F and P-CF_3 labeled model compounds diluted and undiluted are shown in Figures 5.3 to 5.8 of compounds **1-7**. The experimental distance measurements for the model compounds are tabulated in Table 5.1 Of all the model compounds studied, **1** and **2** had the shortest distance to be measured. Figure 5.3 shows the overlapped dephasing curves of **1** and **2** each diluted in KBr (1:100 mol ratio) along with the simulations. The P-F REDOR data for compound **1** is shown as solid squares and the line is the corresponding simulation at 6 Angstroms. For compound **2**, the P-CF_3 REDOR data is depicted as solid triangles and the long and short dashed lines correspond to the 90 and 0 degree P-CF_3 orientation simulations at 6 Angstroms. Figure 5.4 is the P-F REDOR dephasing curve of model compounds **3** and **4** which are diluted at 10mg/uL H_2O and 1:40 benzoic acid, respectively. There is a definite difference in the amount of dephasing between the two curves. Compound **3** is best fitted to the 9 Angstoms P-F simulation and

the data of compound **4** fit between the P-CF_3 8 and 9 Angtrom simulations. Figure 5.5 show the compounds of **3** and **4** not diluted in any medium. There is not a distinctive difference in the two dephasing curves of the compounds as compared when the samples are diluted. Figure 5.6 illustrates the undiluted and diluted case of compound **4** where the dilution makes a difference in isolating the spins such that intermolecular couplings are not interfering.

5.2.3 P-F and P-CF_3 REDOR DNA Results

The sequences and labeling scheme of the DNA used in this study are shown in Table 5.2 and are labeled as molecules **8-10**. The DNA sequence used has been characterized by X-Ray crystallography (PDB: 1BDN) and is used as a model nucleic acid to ensure the REDOR technique is able to measure comparable distances to crystallographic data.

When comparing the REDOR dephasing curves of a DNA oligomer as (shown in Figure 5.9) with a trifluoromethyl group and a single fluorine substituted in the same position, the dephasing curve of the DNA with the trifluoromethyl group exhibits more dephasing than the DNA with a single fluorine. As described above, the effective phosphorous-fluorine dipolar coupling is larger in the system with the trifluoromethyl compared to a single fluorine. The moderate distance of 12 Å measured in the duplex DNA were self-diluting and thus the experimental distances were comparable with the X-ray crystal structure measurements [47].

In order to test the limitations of the ^{31}P-^{19}F REDOR technique with a –CF_3 biomolecule, phosphorothioate and -CF_3 labels were incorporated into a DNA (**10**) where the labels are 20 Å as measured in the X-ray crystal literature (1BDN). The sequence and labeling scheme is shown below,

5'd(C G C A T T T T $^{5\text{-}CF_3}$U T G C G)-3'

3'd(G C-(pS)-G T A A A A A C G C)-5'.

The REDOR dephasing curve was measured at several different hydration levels as well as lyophilized or unhydrated. In the unhydrated case and for a hydration of 10 water molecules per base, also noted as W = 10, the distance measured was 14 Å. A shorter distance may be due to the DNA being in A form and/or the P-F spins are not adequately diluted. At a hydration of W = 14, the distance was not measureable at 15 ms of dephasing which would be the minimum evolution time necessary to determine the distance at 20 Å. Due to the small number of labeled phosphorothioate spins (1.5E-6), the phosphorothioate peak was undecipherable from the noise in the baseline after 15 ms of evolution at a proton field of 200 MHz.

5.3 Discussion of P-F and P–CF_3 REDOR Studies

From the dephasing curves, it can be seen that the molecules with a -CF_3 group exhibit more dephasing than the single fluorines. In addition, the diluted and undiluted samples were co-plotted and reveal less dephasing due to dilution of the sample.

The distances measured from the REDOR experiments were shorter than the expected theoretical distances most likely due to intermolecular effects and possible aggregation of the fluorines [48-50]. Attempts were made to dilute the sample so intermolecular effects may be avoided. However, as dilution of sample increased, the signal to noise diminished.

Simulations were performed by Vinodh Raghunathan to describe possible packing models of the compounds where the intermolecular effects give rise to a

distribution of distances. These results are discussed in the 'P-CF_3 REDOR' draft in Appendix C.

Table 5.1 reveals that the experimental distances measured were shorter than the expected theoretical distances. At long distances greater than 12 Å, the distance to be measured shows a decreasing dependence upon the orientation of the –CF_3 group, and thus the amount of dephasing is nearly the same. However, at short distances (~ 6 Å), the orientation of the –CF_3 group is more sensitive than at distances above 12 Å. Figure 5.2 shows that at 6 Å the 90° orientation dephases faster than the 0° orientation. At short distances, the difference in distance from the ^{31}P atom to the center of mass of the three fluorines compared to the distance from the ^{31}P atom to any one of the fluorines becomes significant and thus, the orientation of the -CF_3 group is relevant at short distances rather than long distances. At longer distances (>12 Å), the three fluorines of the –CF_3 group collectively can thus be considered as a "pseudo-atom".

There is in fact a change in the dephasing curves due to the substitution with a -CF_3 group. Due to an increase in dephasing when utilizing a -CF_3 group as a label, it is hopeful that an internuclear distance of up to 20 Å can be measured. Table x theoretically compares the amount of dephasing between P-F and P-F_3 and shows that a distance of 20 Å has 8% dephasing after 30 ms evolution for a P-F_3 system, which is an estimate of the upper limit of detection. To determine the minimum amount of dephasing needed to measure a 20 Å distance, a phosphorous sample (NaH_2PO_4) without any fluorine was run under the same experimental REDOR conditions as all fluorinated samples.

In deciding when to include a –CF_3 group or –F in a sample depends on the information desired, the system of interest, and placement of the label. Besides being able to measure a long-range distance with a –CF_3 group, there is

an advantage of a $-CF_3$ group at short distances, as well. For distances not more than ~6 Å, the orientation of the $-CF_3$ group relative to the phosphorous nucleus is rather sensitive, if the error in the dephasing data points are low. Figure 5.3 illustrates that the simulations of the 6 Å 0° and 90° dephasing curves do not overlap and are distinguishable enough to determine the orientation of the $-CF_3$ group relative to the phosphorous nucleus. The first three experimental points of the sodium p-(trifluoromethyl)phenyl phosphate dephasing curve, indicated by triangles, are in good agreement with the theoretical P-F_3 6Å 90° dephasing curve (long dashes). Due to the C-O-P arrangement in the sodium p-(trifluoromethyl)phenyl phosphate, the $-CF_3$ group is situated 90° relative to the phosphate atom which is in agreement with the experimental result. As a result of intermolecular effects, at longer dephasing times (greater than 5 ms), the experimental results no longer follow the 6Å 90° dephasing curve. At distances greater than 6Å, the theoretical P-F_3 0° and 90° dephasing curves begin to converge and so the orientation of the $-CF_3$ group can no longer be realized. As seen in our results, a disadvantage of incorporating a $-CF_3$ group is when the molecule of interest is inadequately diluted and/or the distance measured is large compared to the size of the molecule, intermolecular effects are a consequence. Thus, the –F label is best used when measuring short distances in order to avoid intermolecular effects and no longer having isolated spin pairs.

In addition, a $^{31}P\{^{19}F\}$ REDOR null experiment was performed on the solid sample, NaH_2PO_4, due to the absence of fluorine and presence of a phosphorus atom. The NaH_2PO_4 dephasing curve in Figure 5.11 shows results of the null difference experiment. Thus, in order to measure a distance of ~ 20 Å would require a dephasing time of at least 25 ms to distinguish 6% dephasing.

5.4 Conclusion

In a ^{31}P-^{19}F spin system, REDOR recouples the direct dipolar coupling between the two nuclei. This coupling is quantified as a dephasing of spin coherences on the observed nucleus (e.g. ^{31}P) caused by the coupled spin (e.g. ^{19}F). The amount of dephasing observed is directly related to the internuclear distance of the two spins from the heteronuclear dipolar coupling. By replacing a single fluorine spin with three fluorine spins of a trifluoromethyl group, the dipolar coupling and, hence, the dephasing is enhanced and thus, a long internuclear distances of up to 20 Angstroms may be measureable.

5.4.1 Future Applications of P-F/F_3 REDOR

By incorporating a -CF_3 group and a phosphorothiate, to produce a chemical shift from the phosphate backbone, into a biomolecule such as an RNA, the technique of $^{31}P\{^{19}F\}$ REDOR can be used to determine structure in nucleic acids, either DNA or RNA.

Since DNA and RNA are not isolated molecules and their environments are heterogenous and many times their structure is influenced by other molecules (drugs, enzymes or ligands) and environemental factors such as pH, ionic strength, temperature or hydration level, creative labeling schemes or methods are being developed to address ways to determine structure in such complex multi-component systems with a wide range of environmental factors.

Table 5.1 Theoretical and ^{31}P-^{19}F REDOR measured distances of model CF and CF_3 compounds used.

	r_{PF} (Å) distance	r_{PF} (Å) measured
1 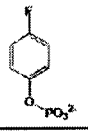	6.6	6.0 ± 0.9 (1:100 mol/mol KBr) 6.2 ± 1.0 (1:5 mol/mol benzoic acid) 6.0 ± 1.0 (1:20 mol/mol benzoic acid)
2 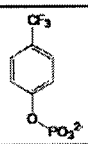	7.4	6.0 ± 0.8 (1:100 mol/mol KBr)
3 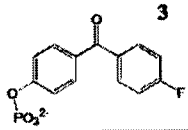	11.2 (10-11.2)*	9.0 ± 0.9 (undiluted) 9.5 ± 1.1 (10mg/30μL) 9.3 ± 1.8 (10mg/60μL)
4 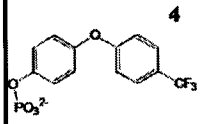	10.9 (10-11.5)*	8.3 ± 3.7 (undiluted) 9.3 ± 2.7 (1:40 mol/mol benzoic acid)
5 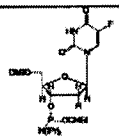	7.3 (7.1-9.0)*	6.4 ± 1.4 (undiluted)
6 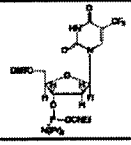	7.6 (7.4-9.5)*	6.0 ± 1.8 (undiluted)
7 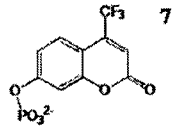	7.8 (7.5-8.3)*	7.2 ± 1.2 (undiluted) 6.4 ± 1.9 (1:30 mol/mol benzoic acid) 6.5 ± 0.5 (1:60 mol/mol benzoic acid)

* Range of distance due to rotation of phosphate or phosphoramidite group.

Table 5.2 X Ray crystal data and ^{31}P-^{19}F REDOR measured distances of model CF and CF_3 dsDNA used

ds DNA	r_{PF} (Å) (X-Ray Crystal)	r_{PF} (Å) (^{31}P-^{19}F REDOR)
8 5'd(CGCAT T-(pS)- TT $^{5-F}$UGCG)-3' 3'd(G C G T A A A A A C G C)-5'	11.9 (PDB: 1BDN)	12 ± 1 (W=14)
9 5'd(C G C A T T-(pS)- T T $^{5-CF3}$ U T G C G)-3' 3'd(G C G T A A A A A C G C)-5'	11.2 (PDB: 1BDN)	13 ± 2 (W=14)
10 5'd(C G C A T T T T $^{5-CF3}$U T G C G)-3' 3'd(G C-(pS)-G T A A A A A C G C)-5'	19.9 (PDB: 1BDN)	14 ± 2 (W=0) 12 ± 1 (W=3) 14 ± 2 (W=10) 13 ± 1 (W=14)

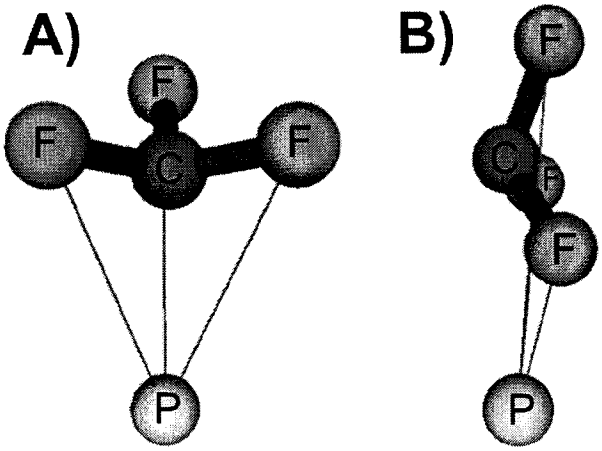

Figure 5.1 CF_3 0 and 90 degree orientation relative to phosphorous atom.

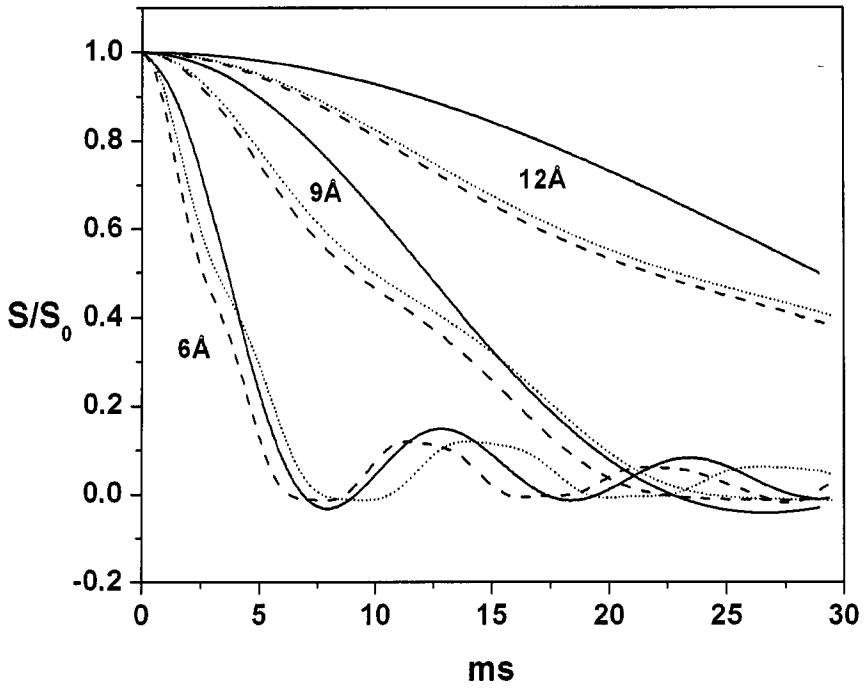

Figure 5.2 Simulated dephasing curves at 6, 9 and 12 Angstroms for P-CF_3 for 0 and 90 degree orientations compared to P-F.

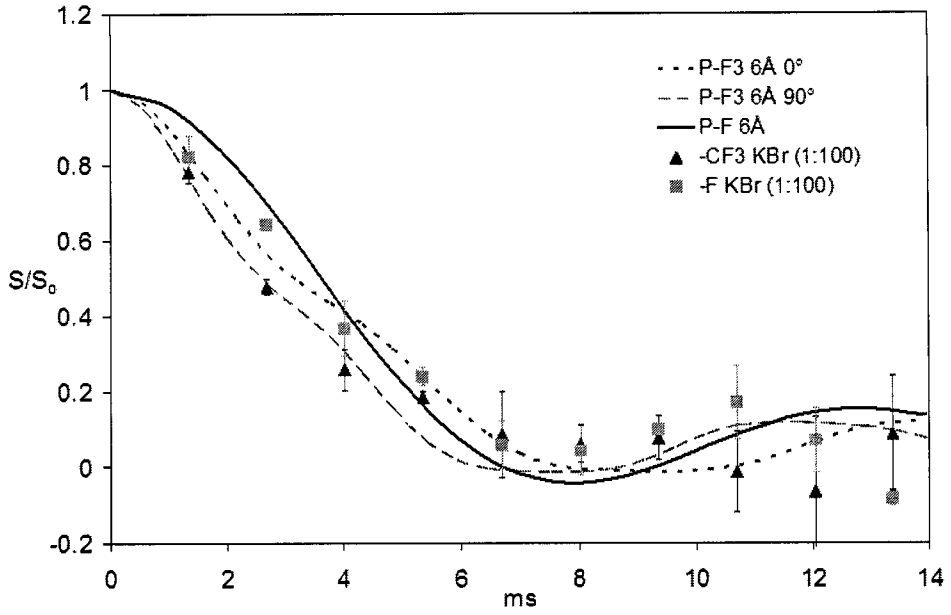

Figure 5.3 $^{31}P\{^{19}F\}$ REDOR dephasing curve of model compounds **1** and **2** diluted in KBr (1:100 mol ratio). Solid triangle compound **1**; solid square compound **2**; dashed lines and short dashed lines are simulations of $P\text{-}F_3$ 6Å 90 and 0 degree, respectively. The solid line is the simulation of P-F for 6 Å.

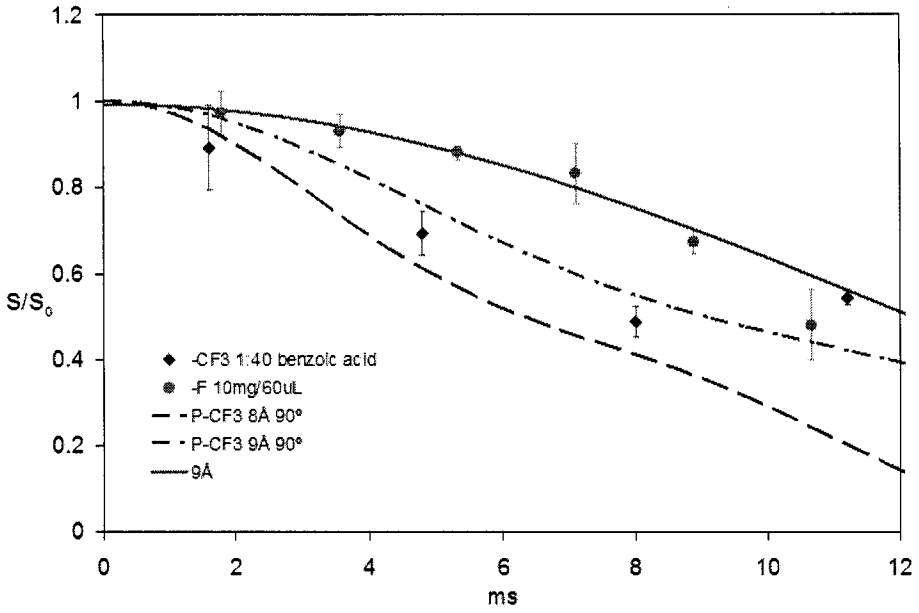

Figure 5.4 $^{31}P\{^{19}F\}$ REDOR dephasing curve of model compounds **3** and **4** diluted in 10mg/uL water and 1:40 benzoic acid, respectively. Solid diamond compound **3**; solid circles compound **4**; dashed dot and dashed lines are simulations of PF_3 90 degree 9Å, and 8Å respectively. The solid lines are simulations of P-F for 6 and 7 Å.

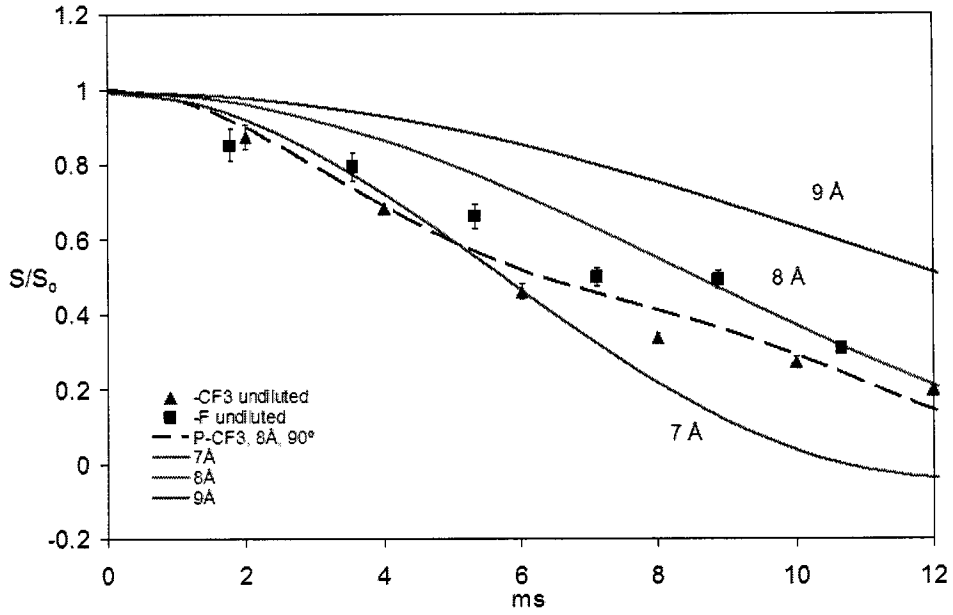

Figure 5.5 $^{31}P\{^{19}F\}$ REDOR dephasing curve of model compounds **3** and **4** undiluted. Solid triangle compound **3**; solid square compound **4**; dashed lines are simulations of $P\text{-}F_3$ 90 degree 8Å. The solid lines are the simulations of P-F for 7, 8 and 9 Å.

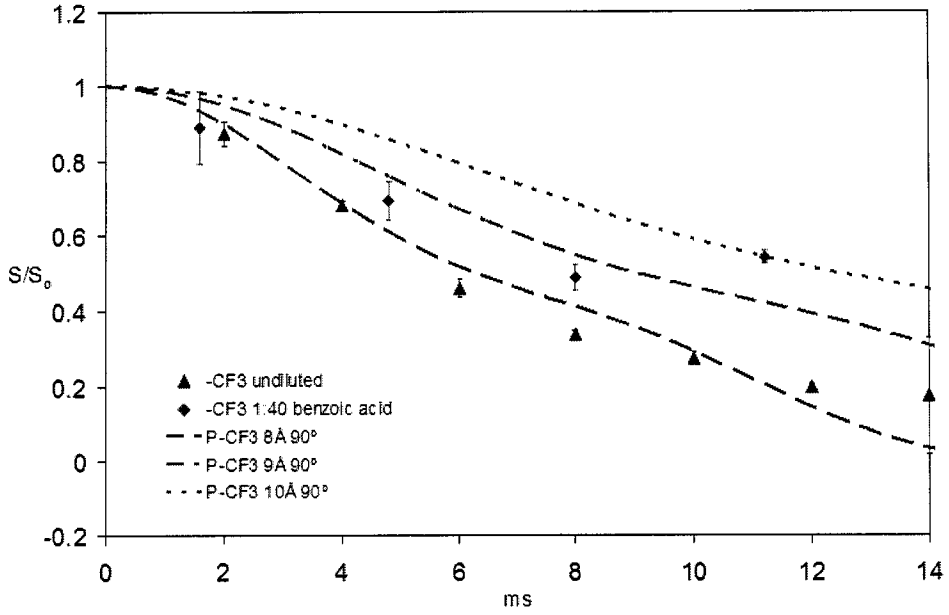

Figure 5.6 $^{31}P\{^{19}F\}$ REDOR dephasing curve of model compound **4** undiluted (solid triangle) and diluted in 1:40 benzoic acid (solid diamond). Dashed lines and dashed dots are simulations of $P\text{-}F_3$ 90 degree 8Å, and 9Å respectively. The short dashes is the simulation of P-F for 10 Å.

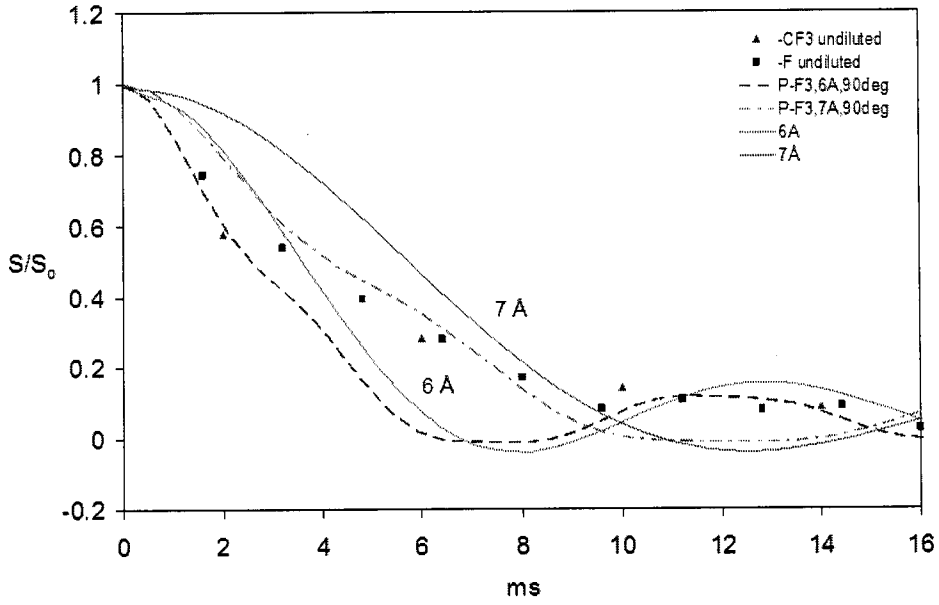

Figure 5.7 $^{31}P\{^{19}F\}$ REDOR dephasing curve of model compounds **5** and **6** undiluted. Solid triangle compound **5**; solid square compound **6**; dashed dot and dashed lines are simulations of $P\text{-}F_3$ 90 degree 7Å, and 6Å respectively. The solid lines are simulations of P-F for 6 and 7 Å.

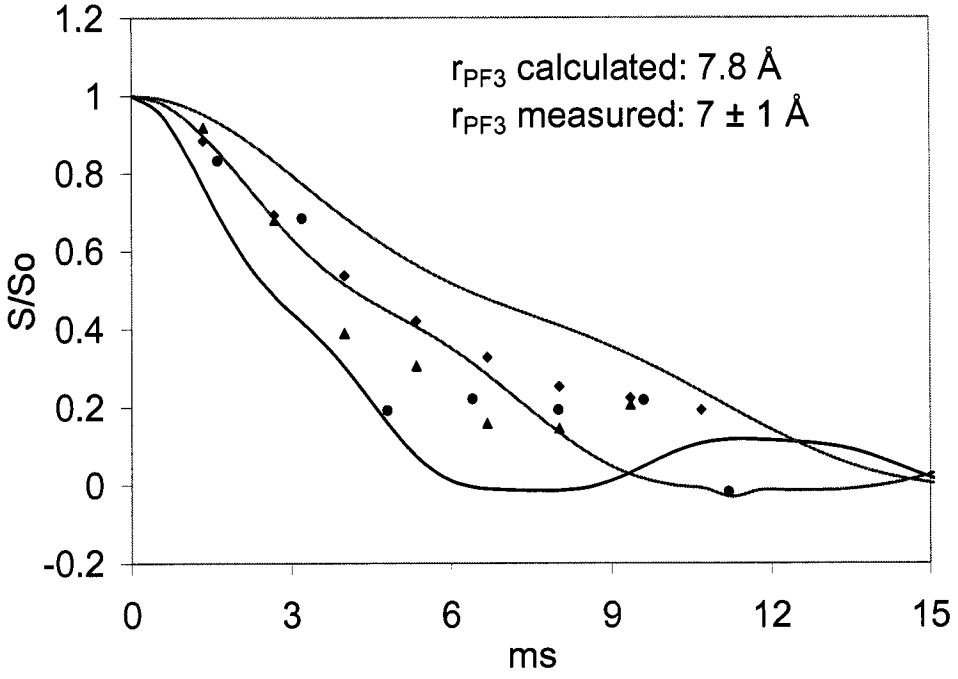

Figure 5.8 $^{31}P\{^{19}F\}$ Redor dephasing curves of compound **7**. Diamonds: compound **7** undiluted; triangles are compound **7** diluted 1:30 in benzoic acid, and dots are compound **7** diluted 1:60 in benzoic acid. Simulations (lines) are shown for P-CF_3 6, 7 and 8 Å.

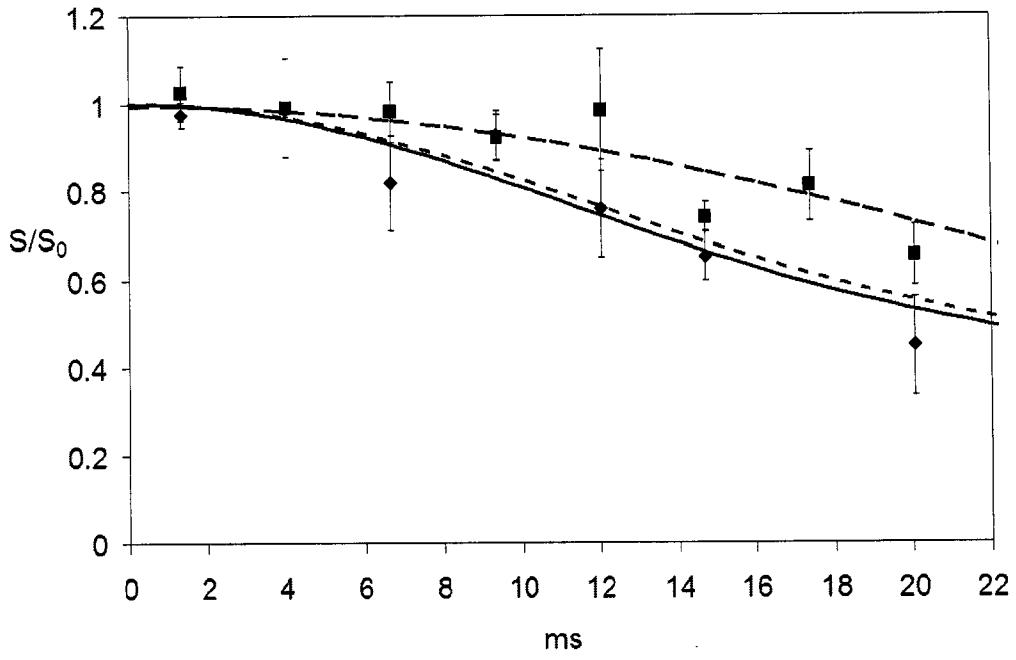

Figure 5.9 $^{31}P\{^{19}F\}$ Redor dephasing curves. Experimental data for dsDNA **8** (filled diamonds) and **9** (filled squares). The lines are simulated REDOR curves, long dashed lines P-F 12 Å, short dashed lines P-F_3 12 Å 0 °, solid line P-F_3 12 Å 90°.

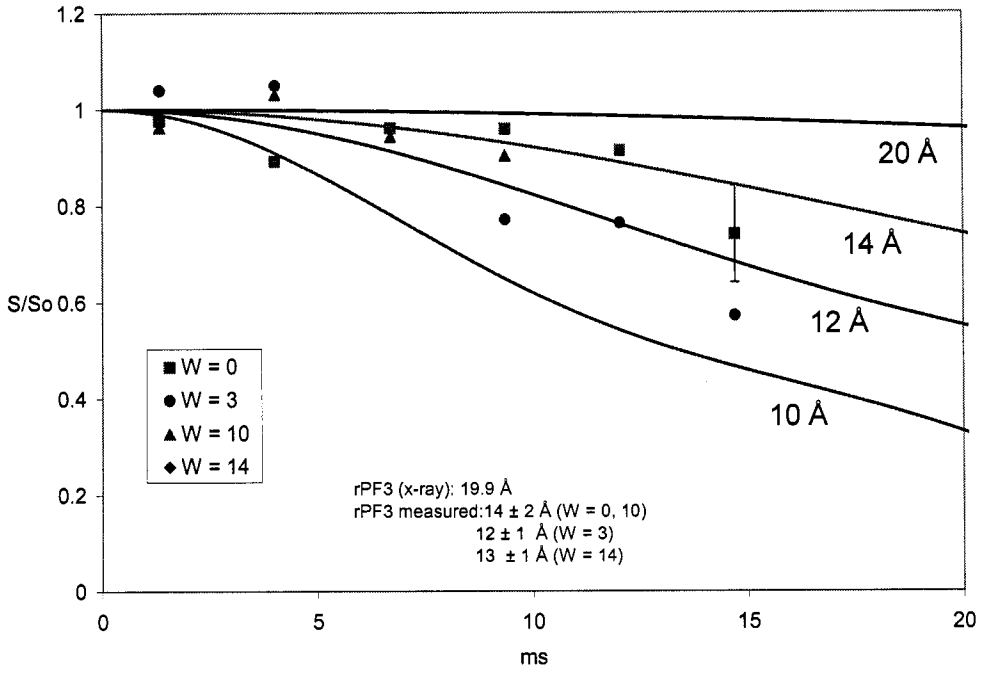

Figure 5.10 $^{31}P\{^{19}F\}$ REDOR dephasing curves at several hydration levels for dsDNA (**10**) with phosphorthioate and $-CF_3$ label 20 Angstroms apart as measured from the crystal structure, 1BDN. Sequence of dsDNA: 5'd(C G C A T T T T $^{5\text{-}CF_3}$U T G C G)-3' and 3'd(G C-(pS)-G T A A A A A C G C)-5'.

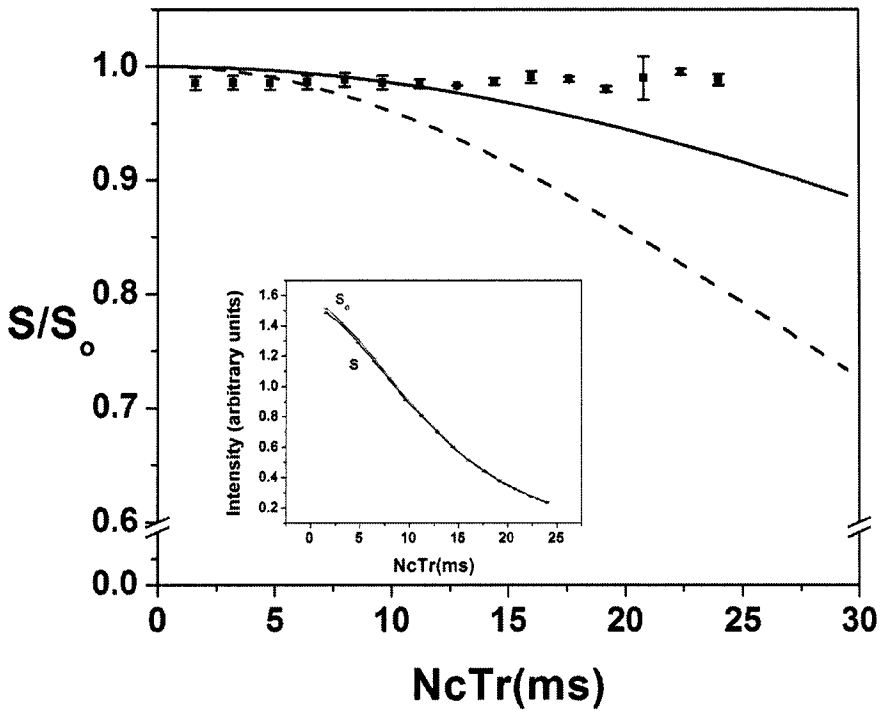

Figure 5.11 $^{31}P\{^{19}F\}$ REDOR curves of solid Na_2HPO_4 (experimental points), and 19 Angstrom simulations of P-F (solid line) and P-F_3 (dashed line). Inset is overlay of S and S_0 curves of the Na_2HPO_4 experimental data.

Chapter 6: Using ^{13}C DQ DRAWS NMR to Determine Secondary Structure of Peptides in Varying Environments

6.1 Introduction

The information gathered from studying the structure of peptides and proteins can provide information regarding the function of these biological molecules or interactions for drug design, biological implants, biological assays, or cell adhesion. In this chapter, two different peptides were studied using the solid-state NMR homonuclear recoupling experiment, DQ DRAWS, to monitor a change in secondary structure of two different peptides in various environments. Secondary structure of a peptide (α-helix vs β-sheet) can be distinguished by inspection of a 2D DQ DRAWS interferogram as will be discussed in section 6.4.

The peptides in this study are gramicidin A and LKα-14 which were placed in unhydrated and hydrated environments of lipid bilayers and carboxylated polystyrene beads, respectively. A brief background of the peptides are in the next two sections and then, the results of gramicidin A and LKα-14 are revealed and examined.

6.1.1 Description of Gramicidin A

Gramicidin A (gA) is a hydrophobic linear polypeptide antibiotic produced by Bacillus brevis. It contains 15 hydrophobic residues with alternating L- and D- amino acids with the N-terminus blocked by a formyl group and the C-terminus by an ethanolamine. The primary sequence of gA is HCO-L-Val-Gly-L-Ala-D-Leu-L-Ala-D-Val-L-Val-D-Val-L-Trp-D-Leu-L-Trp-D-Leu-L-Trp-D-Leu-L-Trp-$NHCH_2CH_2OH$. The peptide forms β helices with a

hydrogen bonding pattern of the backbone similar to that in β sheets due to the alternating sequence of L and D amino acid residues. Gramicidin A can adopt a variety of conformations depending on its environment being that it is a relatively small and flexible polypeptide. The many conformations of gA are classified into two major types: single-stranded (ss) helical dimer or double stranded (ds) helical dimer. The ss dimer has two single-stranded helices associated head to head at the N-terminus as shown on the left in Figure. 6.1 A. The double helical dimer shown on the right in Figure. 6.1 A and can be formed under certain conditions where the two strands run parallel or antiparallel. Figure 6.1 B illustrates the conformation of the ss dimmer in a lipid bilayer.

Gramicidin A is one of the best characterized, widely studied peptide and many methods have been used to determine gA's structure. In the literature, the structure of gA has been studied by CD [51,52], X-ray crystallography [53][Langs 1988,], solution NMR [54-57], and solid state NMR[39,58-68]. The conformational behavior of gA depends highly on its environment. Depending on the organic solvent used to dissolve gA, there are several possible structures. In ethanol, gA rapidly interconverts between four different double helix conformations (head to head, head to tail, and the antiparallel double helix conformation being the dominant form. [51,69] In trifluoroethanol or DMSO, gA is a structured monomer.[70,71] When gA is co-dissolved in SDS micelles [72] or oriented in bilayers [66] a helical head-to-head dimer is formed.

The purpose of using gA as a model peptide is to confirm that DQ DRAWS can accurately determine the secondary structure of a peptide in a membrane. The results for the gA studies are reported in section 6.3.

6.1.2 Description of LKα-14

The LKα-14 peptide is a 14 amino acid peptide composed of leucine and lysine residues organized in a fashion when structured as an α-helix the leucines and lysines form distinct hydrophobic and hydrophilic regions of the peptide, respectively, which makes it a good peptide to study at interfaces [73]. Previous studies using ssNMR of the LKα-14 peptide have involved adsorbing the peptide to polystyrene [29] as well as covalent attachment to gold particles [25]. In this study, LKα-14 was first studied as a function of adsorption to several different polystyrene beads with charged surface modifications such as a amino, carboxylate, and sulfate groups. Fluorimetry was used to determine the amount of peptide adsorbed to the various polystyrene bead surfaces. In addition photon correlation spectroscopy also known as Dynamic Light Scattering (DLS) was used to determine the particle size to check for aggregation of particles. The Double Quantum (DQ) filtered dipolar recoupling experiments were used to determine the secondary structure of the peptide adsorbed to the functionalized polystyrene bead.

6.2 Results of Gramicidin A

Gramicidin A was studied without DMPC and with DMPC unhydrated and hydrated. In determining secondary structure of gA in the different environments, the carbonyls of amino acids gly_2 and ala_3 were ^{13}C labeled. ^{13}C CPMAS spectra were obtained at several spinning speeds. The results of the DRAWS, DQ DRAWS, and 2D DQ DRAWS experiments are discussed below.

6.2.1 NMR Studies of Gramicidin A

The following sections are the NMR results of the gramicidin A peptide studies with and without a phospholipids unilamellar vesicle. The results of the CPMAS, DQDRAWS, and 2D DQDRAWS experiments applied are shown.

6.2.1.1 CPMAS

In Figure. 6.2, the ^{13}C CPMAS spectra of dry gA without and with DMPC at 3, 4 and 8 kHz spinning speeds are shown. As the spinning speed increases, the CPMAS spectra of gA shows an increase in intensity of the central carbonyl peak. However, the CPMAS spectra of the gA with DMPC show the opposite effect where the central band decreases in intensity as the spinning speed is increased. In addition, the CPMAS spectra of gA in DMPC reveal more narrow peaks compared to the CPMAS spectra of gA without DMPC.

6.2.1.2 DRAWS

The DRAWS experiment was performed on gA that had been dissolved in methanol and air dried. The DRAWS dephasing curve is shown in Figure 6.3 and the natural abundance ^{13}C has been subtracted. The experimental data could not be fitted to any one of the 3.2 Å - 3.5 Å DRAWS dephasing curves. Due to the incomplete dephasing from the 9th to 12th DRAWS cycle (~5 ms), this indicates that the aggregate is not well defined and is not in a distinct conformation or is in an extended conformation.

6.2.1.3 DQDRAWS

The DQDRAWS spectra are shown in Figure 6.4 and are compared side by side to the CPMAS data collected for gA without DMPC dried from methanol, gA with DMPC dried from methanol, and gA with DMPC 35% hydrated (top to bottom), respectively. The aliphatic resonances can be seen in the CPMAS spectra and are not seen in the DQ spectra. The DQ DRAWS spectra show the effect of efficient double quantum filtering by the absence of the aliphatic resonances in the region of 20-50 ppm.

The buildup curves are shown in Figure 6.5 on the left panel. The points are experimental data and the curves are simulations. From the top to the bottom of the DQDRAWS Buildup curves are gA (dry), gA/DMPC(dry), and gA/DMPC (hydrated). As the environment of the gA changes without DMPC to with DMPC and then hydrated with DMPC, the distance of the ^{13}C labeled carbonyl carbons increases from 3.24, 3.3, and 3.4 Å, respectively. This increase in distance corresponds to an increase in the phi angle for gA alone, gA in DMPC (1:8 mol/mol) dry and gA with DMPC (1:8mol/mol) hydrated. These distances correspond to phi angles of -90°, -100°, and -109.5°, respectively. Table 6.1 summarizes the phi angles and distances found for the gA in the various environments.

6.2.1.4 2D DQDRAWS

The right panel of Figure 6.5 shows the interferograms of the 2DDQDRAWS data with the lines being the fitted simulations. The data of the three interferograms are all different and a noticeable change in the structure of gA is revealed as the environment of gA changes from being dried from methanol or in a lipid dry or hydrated (35%), thus the torsion angles are changing. The gA dried from methanol has a psi = 160.4°, gA in DMPC dry has a psi = +/- 180° and gA hydrated in DMPC, has a psi = 144.8°.

6.2.2 Gramicidin A Structures in the Protein Data Bank

The Protein Data Bank (PDB) [47] was searched for structures of gA and like-gA structures. Table 6.2 shows the PDB file used to measure phi and psi angles for the 3rd amino acid alanine in the gA sequence under various conditions. The result from the 2D DQ DRAWS experiment which revealed a phi and psi for alanine to be (-109.5°, 145°) agrees well with the PDB 1MAG and 1AV2 structures reported by Cross [74] and [75]. Ketchem and Cross

refined initial gA structures against both experimental constraints and CHARMM energy calculations using a simulated annealing protocol to define torsion angles. They report initial and final torsion angles (phi,psi) for residue ala_3 of (-130, 153) and (-115,144), respectively for gA in a lipid environment [76]. Their refined torsion angles are in good agreement with the data collected for the 35% hydrated gA/DMPC sample that was acquired by using 2D DQ DRAWS and run at –45 °C. The sample was run under low temperature conditions due to cross polarization was not efficient at room temperature due to motion of the peptide and thus signal to noise was poor.

6.3 Secondary Structure Distinction with 2D DQ DRAWS

The 2D DQDRAWS simulations of several peptide secondary structures are compared as the CSA values are varied.

6.3.1 Simulations

It is not always feasible to perform the 2D DQDRAWS experiment at long evolution times due to low signal to noise from not enough material to hydrated ionic samples. Overlay of 2D DQDRAWS interferograms for various secondary structure motifs were simulated and compared for several CSA tensor values.

Figure 6.9 shows the interferograms co-plotted of gA alone and gA/DMPC unhydrated and hydrated. The three plots of intensity vs t_1 evolution time show a distinct difference in intensity as time evolves for the gA under different conditions. This clearly shows a distinct change in conformation of gA.

As a result of the changes in conformation due to CSA tensor and, there is a comparison of the interferogram co-plotted for various secondary structures and different CSA tensor values to show that for a known CSA tensor there is a difference in the interferogram as shown in Figures 6.11A-C to determine a

difference or be confident in the results for a particular structure. The only noticeable difference between the simulation of the beta sheet and alpha helix interferograms regardless of the CSA principal values is that the beta sheet simulations do not show an increase or decrease in intensity whereas the alpha helix simulations do. The beta sheet simulations tend to "hover" more so around the x-axis than the alpha helix simulations. This was first observed when performing the 2D DQDRAWS experiment of the gA/DMPC hydrated for a t_1 time of 2 rotor periods or 500 μs. Initially the data was assumed to be bad because there seemed to be no signal intensity in the spectrum. However, when finally simulating the data, it was determined that a β sheet structure shows not as much signal intensity in the 2D DQDRAWS as the alpha helix.

6.4 Results of LKα-14

Adsorption studies and particle sizing studies were implemented as well as NMR studies for the LKa-14 samples with and without surface. The results are in the following sections.

6.4.1 Adsorption Studies

A very sensitive peptide assay using fluorescence detection of amino acids derivatized with o-phthalaldehyde (OPA) was used to assay which of the functionalized polystyrene beads would promote adsorption to the peptide. Figure 4.4 shows the scheme of the derivitization. The most effective functionalized bead that the peptide bound to was the carboxyl-polystyrene microsphere bead when compared to the amine, and sulfate polystyrene beads. The linearized Langmuir adsorption model for the peptide adsorbed to the carboxylate polystyrene showed the number of available binding sites to be 0.327 μmol/m^2 and the affinity of adsorption was 2551 mL/μmol. The Langmuir plots are shown in Figures 6A-C. The carboxylate polystyrene bead adsorbed the

most peptide and therefore, it was chosen for the solid-state NMR study in order to have adequate signal from the ^{13}C labeled peptide.

6.4.2 Particle Sizing

In order to determine if the peptides and beads were aggregating and in what size or what the distribution of size was, several solutions of peptide with and without the carboxylated beads were made. The DLS particle sizing showed that the beads were in fact made within the specifications of the manufacturer and had an effective diameter of 200nm+/-5nm.The peptides in solution (conc) had effective diameters of 15.5, 31, and 52 nm. This suggests that the peptide exsists as monomers, dimers and trimers in solution. When the peptides and the beads were in solution together after being agitated over a 24 hour period this revealed an effective diameter of 440+/-20 nm. This may indicate that the beads and peptides in solution are forming "sandwiches where a peptide dimer is sandwhiched between two carboxylate beads

In addition, the same samples were studied in a a phosphate buffer solution (PBS) of pH 7.4 (11.9 mM Phosphates, 137 mM Sodium Chloride and 2.7 mM (Fischer). When the peptides and carboxylated beads were made with PBS buffer (pH 7.4), the measurements of the diameter were on average 468 nm for the peptide, 235+/-20nm for the bead, and two readings of 470 nm and 800 nm for the peptide and bead in buffer.

The result of the DLS measurements are a qualitative indication that the beads on average associate with another bead in the presence of peptide via the peptide. The diameter measured was most probable in the region of 400 nm which is twice the diameter of the beads when purchased. There seemed to be aggregation of the peptides in buffer due to the size of the aggregates to 468nm In addition, when the carboxylated beads were in buffer, the effective diameters

had increased about 20-50 nm. It is difficult to surmise how the peptides and carboxylaated bead are interacting when in buffer. It is possible that the peptides and beads interact among themselves and not with each other.

6.4.3 NMR Studies of LKα-14

The following sections are the NMR results of the LKα-14 peptide studies with and without a surface. The results of the CPMAS, DQDRAWS, and 2D DQDRAWS experiments applied are shown.

6.4.3.1 CPMAS

The ^{13}C CPMAS spectra of the LKa-14 peptide under various environments are shown in Figure 6.7. The top figure is the ^{13}C CPMAS spectrum of LKα-14 unhydrated, the middle spectrum is the LKα-14 covalently bound to MBHA resin and second from the bottom spectrum is the LKα-14 adsorbed to the 200 nm carboxylate polystyrene beads. This spectrum shows the ^{13}C natural abundance background signal of the charged polystyrene bead overwhelming the signal from the bound ^{13}C carbonyl labeled peptide. The very bottom spectrum is the ^{13}C CPMAS of the carboxylate beads.

6.4.3.2 DQDRAWS

Figure 6.8 shows the DQDRAWS buildup curves for the LKα-14, LKα-14 covalently bound to resin and the LKα-14 adsorbed to the carboxylate bead. As the peptide is set in various environments, the structure changed and the ϕ angle changed as well. LKα-14 covalently bound to the resin has a ϕ of -84 degrees and when cleaved form the resin, the ϕ angle of LKα-14 increases to -63 degrees. The LKα-14 when placed in the presence of the carboxylated bead, the structures changed from a ϕ of 63 to -57 degrees. In addition, Figure 6.8 shows

the DQ filtered spectra inset under the buildup curves. When comparing the DQ filtered spectra to those of the CPMAS spectra, it can be seen that the natural abundance ^{13}C background signals contributed by the peptide and carboxylated bead are adequately filtered.

6.4.3.3 2D DQDRAWS

The 2D DQDRAWS results revealed that the ψ angle of the LKα-14 covalently bound to the resin was remarkedly different from the other two cases of where the LKα-14 was either in the absence or presence of the carboxylated bead.

6.5 Discussion of Peptide Studies

Solid-state NMR has been used to characterize the secondary structure of lipid proteins using dipolar recoupling techniques such as rotational resonance and REDOR. These methods are useful when there is a chemical shift difference or α-helix/3_{10} structure, respectively. Because rotational resonance requires a chemical shift difference, this may require an elaborate labeling scheme. In the case of REDOR, an α-helix or 3_{10} structure is measured by the i $\rightarrow$ i+4 (^{13}C carbonyl $\rightarrow$ ^{15}N amide) distance which is approximately 4 Å. Thus, using REDOR with the i $\rightarrow$ i+4 peptide labeling, the distance limit measureable for the $^{13}C\{^{15}N\}$REDOR is 5 Å as a result of the low gyromagnetic ratios of the nuclei. Due to the 5 Å distance limit, $^{13}C\{^{15}N\}$ REDOR can provide a negative result for the β-helix structure since the distance is 8 Å.

The DQ DRAWS dipolar recoupling solid-state NMR experiment is able to efficiently remove the overwhelming natural abundance background in the sample such that it is possible to detect signal from a labeled peptide to determine the secondary structure of peptides within polyelectrolyte layers. An

immediate goal includes designing solid-state NMR experiments to determine the interaction (contact points) of the charged peptide and the functionalized polystyrene microsphere. Changes in structure of an amphipathic peptide, peptide covalently bound on resin, and peptide adsorbed to surface by electrostatics can be monitored by solid-state NMR.

6.6 Practical Aspects

Samples with limited amount of material or constrained by rotor size and working with biological or material complexes such as heterogeneous systems, two-dimensional solid-state NMR experiments can become quite long. For example, a hydrated peptide in the presence of lipids with the parameters listed in Table 6.3 would require an acquisition time of 121.4 days or approximately 4 months. If this experiment is to be repeated 2 more times for statistical averaging, then one complete data set of three runs would require 1 year which is quite unacceptable when time and equipment unfortunately are not a luxury. There are several solutions to the problem with the obvious being increase the amount of sample or use of a larger sample holder. However, in NMR these options are not always feasible. Samples used are usually isotopically labeled and expensive as well as requiring time laboring synthetic and purification skills. As for a larger sample holder, solid-state NMR is limited to the length and diameter of the coil and the stator in the probe.

A practical aspect about the 2D DQ DRAWS experiment for biological molecules is the ability to run the experiment for t1 delay values of up to 1 or 2 rotor periods if there is not enough sample or time is a constraint. In the past, the group usually performed both the real and imaginary experiments. This is not realistic when spectrometer time is a constraint. However by cutting out the imaginary collection of data and only acquiring within 2 rotor periods for the

same number of 16384 scans and a 4 second relaxaxtion delay, one can acquire 1 set of data in a little over 2 weeks and for a total of three runs this would require a minimum of 1.5 months. Thus, a much more realistic amount of time for an experiment and a more useful time spent of valuable spectrometer time.

Since membrane proteins can be dynamic, the hydrated samples had to be performed at low temperature to slow down or "freeze" out some of the motion. The DQ DRAWS experiments allowed the measurement of effective ϕ and ψ angles as demonstrated by using a model peptide such as gramicidin A.

In the case of the LKα-14 adsorbed to the carboxylated polystyrene beads, even with a very large and nearly overlapping carbon signal from the phenyl rings, the DQ DRAWS pulse sequence effectively filtered the signal from uncoupled spins so as to detect and observe only the spins which are recoupled.

6.7 Conclusion

The structure of peptides and proteins is a growing field now that the genome project has been completed. DNA codes for the proteins made and by understanding the function of a protein through its structure is ongoing work among many scientists. What becomes more difficult to study are the membrane proteins due to their hydrophobic nature. By isolating membrane proteins from their membrane environment may change their structure and thus may not be as biologically active. Ongoing methods to study proteins are in pursuit as well as discovering new ways to approach the daunting task of characterizing all the many proteins known and those unknown. The benefit to understanding the structure and the function of proteins is for the ultimate design to improve the quality of life by discovering new methods to fight disease, design new drugs, or make better biomaterials. Solid-state NMR is a method that can help in this

pursuit because it is a versatile technique that can probe biological molecules in various environments.

Table 6.1 Summary of distance measurements and torsion angles of gA studied under various conditions. The torsion agles (phi,psi) of gA in DMPC reported by Ketcham et al. [76] were (-115,145).

	gramA unhydrated 23 °C	gramA/DMPC (1:8) unhydrated 23 °C	gramA/DMPC (1:8) ~35% hydrated -45 °C
DRAWS	extended conformation	N/A	N/A
DQDRAWS Buildup	3.2 Å ϕ = -90	3.3 Å ϕ = -100	3.4 Å ϕ = -109.5
2D DQDRAWS	ψ =160.4	ψ = +/- 180	ψ = 144.8

Table 6.2 Structure of gramicidin A or gA-like peptides found in the PDB [47] are tabulated below with the distance and (phi, psi) angles of the 3rd amino acid, alanine.

PDB	distance, Å	Phi	Psi	Solvent	Method
1AL4	3.622 3.600	-149.3 -138.9	128.6 141.1	propanol	X-ray
1ALX	3.550 3.621	-135.6 -151.3	135.1 151.9	methanol	X-ray
1ALZ	3.623 3.614	-151.8 -139.8	137.8 126.4	ethanol	X-ray
1AV2	3.430 3.358 3.382 3.316	-111.0 -96.0 -109.8 -98.3	145.0 145.0 149.9 143.0	CsCl	X-ray
1BDW	3.526 3.540	-126.4 -125.0	147.0 152.6		X-ray
1C4D	3.749 3.802 3.790	168.1 160.1 175.2	112.8 108.7 102.1	CsCl	X-ray
1GMK	3.581 3.564 3.745 3.538	-134.9 -125.5 178.1 -127.3	105.4 153.5 103.1 114.4	Kscn	X-ray
1GRM	3.644 3.645	-153.4 -153.4	144.4 144.3		NMR
1JNO	3.421 3.421	-99.5 -99.4	115.0 115.0	SDS	Solution NMR
1MAG	3.426 3.426	-109.7 -109.7	148.6 148.6	DMPC	Solid NMR
1MIC	3.704 3.698	-180 -172.4	155.6 156.1	$CaCl_2$/ methanol	NMR
1NG8	3.723 3.722	-149.4 -149.4	150.4 150.5	SDS	NMR
1NRM	3.702 3.702	-145.6 -145.7	114.4 114.4	DDPC	NMR
1NRU	3.377 3.376	-95.5 -95.5	130.7 130.7	DDPC excess Na+	NMR
1TKQ	3.288	-98.3	121.1		

Table 6.3 List of experimental parameters for a several mmol biological sample.

Scans	16384
Relax (s)	4
T1 dwell (s)	2.5 e-5
Experiments	160 (80 real + 80 imaginary)

A)

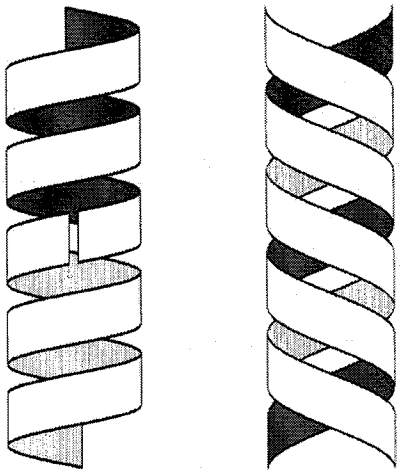

B)

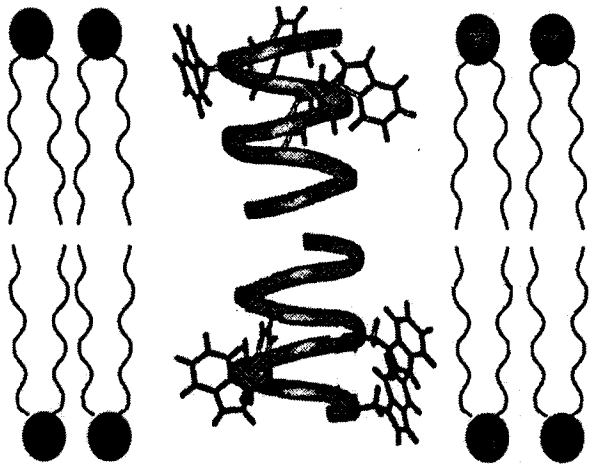

Figure 6.1 A) Schematic structures of gramicidin A as dimers. Left: single stranded head to head dimer. Right: double stranded dimer, can either be anti parallel or parallel. B) Schematic of gramicidin in a phospholipid bilayer where the typtophan residues are shown near the phospholipid head groups and the ethanolamine. (Adapted from M. Cotten Florida State University Thesis 1998)

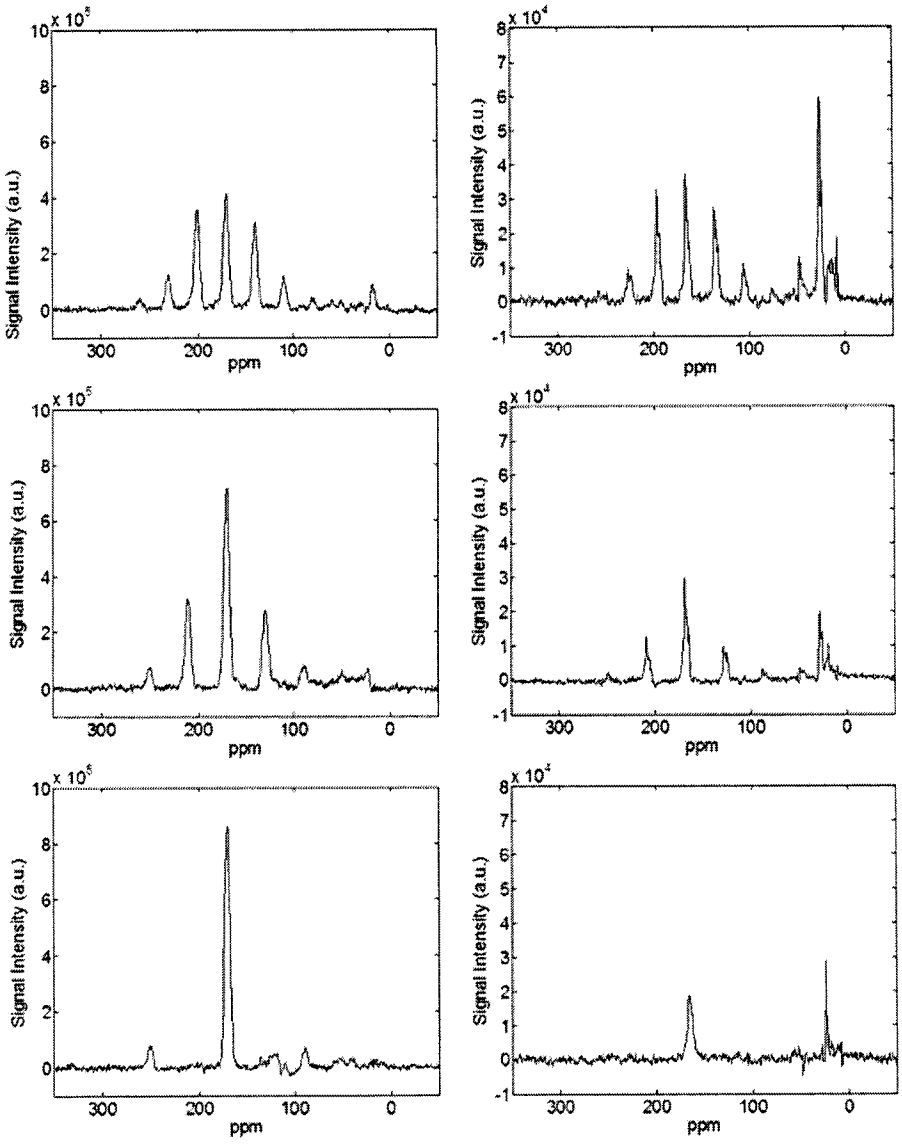

Figure 6.2 ^{13}C CPMAS of gramicidin A dry without and with DMPC at several spinning speeds, 3, 4 and 8 kHz. The left panel is the ^{13}C CPMAS spectra of gramicidin A dry without DMPC at 3, 4, and 8 kHz (top to bottom). The right panel is the ^{13}C CPMAS spectra of gramicidin A with DMPC dry at 3, 4 and 8 kHz (top to bottm).

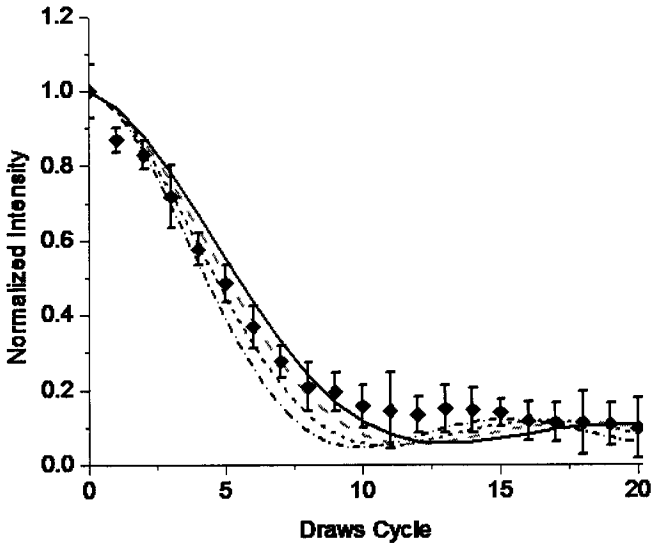

Figure 6.3 ^{13}C DRAWS dephasing curves of dry gA at room temperature. Dash dot 3.2Å; short dash 3.3Å; long dash 3.4Å; and line 3.5Å. Solid diamond gramicidin A (dry) experimental data. Spinning speed of 4 kHz. One DRAWS cycle is 4 rotor periods.

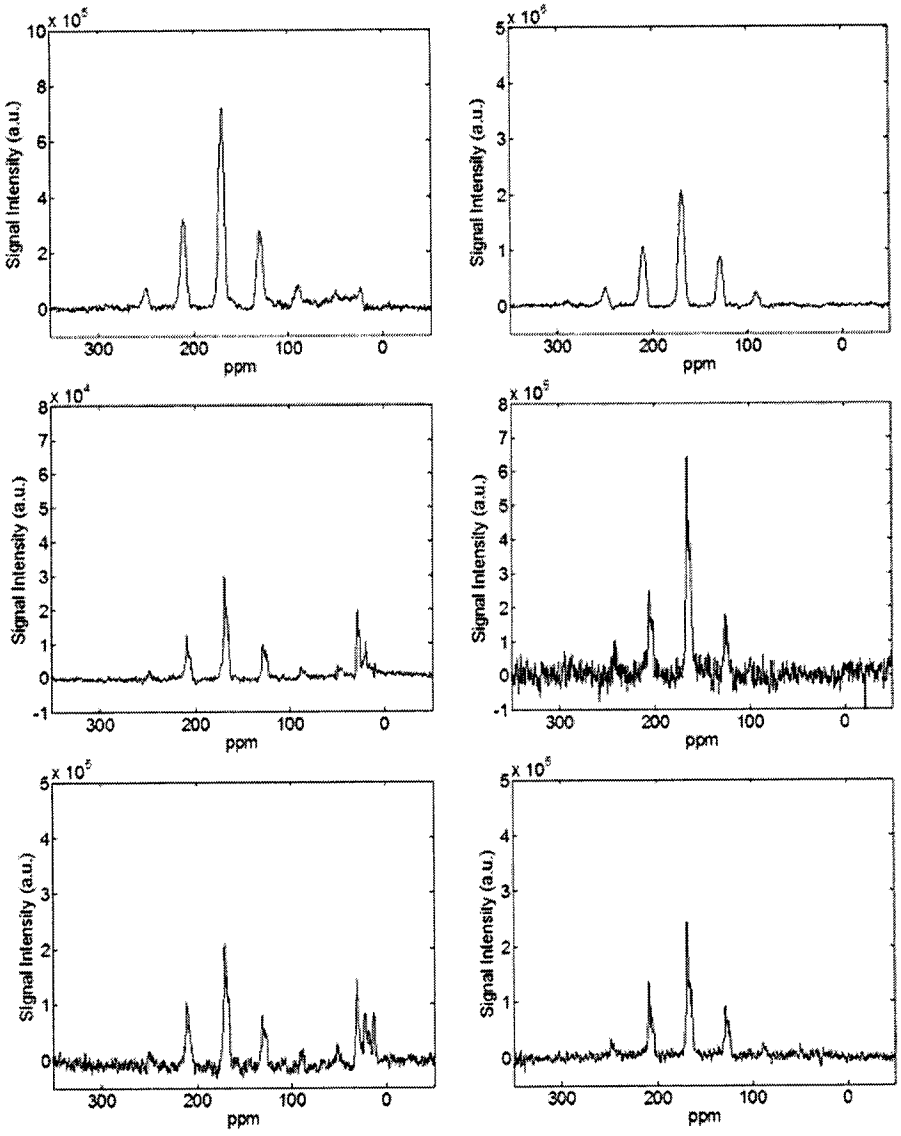

Figure 6.4 ^{13}C CPMAS and DQDRAWS spectra of 1-^{13}C-g_2,a_3-gA. Left panel ^{13}C CPMAS of 1-^{13}C-g_2,a_3-gA without DMPC dry, with DMPC dry and with DMPC 35% hydrated (top to bottom), respectively. Right panel ^{13}C DQDRAWS filtered spectra of 1-^{13}C-g_2,a_3-gA without DMPC dry, with DMPC dry and with DMPC 35% hydrated (top to bottom), respectively.

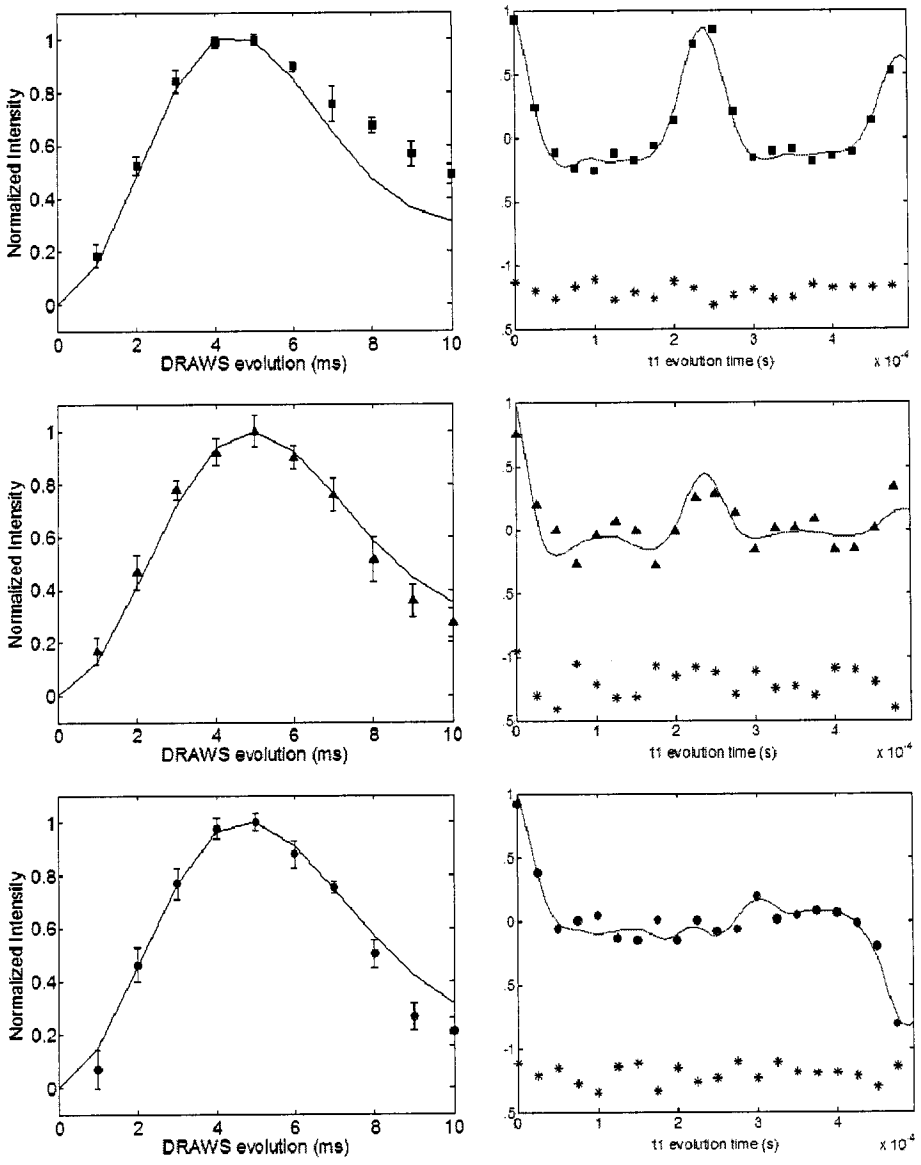

Figure 6.5 Left panel: DQ DRAWS Buildup Curves of gA. Right Panel: 2D DQ DRAWS interferograms of gA. Top to Bottom: gA dry; gA in DMPC 1:8 mol ratio dry; and gA in DMPC 1:8 mol ratio 35% (w/w) hydrated. Points are experimental data and lines are fitted simulations. The (*) astericks are the residuals. As the conditions of the gA change there is a noticeable difference in the interferogram which reflects a change in gA conformational structure.

Fluorimetric Analysis for Adsorption Studies:

Derivatization with *o*-phthaladehyde

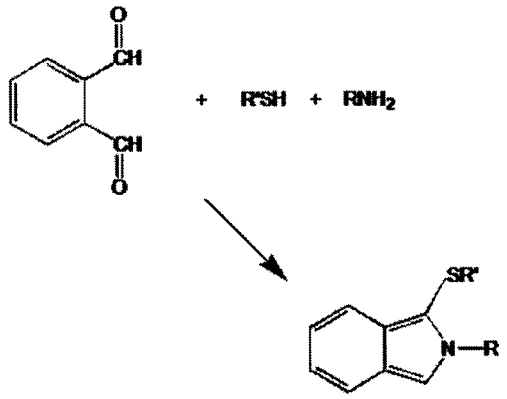

excitation: 360 nm
emission: 445 nm

Figure 6.6 Scheme of fluoroaldehyde which is used to derivitize the amine groups to quantify adsorption of peptide to beads by measuring the concentration of unadsorbed petide.

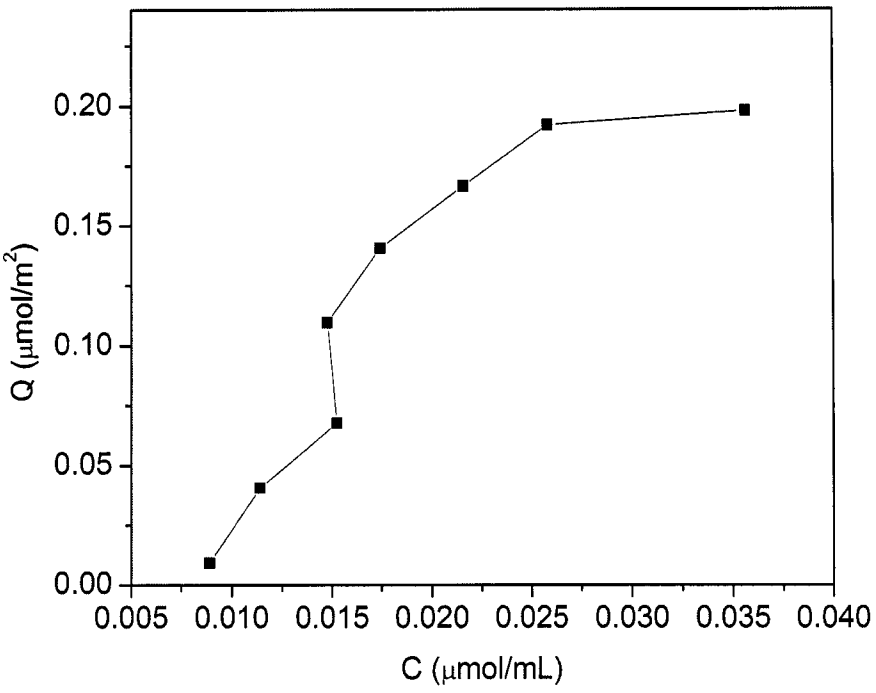

Figure 6.7 A) Langmuir plot of LKα-14 with amine-polystyrene bead.

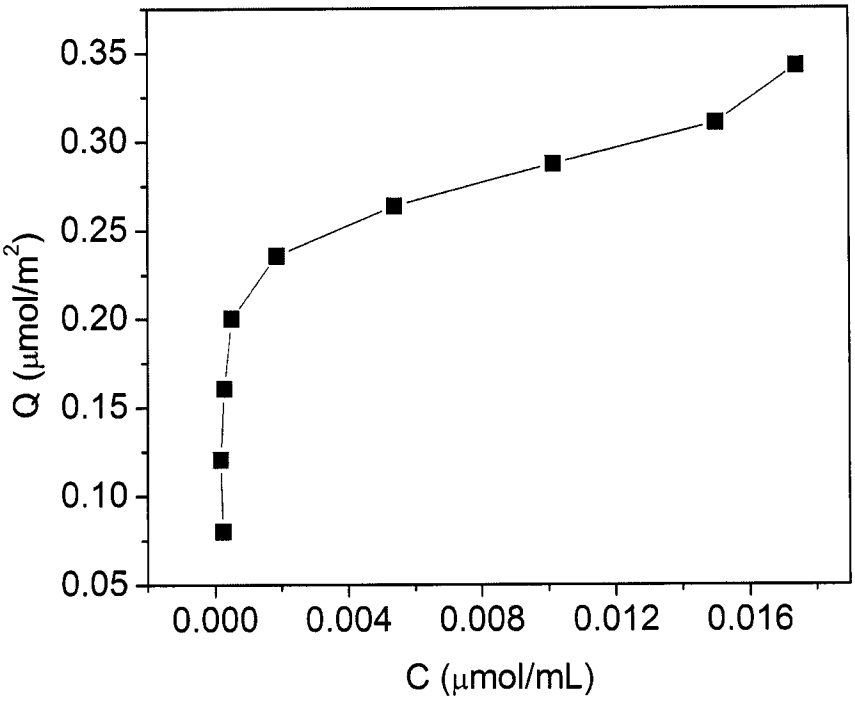

Figure 6.7 B) Langmuir plot of LKα-14 with carboxylate polystyrene bead.

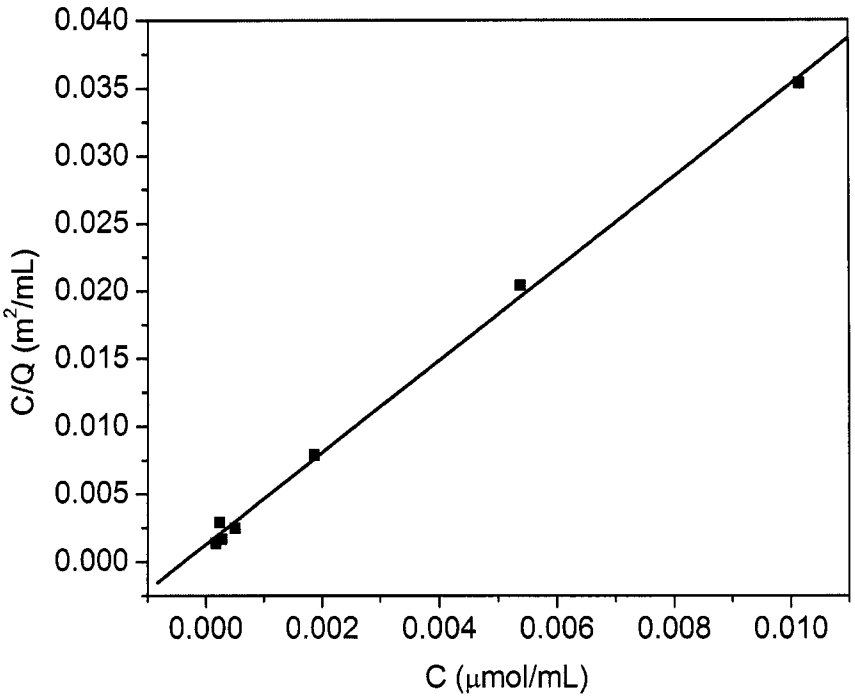

Figure 6.7 C) Langmuir linearized plot of LKα-14 with carboxylate polystyrene bead. The best fit line gives N = 0.327 and K = 2551 where N is the number of available binding sites and K is the affinity of adsorption.

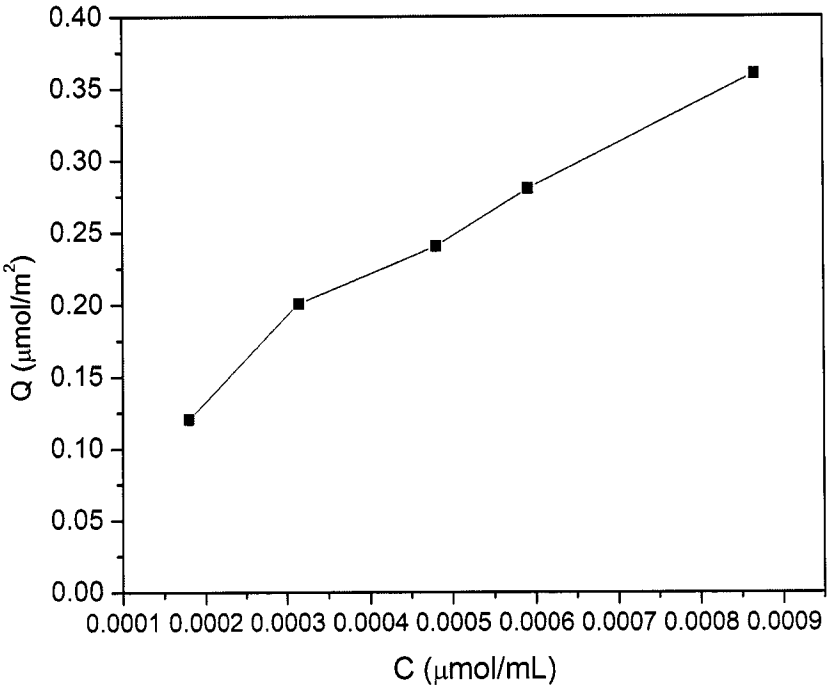

Figure 6.7 D) Langmuir plot of LKα-14 with sulfate polystyrene bead.

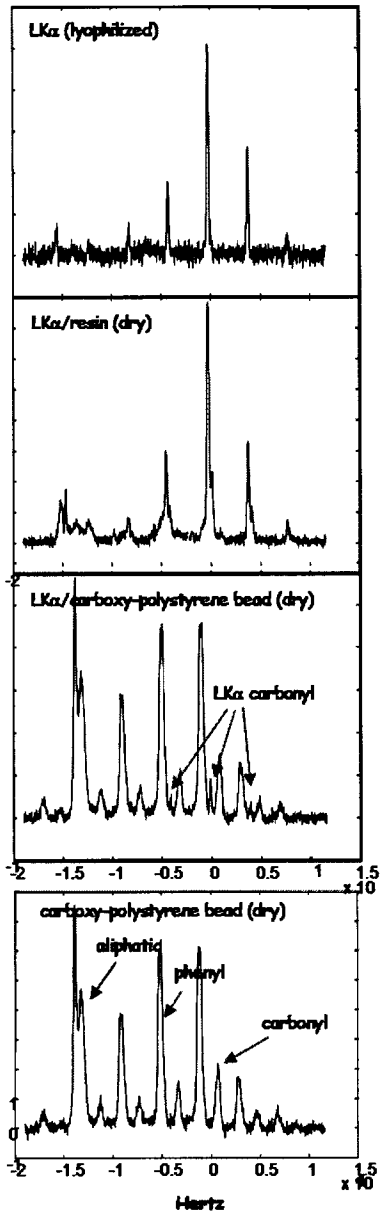

Figure 6.8 ^{13}C CPMAS spectrum of peptide in various environments. (top to bottom) LKα-14 lyophilized, LKα-14 bound to MBHA resin, LKα-14 bound to carboxylated polystyrene bead (dry), and carboxylated polystyrene bead (dry) without any peptide.

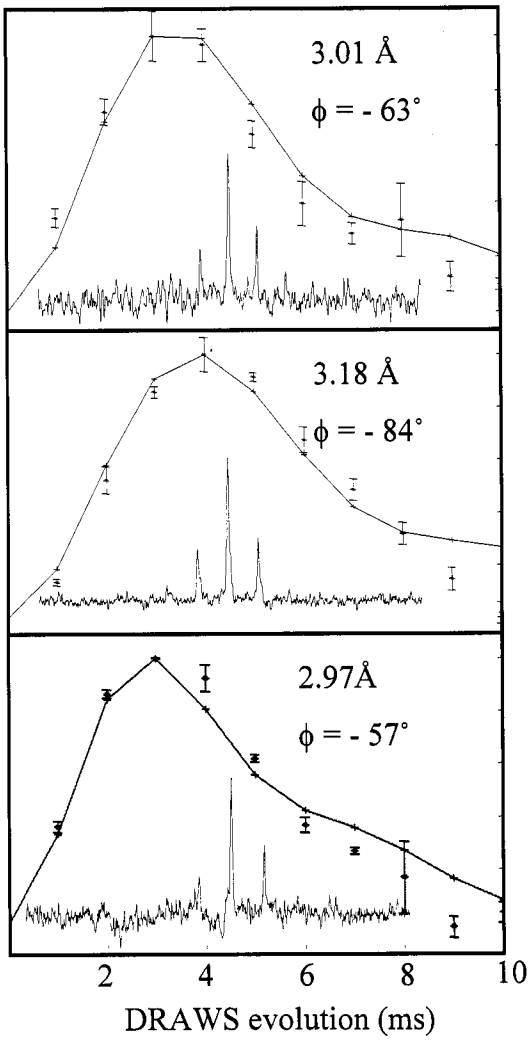

Figure 6.9 DQ DRAWS Buildup curves and DQ DRAWS spectra for LKα-14. From top to bottom unhydrated LKα-14, unhydrated LKα-14 covalently coupled to MBHA resin, unhydrated LKα-14 adsorbed to carboxylate polystyrene bead. The background signal from carboxylated polystyrene bead does not appear due to the DQ filter.

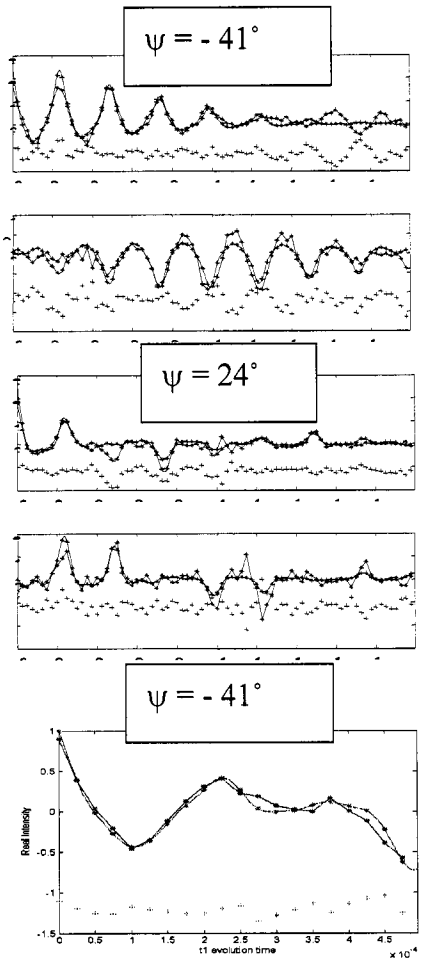

t1 evolution time

Figure 6.10 2D DQ DRAWS interferograms. From top to bottom: unhydrated LKα-14, unhydrated LKα-14 covalently coupled to MBHA resin, unhydrated LKα-14 adsorbed to carboxylated polystyrene bead.

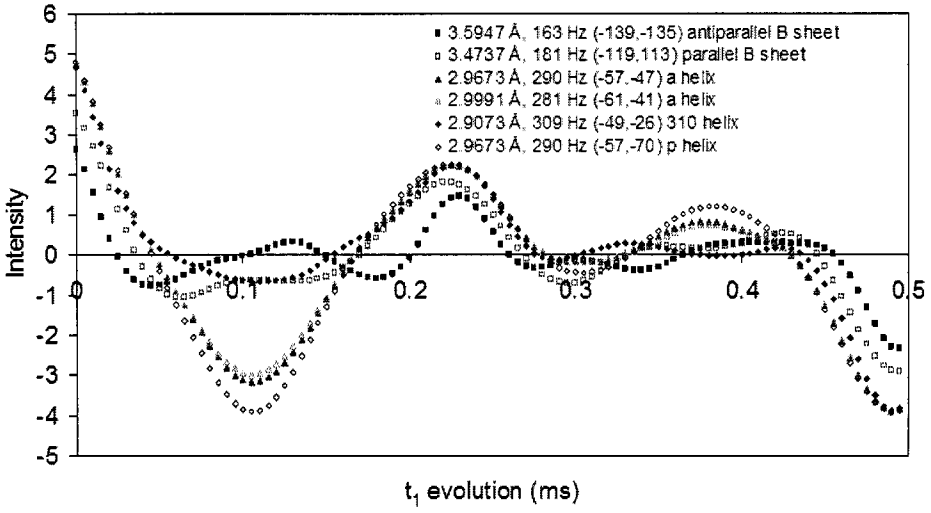

Figure 6.11 A) 2D DQ DRAWS simulations with CSA of (74.546, 6.131, -79.124) for various secondary structures.

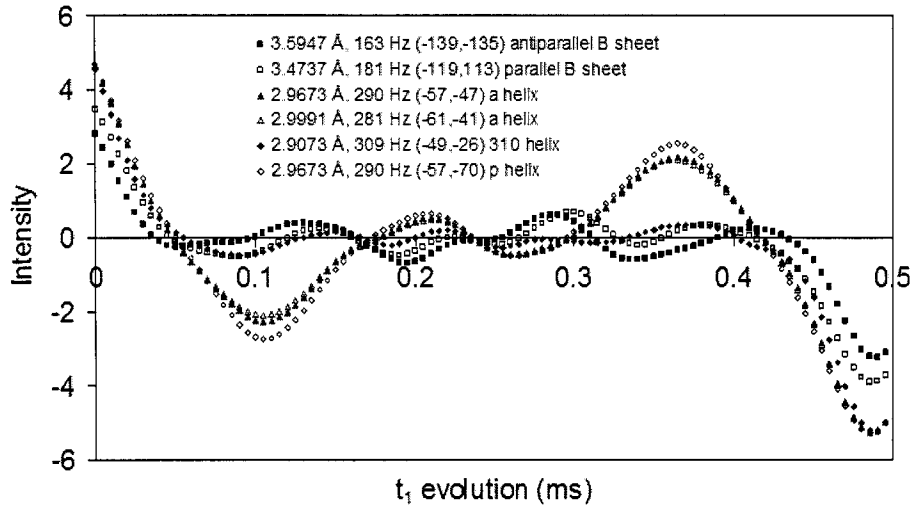

Figure 6.11 B) 2D DQ DRAWS simulations with CSA of (64.352, 17.965, -87.051) for various secondary structures.

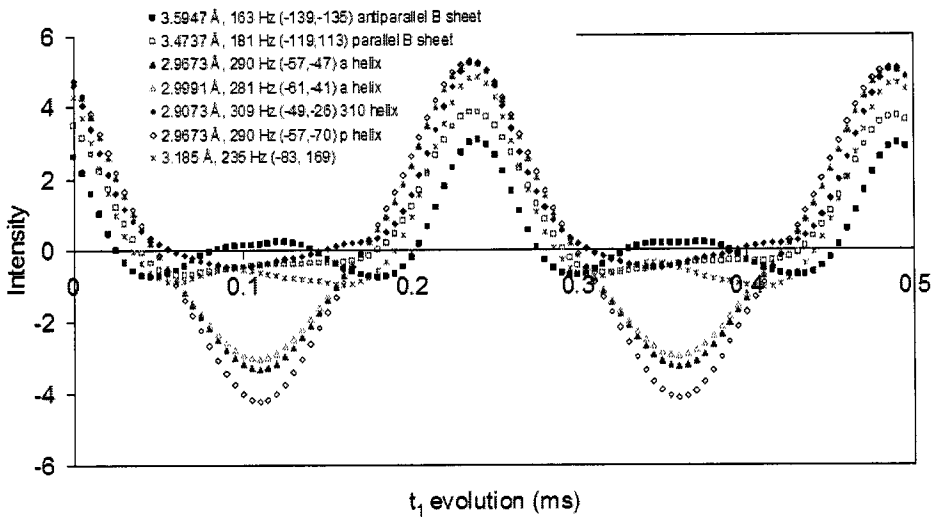

Figure 6.11 C) 2D DQ DRAWS simulations with CSA of (84, -11, -73) for various secondary structures.

Chapter 7: Conclusions and Final Thoughts

Solid state NMR is at its inception in being a useful and complimentary technique for structure determination of biomacromolecules and biological systems. There is ongoing work in development of new techniques and methods to approach this daunting task of studying various biological heterogeneous systems.

Magnetic resonance is a versatile non-invasive non-teratogenic technique that can study samples in the form of gas , liquid, and solid or even a combination of phase under most conditions such as a change in concentration., temperature, pressure, and pH. Thus, magnetic resonance techniques (NMR, MRI, and MRS) are useful in all aspects of life or various industries from studying food, wine, colloids, surface science, psychology, tissues, nerves and use as a medical diagnostic. The hurdle to defeat is the sensitivity of the technique which is an on-going challenge.

Bibliography

[1] J.B. Chaires, Drug-DNA interactions, Current Opinion In Structural Biology, 8 (1998) 314-320.

[2] P.B. Dervan, Molecular recognition of DNA by small molecules, Bioorganic & Medicinal Chemistry, 9 (2001) 2215-2235.

[3] S. Neidle, DNA minor-groove recognition by small molecules, Natural Product Reports, 18 (2001) 291-309.

[4] A.L. Lehninger, D.L. Nelso, M.M. Cox, Principles of Biochemistry, (1993).

[5] T.E. Creighton Proteins: Structures and Molecular Properties, Second ed.; W.H. Freeman and Company: New York, 1984.

[6] B.D. Ratner, A.S. Hoffman, F.J. Schoen, J.E. Lemons Biomaterial Science: An Introduction to Materials in Medicine; Elsevier: San Francisco, 2004.

[7] R.R. Sniden, DNA Structure and Function, (1994).

[8] F. Bloch, W.W. Hansen, M. Packard, Phys. Rev., 69 (1946) 37.

[9] E.M. Purcell, H.C. Torrey, R.V. Pound, Phys. Rev., 69 (1946).

[10] D.M. Grant and R.K. Harris Encyclopedia of Nuclear Magnetic Resonance; John Wiley, and Sons: New York; Vol. 1.

[11] E.R. Andrew, A. Bradbury, R.G. Eades, Nature (London), 182 (1958) 1659.

[12] I. Lowe, Phys. Rev. Lett., Phys. Rev. Lett., 2 (1959) 285.

[13] E.O. Stejskal, J. Schaefer, J.S. Waugh, Magic-Angle Spinning And Polarization Transfer In Proton-Enhanced Nmr, Journal Of Magnetic Resonance, 28 (1977) 105-112.

[14] T. Gullion, Introduction to rotational-echo, double-resonance NMR, Concepts In Magnetic Resonance, 10 (1998) 277-289.

[15] G.P. Drobny, J.R. Long, T. Karlsson, W. Shaw, J. Popham, N. Oyler, P. Bower, J. Stringer, D. Gregory, M. Mehta, P.S. Stayton, Structural studies of biomaterials using double-quantum solid-state NMR spectroscopy, Annual Review Of Physical Chemistry, 54 (2003) 531-571.

[16] T. Gullion and J. Schaefer, Rotational-Echo Double-Resonance Nmr, Journal Of Magnetic Resonance, 81 (1989) 196-200.

[17] T. Gullion and J. Schaefer, Detection of Weak Heteronuclear Dipolar Coupling by Rotational-Echo Double-Resonance Nuclear Magnetic Resonance, Advances in Magnetic Resonance, 13 (1989) 57-83.

[18] T. Gullion and J. Schaefer, Elimination Of Resonance Offset Effects In Rotational-Echo, Double-Resonance Nmr, Journal Of Magnetic Resonance, 92 (1991) 439-442.

[19] J.R. Garbow and T. Gullion, Improvements In Redor Nmr-Spectroscopy - Minimizing Resonance-Offset Effects, Journal Of Magnetic Resonance, 95 (1991) 442-445.

[20] J.M. Goetz and J. Schaefer, REDOR dephasing by multiple spins in the presence of molecular motion, J Magn Reson, 127 (1997) 147-154.

[21] M.L. Gilchrist, K. Monde, Y. Tomita, T. Iwashita, K. Nakanishi, A.E. McDermott, Measurement of Interfluorine Distances in Solids, Journal Of Magnetic Resonance, 152 (2001) 1-6.

[22] R.W. Glaser, C. Sachse, U.H.N. Durr, P. Wadhwani, A.S. Ulrich, Orientation of the antimicrobial peptide PGLa in lipid membranes determined from F-19-NMR dipolar couplings of 4-CF3-phenylglycine labels, Journal Of Magnetic Resonance, 168 (2004) 153-163.

[23] D.M. Gregory, D.J. Mitchell, J.A. Stringer, S. Kiihne, J.C. Shiels, J. Callahan, M.A. Mehta, G.P. Drobny, Windowless Dipolar Recoupling - The Detection Of Weak Dipolar Couplings Between Spin-1/2 Nuclei With Large Chemical-Shift Anisotropies, Chemical Physics Letters, 246 (1995) 654-663.

[24] P.V. Bower, N. Oyler, M.A. Mehta, J.R. Long, P.S. Stayton, G.P. Drobny, Determination of torsion angles in proteins and peptides using solid state NMR, Journal Of The American Chemical Society, 121 (1999) 8373-8375.

[25] P.V. Bower, E.A. Louie, J.R. Long, P.S. Stayton, G.P. Drobny, Solid-state NMR structural studies of peptides immobilized on gold nanoparticles, Langmuir, 21 (2005) 3002-3007.

[26] M. Gilbert, W.J. Shaw, J.R. Long, K. Nelson, G.P. Drobny, C.M. Giachelli, P.S. Stayton, Chimeric peptides of statherin and osteopontin that bind hydroxyapatite and mediate cell adhesion, Journal Of Biological Chemistry, 275 (2000) 16213-16218.

[27] T. Karlsson, J.M. Popham, J.R. Long, N. Oyler, G.P. Drobny, A study of homonuclear dipolar recoupling pulse sequences in solid-state nuclear magnetic resonance, Journal Of The American Chemical Society, 125 (2003) 7394-7407.

[28] J.R. Long, J.L. Dindot, H. Zebroski, S. Kiihne, R.H. Clark, A.A. Campbell, P.S. Stayton, G.P. Drobny, A peptide that inhibits hydroxyapatite growth is in an extended conformation on the crystal surface, Proceedings Of The National Academy Of Sciences Of The United States Of America, 95 (1998) 12083-12087.

[29] J.R. Long, N. Oyler, G.P. Drobny, P.S. Stayton, Assembly of alpha-helical peptide coatings on hydrophobic surfaces, Journal Of The American Chemical Society, 124 (2002) 6297-6303.

[30] J.R. Long, W.J. Shaw, P.S. Stayton, G.P. Drobny, Structure and dynamics of hydrated statherin on hydroxyapatite as determined by solid-state NMR, Biochemistry, 40 (2001) 15451-15455.

[31] D.M. Gregory The design of new solid-state NMR experiments for use in determining oligonucleotide structure / by David Matthew Gregory, 1996.

[32] N. Oyler. SSNMR methods for determining structure in nucleosides and peptides / Nathan Andrew Oyler, University of Washington, 2000.

[33] S.L. Beaucage and R.P. Iyer, The Functionalization Of Oligonucleotides Via Phosphoramidite Derivatives, Tetrahedron, 49 (1993) 1925-1963.

[34] J.C. Markley, P. Chirakul, D. Sologub, S.T. Sigurdsson, Incorporation of 2 '-deoxy-5-(trifluoromethyl)uridine and 5-cyano-2 '-deoxyuridine into DNA, Bioorganic & Medicinal Chemistry Letters, 11 (2001) 2453-2455.

[35] T.M. Alam and G.P. Drobny, Solid-State Nmr-Studies Of Dna-Structure And Dynamics, Chemical Reviews, 91 (1991) 1545-1590.

[36] J.A. Stringer and G.P. Drobny, Methods for the analysis and design of a solid state nuclear magnetic resonance probe, Rev. Sci. Instrum., 69 (1998) 3384-3391.

[37] J.A. Stringer. The Design and Analysis of Solid State Nuclear Magnetic Resonance Probes for the Determination of Biomolecular Structure, University of Washington, 1998.

[38] J. Gladden and G.P. Drobny. Unpublished work.

[39] C.G. Fields, P.V. Lograsso, T.A. Cross, Solid-Phase Synthesis And Solid-State N-15 Nmr-Spectroscopy Of Gramicidin-A, Gramicidin-B, And Gramicidin-C, Faseb Journal, 2 (1988) A320-A320.

[40] G.B. Fields, C.G. Fields, J. Petefish, H.E. Vanwart, T.A. Cross, Solid-Phase Peptide-Synthesis And Solid-State Nmr-Spectroscopy Of [Ala3-N-15][Val1]Gramicidin-A, Proceedings Of The National Academy Of Sciences Of The United States Of America, 85 (1988) 1384-1388.

[41] K. *Eichele* and R.E. *Wasylishen. HBA ver. 1.4*; *Dalhousie University, 2001.*

[42] L.M. McDowell, A. Schmidt, E.R. Cohen, D.R. Studelska, J. Schaefer, Structural constraints on the ternary complex of 5-enolpyruvylshikimate-3-phosphate synthase from rotational-echo double-resonance NMR, J. Mol. Biol., 256 (1996) 160-171.

[43] D.R. Studelska, C.A. Klug, D.D. Beusen, L.M. McDowell, J. Schaefer, Long-range distance measurements of protein binding sites by rotational-echo double-resonance NMR, J. Am. Chem. Soc., 118 (1996) 5476-5477.

[44] M.E. Merritt, S.T. Sigurdsson, G.P. Drobny, Long-range distance measurements to the phosphodiester backbone of solid nucleic acids using P-31-F-19 REDOR NMR, J. Am. Chem. Soc., 121 (1999) 6070-6071.

[45] G.L. Olsen, E.A. Louie, G.P. Drobny, S.T. Sigurdsson, Determination of DNA minor groove width in distamycin-DNA complexes by solid-state NMR, Nucleic Acids Res., 31 (2003) 5084-5089.

[46] W.S. Enochs, W.B. Hyslop, H.F. Bennett, R.D. Brown, S.H. Koenig, H.M. Swartz, Sources Of The Increased Longitudinal Relaxation Rates Observed In Melanotic Melanoma - An Invitro Study Of Synthetic Melanins, Investigative Radiology, 24 (1989) 794-804.

[47] H.M. Berman, Westbrook, J., Feng, Z., Gilliland, G., Bhat, T. N., Weissig, H., Shindyalov, I. N., Bourne, P. E., The Protein Data Bank, Nucleic Acids Research, 28 (2000) 235-242.

[48] O.V. Grineva and P.M. Zorkii, Isostructural and nonisostructural compounds in series of halogenated organic crystal substances. Structure of Hal-aggregates, Journal Of Structural Chemistry, 42 (2001) 16-23.

[49] O.V. Grineva and P.M. Zorkii, Aggregation of halogen atoms in crystalline isomers, Journal Of Structural Chemistry, 43 (2002) 995-1005.

[50] O.V. Grineva and P.M. Zorkii, Aggregation of halogen atoms in haloorganic crystals with low halogen contents, Russian Journal Of Physical Chemistry, 74 (2000) 1758-1764.

[51] W.R. Veatch and E.R. Blout, Aggregation Of Gramicidin-A In Solution, Biochemistry, 13 (1974) 5257-5264.

[52] J.A. Killian, K.U. Prasad, D. Hains, D.W. Urry, The Membrane As An Environment Of Minimal Interconversion - A Circular-Dichroism Study On The Solvent Dependence Of The Conformational Behavior Of Gramicidin In Diacylphosphatidylcholine Model Membranes, Biochemistry, 27 (1988) 4848-4855.

[53] B.A. Wallace and K. Ravikumar, The Gramicidin Pore - Crystal-Structure Of A Cesium Complex, Science, 241 (1988) 182-187.

[54] S.M. Pascal and T.A. Cross, High-Resolution Structure And Dynamic Implications For A Double-Helical Gramicidin-A Conformer, Journal Of Biomolecular Nmr, 3 (1993) 495-513.

[55] Z.L. Zhang, S.M. Pascal, T.A. Cross, A Conformational Rearrangement In Gramicidin-A - From A Double-Stranded Left-Handed To A Single-Stranded Right-Handed Helix, Biochemistry, 31 (1992) 8822-8828.

[56] S.M. Pascal and T.A. Cross, Structure Of An Isolated Gramicidin-A Double Helical Species By High-Resolution Nuclear-Magnetic-Resonance, Journal Of Molecular Biology, 226 (1992) 1101-1109.

[57] Y. Chen, A. Tucker, B.A. Wallace, Solution structure of a parallel left-handed double-helical gramicidin-A determined by 2D H-1 NMR, Journal Of Molecular Biology, 264 (1996) 757-769.

[58] A.W. Hing and J. Schaefer, 2-Dimensional Rotational-Echo Double-Resonance Of Val1-[1-C-13]Gly2-[N-15]Ala3-Gramicidin-A In Multilamellar Dimyristoylphosphatidylcholine Dispersions, Biochemistry, 32 (1993) 7593-7604.

[59] T.A. Cross, Solid-State Nuclear-Magnetic-Resonance Approach For Determining The Structure Of Gramicidin A Without Model-Fitting, Biophysical Journal, 49 (1986) 124-126.

[60] L.K. Nicholson, F. Moll, T.E. Mixon, P.V. Lograsso, J.C. Lay, T.A. Cross, Solid-State N-15 Nmr Of Oriented Lipid Bilayer Bound Gramicidin A', Biochemistry, 26 (1987) 6621-6626.

[61] F. Moll, L.K. Nicholson, P.V. Lograsso, J.C. Lay, C.A. Guy, J. Petefish, G.B. Fields, H.E. Vanwart, T.A. Cross, Solid-State N-15 Nmr-Studies Of Uniform And Specific Site N-15 Labeled Gramicidin-A' In An Oriented Lipid Bilayer, Biophysical Journal, 51 (1987) A73-A73.

[62] J.A. Killian, L.K. Nicholson, T.A. Cross, Solid-State N-15-Nmr Evidence That Gramicidin-A Can Adopt 2 Different Backbone Conformations In Dimyristoylphosphatidylcholine Model Membrane Preparations, Biochimica Et Biophysica Acta, 943 (1988) 535-540.

[63] Q. Teng, S.M. Pascal, T.A. Cross, Determination Of Torsion Angles In The Backbone Of The Gramicidin Cation Channel By Solid-State Nmr, Biophysical Journal, 57 (1990) A100-A100.

[64] S.W. Chiu, L.K. Nicholson, M.T. Brenneman, S. Subramaniam, Q. Teng, C. North, J.A. McCammon, T.A. Cross, E. Jakobsson, Molecular-Dynamics Computations And Solid-State Nmr Of The Gramicidin Cation Channel, Biophysical Journal, 57 (1990) A101-A101.

[65] R.R. Ketchem, W. Hu, T.A. Cross, Structural Details Of The Gramicidin Channel Conformation By Solid-State Nmr, Faseb Journal, 6 (1992) A526-A526.

[66] R.R. Ketchem, W. Hu, T.A. Cross, High-Resolution Conformation Of Gramicidin-A In A Lipid Bilayer By Solid-State Nmr, Science, 261 (1993) 1457-1460.

[67] S.L. Grage, J.F. Wang, T.A. Cross, A.S. Ulrich, Solid-state F-19-NMR analysis of F-19-labeled tryptophan in gramicidin A in oriented membranes, Biophysical Journal, 83 (2002) 3336-3350.

[68] G.J. Gallagher, M. Hong, L.K. Thompson, Solid-state NMR spin diffusion for measurement of membrane-bound peptide structure: Gramicidin A, Biochemistry, 43 (2004) 7899-7906.

[69] W.R. Veatch, E.T. Fossel, E.R. Blout, Conformation Of Gramicidin-A, Biochemistry, 13 (1974) 5249-5256.

[70] D.W. Urry, D.F. Mayers, J.D. Glickson, J. Haider, Spectroscopic Studies On Conformation Of Gramicidin-A' - Evidence For A New Helical Conformation, Biochemistry, 11 (1972) 487-&.

[71] J.D. Glickson, D.F. Mayers, D.W. Urry, J.M. Settine, Spectroscopic Studies On Conformation Of Gramicidin A' - Proton Magnetic-Resonance Assignments, Coupling-Constants, And H-D Exchange, Biochemistry, 11 (1972) 477-&.

[72] V.F. Bystrov, A.S. Arseniev, I.L. Barsukov, A.P. Golovanov, I.V. Maslennikov, The Structure Of The Transmembrane Channel Of Gramicidin A - Nmr-Study Of Its Conformational Stability And Interaction With Divalent-Cations, Gazzetta Chimica Italiana, 120 (1990) 485-491.

[73] W.F. Degrado and J.D. Lear, Induction Of Peptide Conformation At Apolar Water Interfaces.1. A Study With Model Peptides Of Defined Hydrophobic Periodicity, Journal Of The American Chemical Society, 107 (1985) 7684-7689.

[74] R.R. Ketchem, K.C. Lee, S. Huo, T.A. Cross, Macromolecular structural elucidation with solid-state NMR-derived orientational constraints, Journal Of Biomolecular Nmr, 8 (1996) 1-14.

[75] B.M. Burkhart, N. Li, D.A. Langs, W.A. Pangborn, W.L. Duax, The conducting form of gramicidin A is a right handed double-stranded double helix, Proceedings Of The National Academy Of Sciences Of The United States Of America, 95 (1998) 12950-12955.

[76] R.R. Ketchem, B. Roux, T.A. Cross, High-resolution polypeptide structure in a lamellar phase lipid environment from solid state NMR derived orientational constraints, Structure, 5 (1997) 1655-1669.

Appendix A: Determination of DNA minor grove width on distamycin-DNA complexes by solid state NMR

5084–5089 Nucleic Acids Research, 2003, Vol. 31, No. 17
DOI: 10.1093/nar/gkg720

Determination of DNA minor groove width in distamycin-DNA complexes by solid-state NMR

Greg L. Olsen, Elizabeth A. Louie, Gary P. Drobny and Snorri Th. Sigurdsson*

Department of Chemistry, University of Washington, Seattle, WA 98195-1700, USA

Received May 12, 2003; Revised and Accepted July 16, 2003

ABSTRACT

We have performed solid-state ^{31}P-^{19}F REDOR nuclear magnetic resonance (NMR) experiments to monitor changes in minor groove width of the oligonucleotide d(CGCAAA$^{2'F}$UTGGC)·d(GCCAAT(pS)TTGCG) (A_3T_2) upon binding of the drug distamycin A at different stoichiometries. In the hydrated solid-state sample, the minor groove width for the unbound DNA, measured as the $^{2'F}$U7–pS19 inter-label distance, was 9.4 ± 0.7 Å, comparable to that found for similar A:T-rich DNAs. Binding of a single drug molecule is observed to cause a 2.4 Å decrease in groove width. Subsequent addition of a second drug molecule results in a larger conformational change, expanding this minor groove width to 13.6 Å, consistent with the results of a previous solution NMR study of the 2:1 complex. These ^{31}P-^{19}F REDOR results demonstrate the ability of solid-state NMR to measure distances of 7–14 Å in DNA–drug complexes and provide the first example of a direct spectroscopic measurement of minor groove width in nucleic acids.

INTRODUCTION

The interactions of proteins and small molecules with nucleic acids have long been a subject of extensive study. In light of the biological importance of nucleic acid complexes, a wide array of biochemical, biophysical and spectroscopic techniques have been used to pursue an atomic level understanding of recognition, binding specificity and structural alterations associated with complex formation. Solid-state NMR can provide important structural and dynamic information about biomolecules and biomolecular complexes, including many systems which are not tractable to X-ray crystallographic or solution NMR analysis (1–6). In particular, when the distances to be measured exceed those observable via solution NMR or when suitable crystals cannot be obtained for X-ray studies, solid-state NMR experiments in conjunction with site-specific isotopic labeling can often allow access to otherwise difficult to obtain inter-atomic distance information. During the past decade, the rotational echo double resonance (REDOR) experiment (7,8) has emerged as the primary solid-state NMR technique for determination of selected heteronuclear dipolar coupling values and has thus become a valuable method for internuclear distance measurement in structural studies of biological systems (reviewed in 8–10).

A particularly important type of DNA–ligand interaction is that of small molecules with the minor groove. Distamycin A is a short naturally occurring peptide antibiotic (Fig. 1), which has been shown to bind non-covalently in the minor groove of A:T-rich B-DNA tracts (11). As distamycin–DNA complexes have been extensively characterized (11–20), they provide useful model systems for solid-state NMR structural studies of nucleic acid complexes. We have performed REDOR experiments to monitor changes in minor groove width in the oligonucleotide d(CGCAAA$^{2'F}$ UTGGC)·d(GCCAAT(pS)-TTGCG) (A_3T_2) upon binding of the drug distamycin at 0:1, 1:1 and 2:1 drug:DNA ratios. Binding of distamycin to A_3T_2 occurs either in the form of a 1:1 complex or as a 2:1 complex: the minor groove can accommodate not only a single distamycin molecule, but also side-by-side antiparallel binding of two distamycin molecules (15,16). It may thus be inferred that distamycin binding at the different ratios must be accompanied by significant deformations of the A_3T_2 minor groove. The present REDOR measurements confirm this, showing a 2 Å decrease in minor groove width upon 1:1 binding and a subsequent 6 Å increase upon formation of the 2:1 complex. These experiments are, to our knowledge, the first example of the use of a spectroscopic technique for direct measurement of groove width in DNA.

MATERIALS AND METHODS

Sample preparation

DNA oligomers d(CGCAAA$^{2'F}$UTGGC) and d(GCCAAT-(pS)TTGCG) were synthesized on an ABI 394 DNA/RNA synthesizer, deprotected in NH_4OH at 55°C for 16 h, then HPLC purified on a C18 column. Following detritylation (4:1 AcOH/H_2O v/v, 40 min, room temperature) and evaporation of the solvent, the oligonucleotides were ethanol precipitated, desalted using Sep-Paks or RP-HPLC, filtered (0.40 µm Alltech nylon) and characterized using analytical denaturing PAGE and electrospray mass spectroscopy. Alternatively, the oligonucleotides were gel purified following detritylation. The purified oligos were dissolved in water and salted by addition of 0.01 M Na_2EDTA and 1.71 M NaCl (final composition 10% Na_2EDTA and 10% NaCl by weight upon lyophilization). Annealing of the DNAs was accomplished by heating this solution to 80°C for 7 min, then cooling to room temperature.

*To whom correspondence should be addressed. Tel: +1 206 616 8276; Fax: +1 206 685 8665; Email: sigurdsson@chem.washington.edu

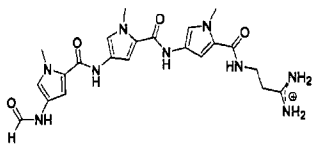

Figure 1. Chemical structure of the minor groove binder distamycin.

The sample was lyophilized and duplex formation verified by non-denaturing PAGE.

The unbound (0:1) DNA sample was run as a frozen solution. A 5.11 μmol aliquot of the lyophilized, salted duplex DNA was dissolved in 50 μl of H_2O, then placed in the MAS rotor.

Distamycin A hydrochloride (Sigma) was used without further purification. The 1:1 drug:DNA sample was prepared by dissolving 1.833 μmol of the salted unbound DNA in H_2O (1.0 ml), adding 514 μl (1.835 μmol) of a freshly prepared 3.57 mM solution of distamycin HCl dissolved in 50 mM sodium cacodylate (pH 6.0), then equilibrating overnight at room temperature. The sample was frozen using liquid nitrogen, lyophilized, returned to the MAS rotor and hydrated by vapor diffusion to 23 waters per nucleotide ($W = 23$). W values were determined gravimetrically following equilibration in a sealed 85% relative humidity chamber. To verify that sample loss or evaporation were not occurring, sample weight was monitored throughout the course of the experiments. The 2:1 complex was formed by redissolving the 1:1 sample in H_2O (0.5 ml), adding 514 μl of a freshly prepared 3.57 mM solution of distamycin HCl dissolved in H_2O (1.835 μmol), then shaking gently overnight at room temperature. The sample was frozen using liquid nitrogen, lyophilized, returned to the MAS rotor and hydrated to $W = 13$.

As three different species, the unbound DNA, DNA in 1:1 complexes and DNA in 2:1 complexes, are expected to be present in the 1:1 sample, simulation of REDOR dephasing for this sample requires determination of their relative populations. If the 9:1 ratio of 1:1 to 2:1 complexes observed in a 0.75:1 drug:DNA mixture (15) is assumed to persist after addition of the additional 0.25 equivalents of drug needed to reach the 1:1 stoichiometry, the relative populations may be estimated as follows: (fraction of DNA in 1:1 complexes) + 2 × (fraction of DNA in 2:1 complexes) = total distamycin equivalents = 1.0, and (fraction 1:1)/(fraction 2:1) = 9/1. Thus (fraction 1:1) = 9 × (fraction 2:1), and 1.0 = 9 × (fraction 2:1) + 2 × (fraction 2:1) = 11 × (fraction 2:1) or (fraction 2:1) = 1.0/11 = 0.0909 ≈ 9%, leaving (fraction 1:1) = 9 × (fraction 2:1) = 0.8181 ≈ 82%, with the remaining 9% of the DNA unbound.

NMR spectroscopy

All experiments were performed in a home built spectrometer with a 4.7 T field (200 MHz proton Larmor frequency), using a home built triply tuned HFP MAS probe (21). All measurements were made at −30°C, with magic angle spinning at 5988 ± 2 Hz. Sample cooling used controlled temperature dry air, generated using an FTS Systems TC-84 controller and XRII851A cooling unit and applied directly to the MAS rotor. rf field strengths were regulated to within ±1%, spinning speed to within ±2 Hz and sample temperatures to within ±1°C. All REDOR experiments employed XY-8 phase cycling on both the ^{31}P and the ^{19}F channels. Custom made 4 mm zirconia rotor barrels were purchased from O'Keeffe Ceramics. Rotor tips and end caps were prepared in-house.

Unbound DNA (0:1) sample. Proton pulse- and cross-polarization rf fields were 50 kHz (5.0 μs T_{90}), with 102 kHz proton decoupling. Phosphorus and fluorine rf pulse fields were 50 and 71 kHz (10.0 and 7.0 μs T_{180}s, respectively). CP contact time was 1.2 ms. 1024 points were acquired, with a dwell time of 25 μs. Nine REDOR S and S_0 data point pairs were acquired, at 1.33 ms (8 rotor period, 1 REDOR cycle) intervals. Acquisition time was 25.6 ms and recycle delay was 2 s. 6174 scans were recorded for each REDOR S or S_0 data point. Four data sets were collected (63 h each) and summed.

(1:1) sample. Proton pulse- and cross-polarization rf fields were 55 kHz (4.5 μs T_{90}), with 114 kHz proton decoupling. Phosphorus and fluorine rf pulse fields were 50 and 67 kHz (10.2 and 7.4 μs T_{180}, respectively). CP contact time was 2.0 ms. 1024 points were acquired, with a dwell time of 25 μs. Acquisition time was 25.6 ms and recycle delay was 2 s. Six REDOR S and S_0 data point pairs were acquired, at 1.33 ms (8 rotor period, one REDOR cycle) intervals. (Due to rapid dephasing, this experiment was adjusted to collect S and S_0 points at the shorter intervals.) 4096 scans were recorded for each REDOR S or S_0 data point. Six data sets were collected (28 h each), then summed.

(2:1) sample. Proton pulse- and cross-polarization rf fields were 52 kHz (4.8 μs T_{90}), with 107 kHz proton decoupling. Phosphorus and fluorine rf pulse frequencies were 50 and 63 kHz (10.2 and 7.9 μs T_{180}, respectively). CP contact time was 1.75 ms. 256 points were acquired, with a dwell time of 25 μs. Recycle delay was 3 s. Acquisition time was 6.4 ms. The shortened acquisition time for the 2:1 sample was used to allow application of a higher decoupling field while avoiding rf arcing.

An initial experiment showed minimal dephasing for the 2:1 sample, indicating that the P-F distance to be measured in this sample was significantly longer than for either of the two previous samples. To determine long (>10 Å) P-F distances, longer dephasing times are required. The associated reduction in signal to noise, however, necessitates significantly extended signal averaging times, and instrumental stability and time requirements then prohibit acquisition of a full dephasing curve. In such cases, acquisition of a single REDOR point may be used to obtain the internuclear separation (3). Hence, to enable measurement of the longer distance, a single dephasing time, 14.7 ms (11 REDOR cycles), was selected for application during a single shorter (6 day) signal averaging period. Data were acquired in 14 h (8192 scan) blocks, which were individually screened for arcing, then summed prior to processing.

Data processing

Data processing was performed using the Gullringen NMR processing suite (Gullringen: a computer program for

5086 Nucleic Acids Research, 2003, Vol. 31, No. 17

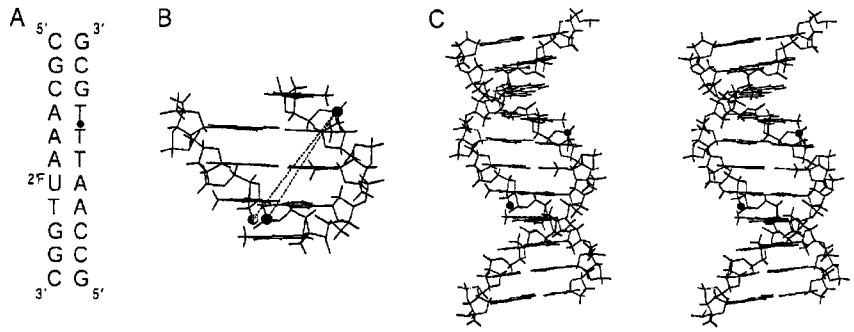

Figure 2. (A) The A_3T_2 DNA sequence used in this study. ^{2F}U indicates 2′-fluoro-2′-deoxyuridine and the dot between T18 and T19 denotes a phosphorothioate. (B) Expanded view of A_3T_2 DNA showing label positions corresponding to standard and P-F REDOR measures of minor groove width across the central A_3T_2 tract. The dark sphere at upper right marks the *i* phosphate (T19); on the lower left, the dark sphere indicates the *i* + 3 phosphate (T8), while the light sphere indicates the 2′F label used in the present experiments. The standard B-form DNA model for the A_3T_2 oligomer was generated using the biopolymer module of Insight II (Biosym). (C) Stereoview of the free A_3T_2 DNA generated using Insight II. Dark spheres show location of phosphorothioate and ^{2F}U.

estimation of molecular properties from NMR experiments, T. Karlsson and G.P. Drobny, in preparation). All simulations were performed using Simpson (22). Reduced χ^2 plots were used to determine best fit distances and error bounds (90% confidence intervals).

RESULTS AND DISCUSSION

Measurement of DNA groove width

Direct measurement of minor groove width in DNA presents a spectroscopic challenge, as the distances to be measured exceed the range of NOE residual dipolar coupling measurements. For instance, upon widening of the minor groove to accommodate drug binding, the groove width will often exceed 10 Å (15,16,23–26). While such distances are currently beyond the reach of solution NMR methods, ^{31}P-^{19}F REDOR has been used to determine internuclear distances of up to 16 Å, making it an ideal tool for the task (3,27). In the REDOR experiment, measurement of heteronuclear dipolar couplings is accomplished using 'dephasing' pulses during magic angle sample spinning to disrupt the averaging of the dipolar coupling. Application of these pulses to nuclei that are coupled to the observed spins produces an attenuated signal, which is then compared to a reference signal from a control experiment in which the dephasing pulses were omitted. Plotting the ratio of the experimental (S) and reference (S_o) signals versus evolution (dephasing) time, S/S_o, allows extraction of the dipolar coupling constant, thus giving direct access to the internuclear distance. In particular, the observed decay in S/S_o is dependent upon the number of rotor cycles (i.e. the dipolar evolution time) and on the dipolar coupling constant. Fitting of each observed REDOR dephasing curve to a simulation then allows determination of internuclear distances.

A common measure of minor groove width is the distance between a selected backbone phosphate *i* and the *i* + 3 phosphate on the opposing strand (28–32). To adapt this for observation of A_3T_2 via REDOR, the ^{31}P-^{19}F distance was measured between phosphate T19 (*i* position) in the backbone and a 2′-fluoro-labeled uridine substituted at T7 directly across the groove (immediately 3′ of the *i* + 3 phosphate) (Fig. 2). As can be seen in Figure 2, the two schemes represent quite similar measures of groove width. Since backbone phosphates have nearly the same chemical shift in solid-state NMR, replacement of the selected phosphate by a phosphorothioate was used to shift the corresponding phosphate resonance, resolving it from the large DNA phosphodiester backbone peak, thereby eliminating the need for phosphorus background correction (27). As the phosphoramidite of 2′-fluorouridine is commercially available, allowing easy insertion of a high sensitivity (high γ) heterospin for the REDOR measurements, and because incorporation of phosphorothioates is readily accomplished during DNA synthesis, this ^{31}P-^{19}F labeling scheme allows rapid and inexpensive sample preparation, avoiding synthetic difficulties often associated with isotopic labeling in nucleic acids.

Distamycin is a minor groove binder

Double-helical DNA, in particular the B-form, is known to display sequence-dependent conformational variation (33,34). A:T-rich B-DNA tracts, for example, are observed to form an unusually narrow minor groove (13,28,33,35), which has been shown to be the preferred binding site for a number of small minor groove binding compounds (11). One of these, distamycin (Fig. 1), is a short peptide antibiotic containing three pyrrole rings and a positively charged propylamidinium tail. Distamycin binds non-covalently in the minor groove of several A:T-rich sequences, using a combination of electrostatic, van der Waals and hydrogen bonding interactions

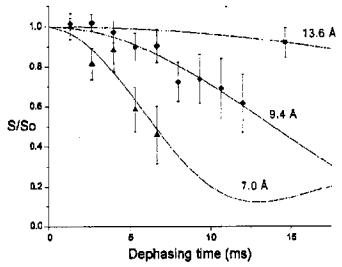

Figure 3. REDOR dephasing curves for A_3T_2 DNA and its 1:1 and 2:1 distamycin complexes. Solid lines represent expected decay curves based on simulations. Diamonds mark data for the unbound A_3T_2 DNA, triangles for the 1:1 distamycin:A_3T_2 complex and the square for the 2:1 distamycin:A_3T_2 complex. The lowest (7.0 Å) line represents a simulation for the 1:1 sample, where the fit is a weighted superposition of simulated dephasing curves corresponding to the three species present in the sample (unbound A_3T_2 and the 1:1 and 2:1 complexes), as described in the text.

(11,13–16,18,19,36). Solution NMR models place the distamycin amide protons in positions to hydrogen bond to acceptors on the floor of the minor groove and situate the drug pyrrole rings in close van der Waals contact to the walls of the groove (14–16). The cationic propylamidinium group of the drug contributes to electrostatic interactions between distamycin and the negative potential of the phosphate backbone (15,16). When bound, distamycin assumes an extended conformation, forming a crescent shape spanning 5 bp and conforming to the curvature of the minor groove. Solution NMR experiments on distamycin in complex with the 11mer used for the present experiments (Fig. 1) found that for this sequence, distamycin binds at the central A_3T_2 site as a monomer and side-by-side as an antiparallel dimer, to form both 1:1 and 2:1 complexes, respectively (15,16). Accordingly, to probe perturbations of the groove associated with formation of these complexes, we have measured the A_3T_2 minor groove width in samples at 0:1, 1:1 and 2:1 distamycin:DNA stoichiometries.

^{31}P-^{19}F REDOR solid-state NMR measurements

Groove width in unbound DNA. The initial REDOR experiment, performed on A_3T_2 prior to addition of distamycin, was used to obtain the native groove width corresponding to our P-F label pair in the solid-state sample. The REDOR data for the unbound DNA are shown in Figure 3, where S/S_o is plotted versus dephasing time. Comparison of the experimental results to simulated dephasing curves gives a χ^2 best fit groove width of 9.4 ± 0.7 Å. While neither X-ray crystal nor solution NMR structures are available for this DNA, structures for a collection of similar A:T-rich DNA sequences show corresponding (pS-^{19}F) inter-label distances of 9.6–10.9 Å, which are in agreement with the present REDOR measurement (37–41).

Groove width in distamycin–DNA 1:1 complex. Following addition of one equivalent of the drug, the second REDOR experiment was performed. Figure 3 shows the resulting dephasing curve obtained for the 1:1 sample. The observed rapid dephasing suggests a significant narrowing of the minor groove. One complicating factor in the determination of groove width from these data is the expected presence of several different species in the 1:1 sample. Solution NMR results for titration of distamycin with A_3T_2 indicate that three DNA species, the unbound DNA, the 1:1 complex and the 2:1 complex, should be present following addition of a single equivalent of the drug (15,16). A qualitative fit to the 1:1 sample data was obtained using the following two assumptions. First, the 9:1 ratio of 1:1 to 2:1 complexes observed in a 0.75:1 drug:DNA mixture (15) was assumed to persist after addition of the additional 0.25 equivalents of drug needed to reach the 1:1 stoichiometry. This assumption results in three approximate populations for the DNA within the 1:1 sample: ~82% bound in 1:1 drug:DNA complexes, ~9% in 2:1 complexes, with the remaining ~9% present as the unbound DNA (see Materials and Methods for calculation details). Second, the minor groove widths for the 0:1 and 2:1 samples were taken to be those measured in the present REDOR experiments, 9.4 and 13.6 Å, respectively. The REDOR dephasing curve is a superposition of curves corresponding to each of the three species present in the sample, weighted according to relative population. A single parameter, the minor groove width corresponding to the 1:1 complexes, was varied, with the remaining distances and populations fixed as described above. This fitting procedure yields a ^{31}P-^{19}F distance of ~7.0 Å, a decrease of 2.4 Å relative to the corresponding distance in the unbound DNA.

Binding of one distamycin molecule thus appears to produce a significant narrowing of the DNA minor groove in the hydrated solid state. Decreases in minor groove width upon distamycin binding have previously been observed. For example, the analogous distance across the central AAT tract in the dodecamer d(CGCAAATTTGCG)$_2$ was found to decrease by ~0.7 Å in an X-ray structure of the 1:1 distamycin complex (13), relative to the unbound DNA (42).

Recent solution NMR studies and molecular dynamics simulations have shown a strong response of minor groove width to the local electrostatic environment, suggesting that electrostatic disturbances associated with distamycin occupancy of the minor groove could significantly affect the groove width (32,43–47). Hence, one possibility consistent with the present results is that upon distamycin binding, displacement of the minor groove spine of hydration or of counterions in the hydration shells provides such a perturbation of the electrostatic environment within the minor groove. Alternatively, enhancement of van der Waals contact between distamycin and the groove walls could be a driving force for a narrowed minor groove (11,13–16,31).

Groove width in distamycin–DNA 2:1 complex. Upon addition of a second equivalent of distamycin, solution NMR studies reveal that only those solution NMR cross-peaks corresponding to a 2:1 complex are present (15,16). The REDOR dephasing data for the 2:1 complex is shown in Figure 3, and Figure 4 shows the corresponding S and S_o spectra. In contrast to the 1:1 complex, a significant increase in minor groove width, to 13.6 ± 1.5 Å, was observed for the 2:1 complex. The 2:1 groove width observed in the present experiment is in

5088 Nucleic Acids Research, 2003, Vol. 31, No. 17

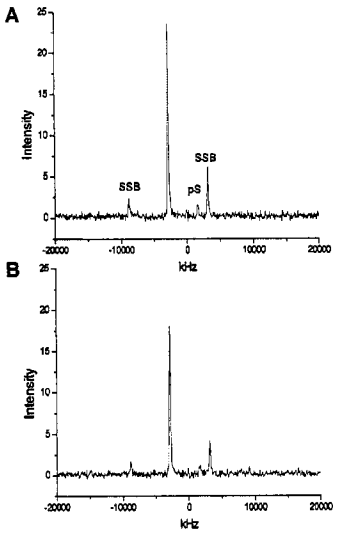

Figure 4. REDOR S and S_0 spectra for the 2:1 distamycin:A_3T_2 DNA complex. Plots were generated without line broadening and show absolute intensities. (A) Reference (S_0) ^{31}P spectrum, where pS denotes the phosphorothioate signal. The large central peak and its spinning side bands (SSB) are due to unmodified backbone phosphates. (B) Experimental (S) REDOR spectrum, showing diminished ^{31}P backbone and phosphorothioate peak intensities following application of ^{19}F pulses.

agreement with the distance seen in a model generated using solution NMR distance restraints (~13.1 Å; D. Wemmer, personal communication).

CONCLUSION

In summary, these results show large changes in DNA minor groove width as ligand stoichiometry is varied (Fig. 4). In the hydrated solid-state sample, binding of a single distamycin molecule to A_3T_2 generates a 2.4 Å decrease in groove width, while addition of a second drug molecule results in a large conformational change, expanding the minor groove width by 6.6 Å, to 13.6 Å. The 13 Å distance suggested by a previous solution NMR study for the 2:1 complex is supported by our data, demonstrating the ability of ^{31}P-^{19}F REDOR to accurately measure distances of >10 Å in a nucleic acid complex. These solid-state NMR studies present, to our knowledge, the first example of direct spectroscopic measurement of minor groove width in nucleic acids.

ACKNOWLEDGEMENTS

We thank J. Markley for synthesis and purification of the DNA samples, D. Wemmer for use of the 2:1 distamycin–DNA model coordinate file and the Drobny and Sigurdsson groups for critical review of the manuscript. This work was supported by a grant from the National Institutes of Health (GM58914).

REFERENCES

1. Ketchem,R.R., Hu,W. and Cross,T.A. (1993) High-resolution conformation of gramicidin A in a lipid bilayer by solid-state NMR. *Science*, **261**, 1457–1460.
2. Opella,S.J., Kim,Y. and Mcdonnell,P. (1994) Experimental nuclear magnetic resonance studies of membrane proteins. *Methods Enzymol.*, **239**, 536–560.
3. Studelska,D.R., Klug,C.A., Beusen,D.D., McDowell,L.M. and Schaefer,J. (1996) Long-range distance measurements of protein binding sites by rotational-echo double resonance NMR. *J. Am. Chem. Soc.*, **118**, 5476–5477.
4. Merritt,M.E., Christensen,A.M., Kramer,K., Hopkins,T. and Schaefer,J. (1996) Detection of intercatechol cross-links in insect cuticle by solid-state carbon-13 and nitrogen-15 NMR. *J. Am. Chem. Soc.*, **118**, 11278–11282.
5. Wang,J., Balazs,Y.S. and Thompson,L.K. (1997) Solid-state REDOR NMR distance measurements at the ligand site of a bacterial chemotaxis membrane receptor. *Biochemistry*, **36**, 1699–1703.
6. Long,J.R., Dindot,J.L., Zebroski,H., Kiihne,S., Clark,R.H., Campbell,A.A., Stayton,P.S. and Drobny,G.P. (1998) A peptide that inhibits hydroxyapatite growth is in an extended conformation on the crystal surface. *Proc. Natl Acad. Sci. USA*, **95**, 12083–12087.
7. Gullion,T. and Schaefer,J. (1989) Rotational-echo double-resonance NMR. *J. Magn. Reson.*, **81**, 196–200.
8. Gullion,T. and Schaefer,J. (1989) Detection of weak heteronuclear dipolar coupling by rotational-echo double-resonance nuclear magnetic resonance. *Adv. Magn. Reson.*, **13**, 57–83.
9. Gullion,T. (1997) Measurement of heteronuclear dipolar interactions by rotational-echo, double-resonance nuclear magnetic resonance. *Magn. Reson. Rev.*, **17**, 83–131.
10. Dusold,S. and Sebald,A. (2000) Dipolar recoupling under magic angle spinning conditions. In Webb,G. (ed.), *Annual Reports on NMR Spectroscopy*. Academic Press Inc, San Diego, Vol. 41, pp. 185–264.
11. Zimmer,C. and Wahnert,U. (1986) Nonintercalating DNA-binding ligands: specificity of the interaction and their use as tools in biophysical, biochemical and biological investigations of the genetic material. *Prog. Biophys. Mol. Biol.*, **47**, 31–112.
12. Klevit,R.E., Wemmer,D.E. and Reid,B.R. (1986) 1H NMR studies on the interaction between distamycin A and a symmetrical DNA dodecamer. *Biochemistry*, **25**, 3296–3303.
13. Coll,M., Frederick,C.A., Wang,A.H. and Rich,A. (1987) A bifurcated hydrogen-bonded conformation in the d(a.T) base pairs of the DNA dodecamer d(CGCAAATTTGCG) and its complex with distamycin. *Proc. Natl Acad. Sci. USA*, **84**, 8385–8389.
14. Pelton,J.G. and Wemmer,D.E. (1988) Structural modeling of the distamycin a-d(CGCGAATTCGCG)$_2$ complex using 2D NMR and molecular mechanics. *Biochemistry*, **27**, 8088–8096.
15. Pelton,J.G. and Wemmer,D.E. (1989) Structural characterization of a 2:1 distamycin a.D(CGCAAATTGGC) complex by two-dimensional NMR. *Proc. Natl Acad. Sci. USA*, **86**, 5723–5727.
16. Pelton,J.G. and Wemmer,D.E. (1990) Structure and dynamics of distamycin A with d(CGCAAATTGGC):D(GCCAATTTGCG) at low drug:DNA ratios. *J. Biomol. Struct. Dyn.*, **8**, 81–97.
17. Wang,H., Liaw,Y., Robinson,H. and Gao,Y. (1990) Mutual conformational adaptation of both ligand and receptor in anti-tumor drug-DNA complexes. In Pullman,B. and Jortner,J. (eds), *Molecular Basis of Specificity in Nucleic Acid–Drug Interactions*. Kluwer, Dordrecht, The Netherlands, pp. 1–21.
18. Boehncke,K., Nonella,M., Schulten,K. and Wang,A.H. (1991) Molecular dynamics investigation of the interaction between DNA and distamycin. *Biochemistry*, **30**, 5465–5475.
19. Rentzeperis,D., Kupke,D.W. and Marky,L.A. (1992) Differential hydration of homopurine sequences relative to alternating purine/pyrimidine sequences. *Biopolymers*, **32**, 1065–1075.
20. Fagan,P. and Wemmer,D.E. (1992) Cooperative binding of distamycin-A to DNA in the 2:1 mode. *J. Am. Chem. Soc.*, **114**, 1080–1081.

21. Stringer,J. and Drobny,G.P. (1998) Methods for the analysis and design of a solid state nuclear magnetic resonance probe. *Rev. Sci. Instrum.*, **69**, 3384–3391.
22. Bak,M., Rasmussen,J.T. and Nielsen,N.C. (2000) Simpson: a general simulation program for solid-state NMR spectroscopy. *J. Magn. Reson.*, **147**, 296–330.
23. Pjura,P.E., Grzeskowiak,K. and Dickerson,R.E. (1987) Binding of Hoechst 33258 to the minor groove of B-DNA. *J. Mol. Biol.*, **197**, 257–271.
24. Tabernero,L., Verdaguer,N., Coll.M., Fita,I., Van Der Marel,G.A., Van Boom,J.H., Rich,A. and Aymami,J. (1993) Molecular structure of the A-tract DNA dodecamer d(CGCAAATTTGCG) complexed with the minor groove binding drug netropsin. *Biochemistry*, **32**, 8403–8410.
25. Nunn,C.M. and Neidle,S. (1995) Sequence-dependent drug binding to the minor groove of DNA: crystal structure of the DNA dodecamer $d(CGCAAATTTGCG)_2$ complexed with propamidine. *J. Med. Chem.*, **38**, 2317–2325.
26. Mitra,S.N., Wahl,M.C. and Sundaralingam,M. (1999) Structure of the side-by-side binding of distamycin to $d(GTATATAC)_2$. *Acta Crystallogr. D*, **55**, 602–609.
27. Merritt,M., Sigurdsson,S.T. and Drobny,G.P. (1999) Long-range measurements to the phosphodiester backbone of solid nucleic acids using 31P-19F REDOR NMR. *J. Am. Chem. Soc.*, **121**, 6070–6071.
28. Fratini,A.V., Kopka,M.L., Drew,H.R. and Dickerson,R.E. (1982) Reversible bending and helix geometry in a B-DNA dodecamer: CGCGAATTBrCGCG. *J. Biol. Chem.*, **257**, 14686–14707.
29. Laughton,C. and Luisi,B.F. (1998) The mechanics of minor groove width variation in DNA and its implications for the accomodation of ligands. *J. Mol. Biol.*, **288**, 953–963.
30. Gavathiotis,E., Sharman,G.J. and Searle,M.S. (2000) Sequence-dependent variation in DNA minor groove width dictates orientational preference of Hoechst 33258 in A-tract recognition: solution NMR structure of the 2:1 complex with $d(CTTTTGCAAAAG)_2$. *Nucleic Acids Res.*, **28**, 728–735.
31. Bostock-Smith,C.E., Harris,S.A., Laughton,C.A. and Searle,M.A. (2001) Induced fit DNA recognition by a minor groove binding analogue of Hoechst 33258: fluctuations in DNA A tract structure investigated by NMR and molecular dynamics simulations. *Nucleic Acids Res.*, **29**, 693–702.
32. Wellenzohn,B., Flader,W., Winger,R.H., Hallbrucker,A., Mayer,E. and Liedl,K.R. (2002) Influence of netropsin's charges on the minor groove width of $d(CGCGAATTCGCG)_2$. *Biopolymers*, **61**, 276–286.
33. Saenger,W. (1984) *Principles of Nucleic Acid Structure*. Springer-Verlag, New York, NY, pp. 220–241, 253–282.
34. Dickerson,R.E. (1983) Base sequence and helix structure variation in B and A DNA. *J. Mol. Biol.*, **166**, 419–441.
35. Nelson,H.C., Finch,J.T., Luisi,B.F. and Klug,A. (1987) The structure of an oligo(dA).oligo(dT) tract and its biological implications. *Nature*, **330**, 221–226.
36. Kopka,M.L., Yoon,C., Goodsell,D., Pjura,P. and Dickerson,R.E. (1985) The molecular origin of DNA-drug specificity in netropsin and distamycin. *Proc. Natl Acad. Sci. USA*, **82**, 1376–1380.
37. Kim,S.G. and Reid,B.R. (1992) Solution structure of the T_nA_n DNA duplex GCCGTTAACGCG containing the hpa1 restriction site. *Biochemistry*, **31**, 12103–12116.
38. Arumini,J.M., Mujeeb,A. and Germann,M.W. (1998) NMR solution structures of $[d(GCGAAT\text{-}3'\text{-}3'\text{-}alphaT\text{-}5'\text{-}5'\text{-}CGC)_2]$ and its unmodified control. *Nucleic Acids Res.*, **26**, 5644–5654.
39. Tjandra,N., Tate,S., Ono,A., Kainosho,M. and Bax,A. (2000) The NMR structure of a DNA dodecamer in an aqueous dilute liquid crystalline phase. *J. Am. Chem. Soc.*, **122**, 6190–6200.
40. Kuszewski,J., Schwieters,C. and Clore,G.M. (2001) Improving the accuracy of NMR structures of DNA by means of a database potential of mean force describing base-base positional interactions. *J. Am. Chem. Soc.*, **123**, 3903–3918.
41. Barbic,A., Zimmer,D.P. and Crothers,D.M. (2003) Structural origins of adenine-tract bending. *Proc. Natl Acad. Sci. USA*, **100**, 2369–2373.
42. Edwards,K.J., Brown,D.G., Spink,N., Skelly,J.V. and Neidle,S. (1992) Molecular structure of the B-DNA dodecamer $d(CGCAAATTTGCG)_2$. An examination of propeller twist and minor-groove water structure at 2.2 Å resolution. *J. Mol. Biol.*, **226**, 1161–1173.
43. Hud,N.V. and Feigon,J. (1997) Localization of divalent metal ions in the minor groove of DNA A-tracts. *J. Am. Chem. Soc.*, **119**, 5756–5757.
44. Hud,N.V., Sklenar,V. and Feigon,J. (1999) Localization of ammonium ions in the minor groove of DNA duplexes in solution and the origin of DNA A-tract bending. *J. Mol. Biol.*, **286**, 651–660.
45. Hamelberg,D., McFail-Isom,L., Williams,L.D. and Wilson,W.D. (2000) Flexible structure of DNA: ion dependence of minor-groove structure and dynamics. *J. Am. Chem. Soc.*, **122**, 10513–10520.
46. Shui,X., Sines,C.C., McFail-Isom,L., Vanderveer,D. and Williams,L.D. (1998) Structure of the potassium form of CGCAATTCGCG: DNA deformation by electrostatic collapse around inorganic cations. *Biochemistry*, **37**, 16877–16887.
47. Wellenzohn,B., Flader,W., Winger,R.H., Hallbrucker,A., Mayer,E. and Liedl,K.R. (2001) Significance of ligand tails for interaction with the minor groove of B-DNA. *Biophys. J.*, **81**, 1588–1599.

Appendix B: Solid State NMR Structural Studies of Peptides Immobilized in Gold Nanoparticles

Solid-State NMR Structural Studies of Peptides Immobilized on Gold Nanoparticles

P. V. Bower,[†] E. A. Louie,[†] J. R. Long,[†,‡,§] P. S. Stayton,[§] and G. P. Drobny*[,†]

Department of Chemistry and Department of Bioengineering, University of Washington, Seattle, Washington 98195-1700

Received June 29, 2004

In this paper we describe solid-state NMR experiments that provide information on the structures of surface-immobilized peptides. The peptides are covalently bound to alkanethiolates that are self-assembled as monolayers on colloidal gold nanoparticles. The secondary structure of the immobilized peptides was characterized by quantifying the Ramachandran angles ϕ and ψ. These angles were determined in turn from distances between backbone carbonyl ^{13}C spins, measured with the double-quantum filtered dipolar recoupling with a windowless sequence experiment, and by determination of the mutual orientation of chemical shift anisotropy tensors of ^{13}C carbonyl spins on adjacent peptide planes, obtained from the double-quantum cross-polarization magic-angle spinning spectrum. It was found that peptides composed of periodic sequences of leucines and lysines were bound along the length of the peptide sequence and displayed a tight α-helical secondary structure on the gold nanoparticles. These results are compared to similar studies of peptides immobilized on hydrophobic surfaces.

Introduction

The development of materials with enhanced biocompatibility is a major focus of the materials and tissue engineering communities.[1-4] As a consequence there has been considerable interest in the use of peptide- and protein-based coatings on materials and tissue engineering scaffolds, with the goal of recreating a natural extracellular matrix to direct wound repair or tissue development and homeostasis.[5-9] Many materials currently used in biomedical materials and tissue engineering scaffolds are modified directly with biomolecules, or the biomolecules can be conjugated through a hydrophilic layer [e.g., poly(ethylene oxide)-based].[10-15] In addition to the biomaterials and tissue engineering fields, there is considerable interest in the patterned immobilization of active peptides and proteins, in affinity separations, diagnostics, proteomics, and cell culture technologies. There has been considerable interest in gold-based nanoparticles for bioanalytical applications. A major concern in all these applications is retention of biological specificity (i.e., structure and dynamics) after adsorption or conjugation of the biomolecules.

Numerous studies have shown that peptide-modified surfaces influence cell attachment, shape, and function. For example, peptide coatings composed of the sequence arginine−glycine−aspartate (R-G-D) have been broadly used to promote cell adhesion to materials. A key element in optimizing the "biocompatibility" of peptide coatings is determining and controlling the secondary structure of the immobilized peptide. We have recently reported an approach to modifying hydrophobic materials using synthetic peptides that are designed to assemble with a defined structure and orientation on the surface via the hydrophobic effect.[34] DeGrado and Lear[16] demonstrated that specific secondary structures could be observed in short peptides at the air/water interface by varying the hydrophobic periodicity in the peptides to match the periodicity of the desired secondary structure, so our recent work corresponds to basically the same effect only observed at a biomaterial interface. Interestingly, when used as biomaterial coatings, these peptides reverse the usual paradigm of protein unfolding being driven by hydrophobic surfaces, through the design of a recognition mechanism that stabilizes a specific secondary structure on the surface.

Solid-state nuclear magnetic resonance (SSNMR) has the ability to probe structure and dynamics at specific residues in an immobilized peptide sequence. ^{13}C SSNMR gives favorable signal if $\sim 10^{19}$ spins are present in the sample chamber. For surface-adsorbed molecules this requires high surface area substrates and good coverage because the volume of a typical sample chamber used in SSNMR is ~100 μL. The size of the colloidal particles (diameter 2−200 nm) gives very favorable surface areas

* To whom correspondence should be addressed. E-mail: drobny@macmail.chem.washington.edu.

† Department of Chemistry, University of Washington.

‡ Current address: University of Florida, Department of Biochemistry and Molecular Biology, Gainesville, FL.

§ Department of Bioengineering, University of Washington.

(1) Healy, K. E. *Curr. Opin. Solid State Mater. Sci.* **1999**, *4*, 381−387.

(2) Angelova, N.; Hunkeler, D. *Trends Biotechnol.* **1999**, *17*, 409−421.

(3) Griffith, L. G. *Acta Mater.* **2000**, *48*, 263−277.

(4) Langer, R. *Acc. Chem. Res.* **2000**, *33*, 94−101.

(5) Borkenhagen, M.; Clemence, J. F.; Sigrist, H.; Aebischer, P. J. *Biomed. Mater. Res.* **1998**, *40*, 392−400.

(6) Belcheva, N.; Baldwin, S. P.; Saltzman, W. M. *J. Biomat. Sci., Polymer Ed.* **1998**, *9*, 207−226.

(7) Rezania, A.; Healy, K. E. *Biotechnol. Prog.* **1999**, *15*, 19−32.

(8) Gilbert, M.; Shaw, W. J.; Long, J. R.; Nelson, K.; Drobny, G. P.; Giachelli, C. M.; Stayton, P. S. *J. Biol. Chem.* **2000**, *275*, 16213−16218.

(9) Whang, K.; Goldstick, T. K.; Healy, K. E. *Biomaterials* **2000**, *21*, 2545−2551.

(10) Drumheller, P. D.; Elbert, D. L.; Hubbell, J. A. *Biotechnol. Bioeng.* **1994**, *43*, 772−780.

(11) Walluscheck, K. P.; Steinhoff, G.; Kelm, S.; Haverich, A. *European Journal of Vascular and Endovascular Surgery* **1996**, *12*, 321−330.

(12) Neff, J. A.; Caldwell, K. D.; Tresco, P. A. *J. Biomed. Mater. Res.* **1998**, *40*, 511−519.

(13) Tong, Y. W.; Shoichet, M. S. *J. Biomat. Sci., Polymer Ed.* **1998**, *9*, 713−729.

(14) Pakalns, T.; Haverstick, K. L.; Fields, G. B.; McCarthy, J. B.; Mooradian, D. L.; Tirrell, M. *Biomaterials* **1999**, *20*, 2265−2279.

(15) Bhadriraju, K.; Hansen, L. K. *Biomaterials* **2000**, *21*, 267−272.

(16) DeGrado, W. F.; Lear, J. D. *J. Am. Chem. Soc.* **1985**, *107*, 7684−7689.

10.1021/la040092w CCC: $30.25
Published on Web 00/00/0000 PAGE EST: 6

in the lower diameter range (~20 m² in a NMR rotor), and the addition of a self-assembled monolayer (SAM) composed of alkanethiolates enables the immobilization of biomolecules by a number of mechanisms depending upon the terminal functional group of the SAM.

The synthetic preparation of colloidal gold has been extended to include self-protection of the gold cluster by SAMs of functionalized alkanethiols and other sulfur-containing capping molecules[1] into what are commonly called monolayer-protected clusters (MPCs). Gold coatings are easily constructed on many underlying materials, and the coverage with a SAM provides a versatile interface for subsequent masking of the material with the peptide coatings. Following the results of our recent SSNMR study of the structures of peptides with varying periodicities of leucine and lysine residues adsorbed on polystyrene beads, we synthesized and used in the present study a peptide displaying a periodic alternation of leucine and lysine amino acids: Ac-LKKLLKLLKKLLKL-NH_2 (LKα14). This peptide was shown in our earlier study to assume a helical structure when adsorbed onto polystyrene beads. In the present study LKα14 was synthesized, adsorbed, and covalently tethered to gold nanoparticles coated with an alkanethiolate SAM and studied using a combination of SSNMR techniques. Using conventional SSNMR experiments and newly developed double-quantum techniques, their helical structure was verified. Large-amplitude dynamics on the NMR time scale were not observed, further substantiating the conjugation of the peptides to the SAM-coated particles. Two-dimensional double-quantum experiments using ^{13}C enriched peptide sequences allow high-resolution determination of secondary structure in heterogeneous environments where the peptides are a minor component of the material. These results shed light on how gold nanoparticle surfaces may be surface-modified by structured peptides and demonstrate the level of molecular structural and dynamic information SSNMR can provide from biomaterial composites.

Materials and Methods

Peptide Synthesis and Characterization. Carbonyl ^{13}C-labeled leucine and ^{15}N-labeled lysine were purchased from Cambridge Isotope Laboratories (Andover, MA) and protected using standard protocols. Peptides were synthesized by United Biochemical Research, Inc. (Seattle, WA), on an automated synthesizer using MBHA resin, and protected, isotopically labeled amino acids were provided by the authors. The peptides were cleaved from the resin using 95% trifluoroacetic acid with 2.5% triisopropylsilane and 2.5% water. The crude peptides were purified using a Waters HPLC C-18 reverse phase column with a water/acetonitrile solvent system containing 0.1% trifluoroacetic acid. Peptide fractions were lyophilized and analyzed by electrospray mass spectrometry to establish isotope incorporation and peptide purity.

Selectively ^{13}C labeled Ac-LKKLLKLLKKLLKL (LKα14) was produced in several versions for SSNMR studies. In the first sample, carbonyl-labeled leucine (i.e., leucine-1-^{13}C) was incorporated at positions L4 and L5. In a second sample, leucine-1-^{13}C was incorporated at positions L11 and L12. These samples were used to determine backbone torsion angles in LKα14 covalently immobilized on MPC-coated gold nanoparticles. To monitor lysine side-chain dynamics, lysine-ε-^{15}N was incorporated at K10.

MPC Synthesis. To enable covalent attachment of LKα14, a water-soluble, functionalized MPC gold bead is required. MPCs consisting of ω-carboxylic acid functionalized alkanethiolates can be made water-soluble by minimizing the length of the methylene spacer chain and by introducing polar functional groups between the thiol group and the ω-carboxyl group. An approach developed by Murray et al.[17] for the preparation of water-soluble MPC gold particles utilizes thiol-containing biomolecules such as tiopronin (*N*-2-mercaptopropionylglycine, see Figure 1), a drug used in the treatment of cystinuria and arthritis. To prepare tiopronin-based MPCs, 0.31 g of $HAuCl_4$ (0.80 mmol) and 0.38 g (2.4 mmol) of *N*-(2-mercaptopropionyl)glycine (i.e., tiopronin) were dissolved in a 6:1 methanol/acetic acid (30 mL/5 mL) solution, yielding a deep ruby-red solution. To this solution was added with rapid stirring 0.6 g of $NaBH_4$ (16 mmol) in 15 mL of H_2O, and the resulting solution turned from ruby red to black. Following the addition of $NaBH_4$ the solution temperature rose from room temperature (ca. 25 °C) to over 40 °C. After stirring for 45 min, the solvent was removed under a vacuum. A total of 150 mg of product was dissolved in 75 mL of H_2O, the pH was adjusted to 1 by dropwise addition of concentrated HCl, and the resulting solution was loaded into dialysis membrane (molecular weight cutoff 10 000) and placed in 4 L of nanopure H_2O. The solution, dialyzed for a total time of 72 h, was recharged with fresh H_2O about once every 10 h. The dark blue tiopronin–MPC solution was collected, and the solvent was removed under a vacuum (temp <40 °C). Under the conditions described above, gold nanoparticles with a 1–3-nm diameter were produced with about 85 chains attached per particle.[17]

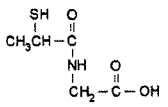

Figure 1. Tiopronin (*N*-2-mercaptopropionylglycine).

Attachment of Peptides to Protected Gold Nanoparticles. LKα14 was covalently attached to the MPC through the creation of amide bonds between the primary amine groups of the lysine side chains and the terminal carboxyl groups of the tiopronin–MPC. This was done by reacting the terminal carboxyl groups of the tiopronin–MPC with 1-ethyl-3-(3-dimethylaminopropyl)carbodiimide HCl (EDC) to form an *o*-acylisourea-active intermediate, followed by reaction with *N*-hydroxysulfosuccinimide (sulfo-NHS) to form a sulfo-NHS ester intermediate which reacts with the primary amine.[18] The two-stage reaction produces higher yields of amide bond formation than occurs from a reaction with EDC alone.

A total of 50 mg (ca. 0.08 mmol) of tiopronin–MPC was dissolved in 10 mL of H_2O. To the MPC/water solution was added 153 mg of EDC and 68 mg of sulfo-NHS. The solution was stirred for 20 min. To this solution was added 0.8 mmol of LKα14. The product was purified by dialysis for 48 h (the water was changed every ~12 h) using SnakeSkin membrane from Pierce Chemical Co. with a 7000 g/mol molecular weight cutoff. This ensured removal of biproducts and unbound LKα14. The beads settled to the bottom of the dialysis tube. The dialyzed aggregated material was spun at 1700*g* for 5 min to isolate the precipitate, and after decanting, it was dried under a vacuum and used without further purification.

NMR Spectroscopy. NMR experiments were carried out on a 9.4 T magnet with a home-built spectrometer.[19] The NMR probe used was a home-built HFXY probe[20] with the X-channel tuned to the ^{13}C Larmor frequency (100.7 MHz). Cross-polarization (CP) experiments used a 2-ms contact time and a ^1H 90° pulse width of 4 μs followed by a contact time of 2 ms. For the dipolar recoupling with a windowless sequence (DRAWS)[21–23] and double-

(17) Templeton, A. C.; Chen, S.; Gross, S. M.; Murray, R. W. *Langmuir* **1999**, *15*, 66–76

(18) Hermanson, G. T. *Bioconjugate Techniques*; Academic Press: New York, 1996.

(19) Gladden, J.; Drobny, G. P. Unpublished result.

(20) Stringer, J. S. Ph.D. Thesis, Department of Chemistry, University of Washington, Seattle, WA, 1998.

(21) Gregory, D. M.; Mitchell, D. J.; Stringer, J. A.; Kiihne, S.; Shiels, J. C.; Callahan, J.; Mehta, M. A.; Drobny, G. P. *Chem. Phys. Lett.* **1995**, *246*, 654–663.

(22) Mehta, M. A.; Gregory, D. M.; Kiihne, S.; Mitchell, D. J.; Hatcher, M. E.; Shiels, J. C.; Drobny, G. P. *Solid State Nucl. Magn. Reson.* **1996**, *7*, 211–228.

(23) Gregory, D. M.; Mehta, M. A.; Shiels, J. C.; Drobny, G. P. *J. Chem. Phys.* **1997**, *107*, 28–42.

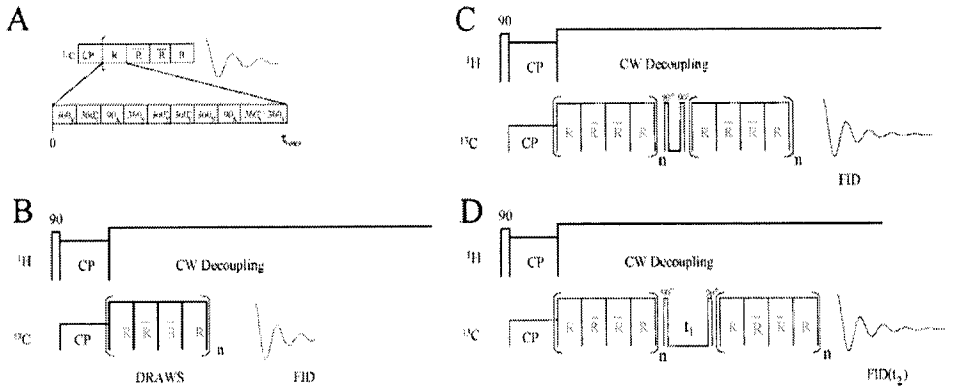

Figure 2. (A) DRAWS pulse cycle and supercycle. *R* indicates a cycle of DRAWS. $\bar{R}$ indicates a cycle of DRAWS that has been shifted in phase by 180° relative to the *R* cycle. (B) DRAWS dipolar recoupling pulse sequence. (C) DQFDRAWS. (D) Two-dimensional DQDRAWS pulse sequence.

quantum dipolar recoupling with a windowless sequence (DQDRAWS)[24] experiments a spinning frequency of 3557 Hz was used corresponding to a ^{13}C radio frequency field of 30.24 kHz. Continuous ^{1}H decoupling of 110 kHz was used during the DRAWS sequence and FID collection. The DRAWS pulse sequence consists of a windowless pulse train applied in synchrony with the rotor cycle (see Figure 2A). The transverse magnetization is then observed stroboscopically every four rotor cycles and normalized with respect to the magnetization observed without any DRAWS dephasing (Figure 2B). Each DRAWS experiment was run at least five times, using either 128 or 512 scans per spectrum and a repetition time of 4 s. Adsorbed samples consisted of approximately 10 mg of peptide covalently bound to 100 mg of tiopronin–MPC packed into a 5-mm rotor. Simulated DRAWS decay curves were calculated using numerical methods that incorporated the observed relaxation times from singly labeled peptides, chemical shift anisotropies (CSAs), and experimental parameters.

DQ-filtered DRAWS[25] (DQFDRAWS, see Figure 2C) experiments were carried out first performing a CP pulse sequence (4-μs ^{1}H 90 followed by a 2-ms mixing time), followed by a DRAWS pulse sequence of 3–6-ms duration, using a ^{13}C field of 34.0 kHz. A 90° pulse following the DRAWS pulse sequence generates double-quantum coherence. In the double-quantum buildup experiment, this coherence is immediately transferred back to single-quantum coherence by a second 90° pulse followed by a DRAWS mixing sequence for the same amount of time. The buildup of double-quantum coherence was then monitored as a function of the DRAWS mixing time to determine dipolar couplings. Proton decoupling of > 110 kHz was applied throughout the DRAWS, evolution, and acquisition periods.

In the two-dimensional DQDRAWS experiment (see Figure 2D), the DRAWS pulse sequence is again applied for 4–6 ms. But in the two-dimensional DQDRAWS experiment, after the magnetization is transferred to the double-quantum state by a 90° pulse, it is allowed to evolve under the chemical shift and dipolar interactions for 0–3 ms, corresponding to 120 t_1 time points with a dwell time of 25 μs. The magnetization is then transferred back to an observable state by a second 90° pulse and reapplying the DRAWS mixing sequence for the same amount of time. Proton decoupling of > 110 kHz was applied throughout the DRAWS, evolution, and acquisition periods. The samples were spun at 4000 ± 5 Hz to match with the 250-μs DRAWS cycle time. The DQDRAWS were simulated as a function of t_1 evolution using code previously described operating in a Matlab environment. Torsion angle values were obtained from a least-squares minimization of the evolution in the t_1 dimension. Simulations incorporated the observed CSAs, experimental parameters, and principal axes of the CSAs relative to the amide bonds (molecular frame) as previously described.

Results

Chemical Shift Analysis of Peptides Adsorbed to Gold Nanoparticles. Qualitative information about peptide secondary structure may be determined by measuring isotropic chemical shifts and the CSA tensor.[26–31] Figure 3A shows the ^{13}C chemical shift spectra of the LKα14 peptide, ^{13}C enriched at the C1 carbonyl positions of L4 and L5, lyophilized from concentrated (> 1 mM) solution, and Figure 3B is the ^{13}C chemical shift spectra of the LKα14 peptide immobilized by covalent bonding to the protected MPC. In both the spectra, the isotope enriched carbonyl carbons have a chemical shift of about 177 ppm relative to tetramethylsilane, a CSA of 150 ppm, and an asymmetry of 0.6. Previously it has been shown that these values correlate to helical structure in peptides.[29] Figure 4A,B shows double-quantum-filtered spectra from the surface-attached LKα14 peptide doubly carbonyl-labeled at L4/L5 and L11/L12, respectively. The similarity of these spectra indicates a helical structure throughout this peptide when attached to the MPC particle surface. These results indicate that the formation of helical secondary structure in solution precedes covalent attachment to the MPC surface, at least at higher concentrations. Note that interference from the natural abundance carboxyl signal of tiopronin is apparent in Figure 3A,B. In Figure 3A the background arises from the ^{13}C spins at natural abundance in the LKα14 peptide. In Figure 3B the background is due to the natural abundance background of the LKα14 peptide and to a greater extent to the methine carbon and the carbons in the proprionyl side chain of tiopronin. Figure 4 shows that double-quantum filtering essentially removes the natural abundance background, so double-quantum

(24) Bower, P. V.; Oyler, N.; Mehta, M. A.; Long, J. R.; Stayton, P. S.; Drobny, G. P. *J. Am. Chem. Soc.* **1999**, *121*, 8373–8375.
(25) Karlsson, T.; Popham, J. M.; Long, J. R.; Drobny, G. P. A study of homonuclear dipolar recoupling pulse sequences in solid-state nuclear magnetic resonance. *J. Am. Chem. Soc.* **2003**, *125* (24), 7394–7407.
(26) Asakawa, N.; Kurosu, H.; Ando, I.; Shoji, A.; Ozaki, T. *J. Mol. Struct.* **1994**, *317*, 119–129.
(27) Tsuchiya, K.; Takahashi, A.; Takeda, N.; Asakawa, N.; Kuroki, S.; Ando, I.; Shoji, A.; Ozaki, T. *J. Mol. Struct.* **1995**, *350*, 233–240.
(28) Kameda, T.; Takeda, N.; Kuorki, S.; Kurosu, H.; Ando, S.; Ando, I.; Shoji, A.; Ozaki, T. *J. Mol. Struct.* **1996**, *384*, 17–23.
(29) Ando, I.; Kuroki, S. *The Encyclopedia of NMR*; John Wiley: New York, 1996; pp 4458–4463.
(30) Kameda, T.; Ando, I. *J. Mol. Struct.* **1997**, *412*, 197–203.
(31) Ando, I.; Kameda, T.; Asakawa, N.; Kuroki, S.; Kurosu, H. *J. Mol. Struct.* **1998**, *441*, 213–230.

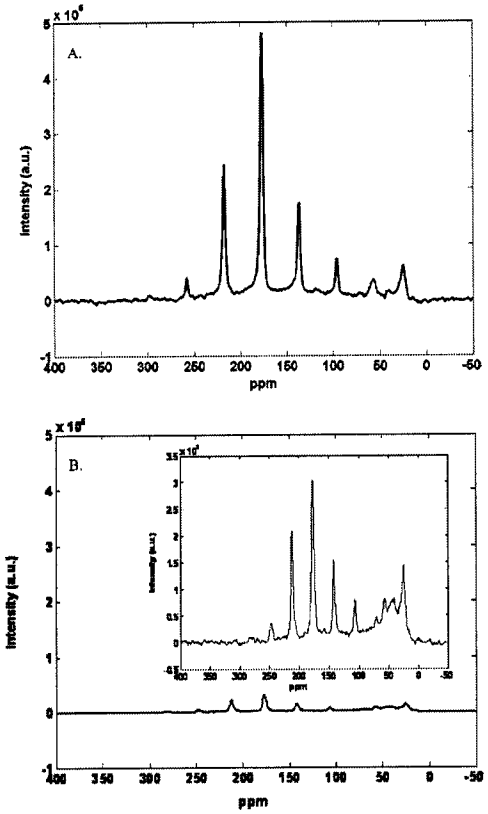

Figure 3. (A) ^{13}C CPMAS spectrum of LKα14, enriched at the carbonyl positions of L4 and L5 and in aggregated, lyophilized form. (B) ^{13}C CPMAS spectrum of LKα14 adsorbed onto tiopronin-protected gold particles (inset, enlarged view of spectrum).

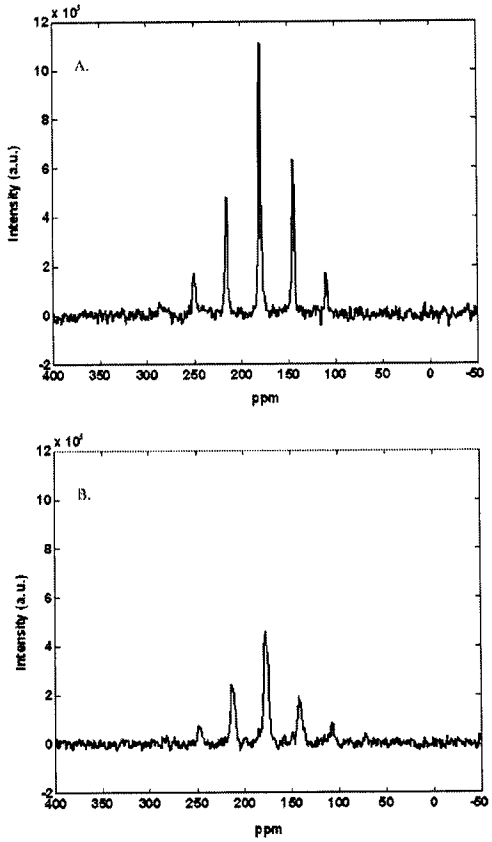

Figure 4. Double-quantum filtered ^{13}C CPMAS spectra of LKα14 adsorbed onto tiopronin-protected gold nanoparticles. (A) Adsorbed LKα14 ^{13}C enriched at the carbonyl sites of L4/L5. 1280 scans, 3558-Hz MAS rotation rate. (B) Adsorbed LKα14 ^{13}C enriched at the carbonyl sites of L11/L12. 3840 scans, 3558-Hz MAS rotation rate.

buildup experiments were used to measure the distances between adjacent carbonyl carbons in the peptide backbones.

The CSA values can also provide information about the presence of dynamics. As mobility increases, the anisotropy will become increasingly averaged until it approaches the liquid state spectrum, the completely averaged or isotropic state. Insofar as the spectra in Figures 3 and 4 indicate CSA values that approach rigid lattice parameters, the CSAs indicate that there is little or no peptide motion on the time scale (< kilohertz) of the NMR experiments at either the L4/L5 sites or the L11/L12 sites. Measurement of the ^{13}C $T_{1\rho}$ relaxation constants[32] (data not shown) and the buildup of double-quantum efficiency in the DQDRAWS experiment also indicate there is no detectable motion of the adsorbed peptides on the time scales of the experiments.

Figure 5A shows the ^{15}N cross-polarization magic-angle spinning (CPMAS) spectra of the ϵ ^{15}N spin of K7 in LKα14, immobilized on MPC particles, acquired at a spinning rate of 1800 Hz. As a result of the limited amount of material attached to the MPC surface and the low proton decoupling power used, the signal-to-noise ratios are not sufficient for detailed simulation of the CSA anisotropy, but the data are sufficient for demonstrating that the peptide is covalently bound to the carboxyl groups of the MPC surface and that the peptide is immobilized on the surface. From the CPMAS spectrum the CSA is in the range of 110−130 ppm, which is characteristic of amide ^{15}N CSA values in peptides and far greater than would be expected for the CSA of an ϵ amine ^{15}N in lysine. This indicates that the ϵ ^{15}N of K7 is covalently bound to the carboxyl group of tiopronin. The fact that the CSA lies in the range of amide ^{15}N spins in crystalline peptides further indicates that LKα14 is substantially immobilized on the MPC surface. The small peak observed at slightly over 110 ppm relative to liquid NH_3 is very likely due to the free side-chain amine group of lysine[38] and indicates only about 5% of the peptide is untethered to the MPC.

MPC-Bound Peptide Conformation from Dipolar Recoupling Studies. Higher resolution determination of the secondary structure of the MPC-bound peptides was accomplished using the DQFDRAWS experiment to

(32) Schaefer, J.; Stejskal, E. O.; Buchdahl, R. *Macromolecules* **1977**, *10*, 384−405.

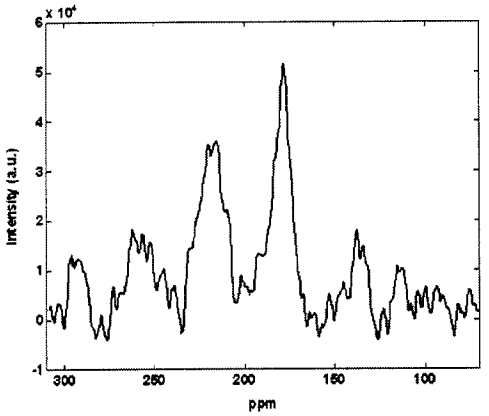

Figure 5. CPMAS ^{15}N spectra of LKα14 with lysine-ε-^{15}N incorporated at K7 and covalently immobilized on tiopronin-protected gold nanoparticles (ν_{rot} = 1800 Hz). Spectra referenced to liquid NH_3.

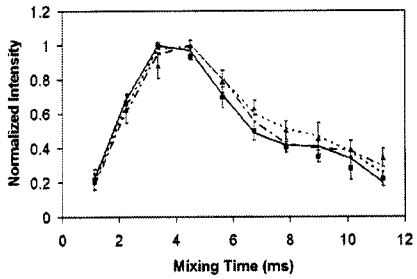

Figure 6. Buildup of ^{13}C double-quantum coherence accomplished with the DRAWS pulse sequence shown in Figure 2C. Closed squares, LKα14 ^{13}C enriched at the carbonyl positions of L4/L5 and adsorbed onto tiopronin-protected gold nanoparticles; closed triangles: LKα14 ^{13}C enriched at the carbonyl positions of L11/L12 and adsorbed onto tiopronin-protected gold nanoparticles; dashed line, simulated data assuming model consisting of 20% β sheet, 80% alpha helix; dashed–dotted line, carbonyl–carbonyl distance = 3.10 Å; solid line, carbonyl–carbonyl distance = 3.02 Å.

measure φ and DQDRAWS SSNMR experiment for simultaneous measurement of (φ, ψ). Although less sensitive than direct detection of recoupled dipolar dephasing, DQFDRAWS was used for the following reasons. When peptides are covalently bound to tiopronin MPCs, a significant component of the ^{13}C spectral intensity arises from the natural abundance ^{13}C contribution from the tiopronin component of the MPC. This background signal complicates any quantitative analysis of single quantum spectra and, thus, must be removed to enable a high-resolution structural analysis of the MPC-bound peptide.

Figure 6 shows the DQFDRAWS results for the LKα14 covalently immobilized on MPC particles. As described above, samples of LKα14 were pairwise enriched at the carbonyl sites of L4/L5 and L11/L12. In the former sample the carbonyl–carbonyl DQFDRAWS data were fitted to a model in which the internuclear distance is 3.10 Å, corresponding to $\phi = 78°$, which deviates somewhat from values typical of α-helical peptides and approaches the range of 3_{10} helices.[33] The fit can be improved, as shown in Figure 6, by adding small populations of nonhelical

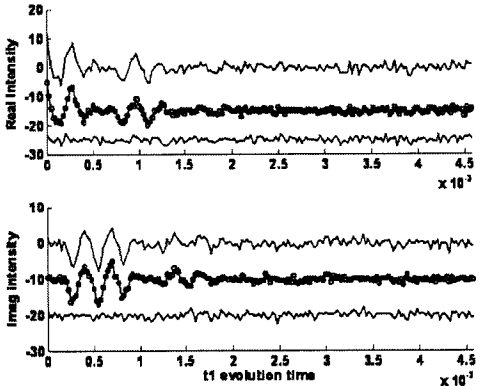

Figure 7. Real (top) and imaginary (bottom) components of the double-quantum interferogram, obtained from L11/L12 carbonyl labeled LKα14 adsorbed onto tiopronin-protected gold nanoparticles. In both plots the line is a simulation, produced assuming a carbonyl–carbonyl distance of 3.02 Å, corresponding to $\phi = 64°$ and $\psi = -30 \pm 5°$. The open circles correspond to experimental data, and the dashed line is the residual.

conformers, but in all models the major conformer has a ϕ value in the α-helical region. Even given the limits of experimental accuracy, as indicated by the error bars in the DQFDRAWS data, basically three pieces of evidence indicate extended conformers, if present, cannot be in large abundance: the ^{13}C carbonyl chemical shift is typical of predominantly helical peptides, the peak of the DQFDRAWS buildup curve would be extended to longer times if extended conformers were in high abundance, and large populations of nonhelical conformers would perturb the sideband pattern of the double-quantum spectrum, discussed below. The L11/L12 sample yields DQFDRAWS data with a similar interpretation. The carbonyl–carbonyl distance is 3.02 Å, corresponding to $\phi = 64°$, again in the α-helical region of the Ramachandran map.

A more thorough definition of the secondary structure of the MPC-bound peptide is obtained from the projection of the two-dimensional DQDRAWS spectrum. For the L11/L12 doubly carbonyl enriched sample, the double-quantum projection is shown in Figure 7. As shown in Figure 7, the real and imaginary double-quantum interferograms are actually fitted and indicated a value of $\psi = -30 \pm 5°$. The simulated double-quantum interferograms were produced assuming a ϕ value derived from the DQFDRAWS experiment. When the two data sets are combined the L11/L12 labels yield torsion angle values of $(\phi, \psi) = (-64 \pm 5°, -30 \pm 5°)$, values typical of well-ordered helical peptides. For comparison, the Fourier transform of the DQDRAWS interferogram is shown in Figure 8 together with the corresponding simulation.

Discussion

Our long-term goal is to design well-structured and oriented peptide or protein surface coatings on biomaterial, tissue engineering, and device surfaces (e.g., diagnostic, chip, microfluidic channels). This study is the most recent effort aimed at using SSNMR to determine the influence that surface chemistry has on the structure of adsorbed peptide and protein coatings. The ability to control peptide

(33) Millhauser, G. L. *Biochemistry* **1995**, *34*, 3873–3877.

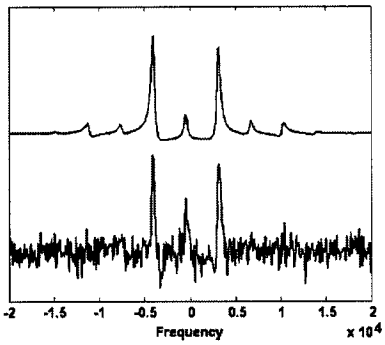

Figure 8. Real component of the complex Fourier transform of the simulation and data in Figure 7. The top is the simulated transform, and the bottom is the experimental transform.

structure and orientation on material surfaces enhances their ability to display signal sequences that interact with target cell receptors, to display larger proteins on chip surfaces, and to open avenues for using specific side-chain residues with defined periodicity as templates on nanoparticles.

Here we have utilized periodic peptide sequences first designed and shown to form helical structures at the air–water interface by DeGrado and Lear.[16] In a recent study we showed that peptides composed of periodic alternations of leucine and lysine residues form defined helices on hydrophobic surfaces such as polystyrene, although the mechanistic assembly process was very different from the process occurring at the air–water interface as reported by DeGrado and Lear.[16] We found that in cases where peptides were lyophilized from > 1 mM solution, structural changes that occur upon adsorption are minimal, at least for longer peptides. This situation is exemplified in the LKα14 peptide by change in the (ϕ, ψ) torsion angles from $(-63, -39)$ in the aggregated form to $(-65, -36)$ when adsorbed onto polystyrene, with the leucines being more aligned along one side of the peptide a situation that likely maximizes interactions with the hydrophobic surface.

In the present study a similar peptide assembly was accomplished on a hydrophilic surface composed of carboxyl-terminated alkanethiolates self-assembled onto colloidal gold particles. LKα14 peptide, shown to be helical in aggregated form, maintains a helical secondary structure when covalently tethered to the surface carboxyl groups. The explanation is similar to that suggested by experiments performed on peptides adsorbed onto hydrophobic surfaces: the helical secondary structure places the primary amine groups of the lysine side chains on one surface of the helix, thus, maximizing exposure of these functional groups to the hydrophilic surface. By forming specific secondary structures on the MPC particle surface, the exposed helical face can also be utilized for orthogonal chemistry.

A key component of the approach described in our earlier paper[34] and applied in the present work is the verification of structure on the relevant biomaterial surfaces using SSNMR.[35–37] SSNMR can provide high-resolution structural and dynamic information about peptides on biomaterial surfaces. The combination of $^{13}C/^{15}N$ chemical shift information, DQFDRAWS and DQDRAWS techniques, elucidated the molecular structure and dynamics of the LK peptides covalently attached to the MPC particle surface. The advantage of the SSNMR approach is the degree to which local structure and dynamics can be quantified in biocomposites, where low solubility and lack of long range order preclude the use of more traditional biostructural techniques like solution NMR and X-ray crystallography. A disadvantage of SSNMR in general and double-quantum methods in particular is low sensitivity, an issue partly addressed by the use of MPCs.

This work further emphasizes the complexity of the interaction between peptides and the biomaterial surface, in this case a MPC particle surface. In the earlier study of LK peptides adsorbed via the hydrophobic effect onto polystyrene bead surfaces, it was established that an equilibrium exists between unfolded peptides and folded peptide assemblies in solution, as well as between the soluble peptide assemblies and adsorbed peptides. Once the peptides are covalently attached to the MPC particle surface from aqueous solution, they are immobile on the NMR time scale along the entire length of the peptide. SSNMR structural measurements indicate adsorption is accompanied by a slight change in the backbone torsion angles. This may be a consequence of the peptides adsorbing on an immobile, two-dimensional surface rather than interacting with other flexible peptides to reach an energy minimum. Although only two sets of torsion angles were studied for each peptide, with sites located near the center and ends of the LKα14 molecule, the small size of the peptide and the low fraction of untethered lysine side chains makes it unlikely that large portions of the peptide removed from the areas of labeling deviate greatly from a helical structure or are mobile. The fact that the LKα14 peptides attach to the carboxylated MPC particle surface in a helical secondary structure is likely a consequence of the fact that the helix exposes a maximum number of lysine residues for attachment to the MPC particle surface. Modifying the identity of the exposed amino acid side chains may be used to control electrostatic properties, spacing of pendant molecules, and so forth. It may also provide interesting possibilities to perform orthogonal grafting chemistry off side chains that have a well-defined periodic registry to control graft periodicity and density.

Acknowledgment. We gratefully acknowledge the support provided by the National Science Foundation (grant numbers EEC-9529161 and DMR-0110505) and by the National Dental Institute (DE 12554). P. V. Bower acknowledges support from the Danish Research Academy. Helpful and informative discussions with Professor David G Castner and Nathan Oyler are gratefully acknowledged.

LA040092W

(34) Long, J. R.; Oyler, N.; Drobny, G. P.; Stayton, P. S. Assembly of alpha-helical peptide coatings on hydrophobic surfaces. *J. Am. Chem. Soc.* **2002**, *124* (22), 6297–6303.

(35) Drobny, G. P.; Long, J. R.; Shaw, W. J.; Cotten, M.; Stayton, P. S. Structure and dynamics of proteins adsorbed to biomaterial interfaces. *Encyclopedia of Nuclear Magnetic Resonance* **2002**, *9*, 458–468.

(36) Shaw, W. J.; Long, J. R.; Drobny, G. P.; Stayton, P. S. NMR Studies of the Structure and Dynamics of Proteins Adsorbed to Biomaterial Interfaces. *Crit. Rev. Oral Biol. Med.* **2003**, *14* (5), 370–376.

(37) Drobny, G. P.; Cotten, M.; Long, J. R.; Stayton, P. S. NMR Studies of the Structure and Dynamics of Proteins Adsorbed to Biomaterial Interfaces. *Annu. Rev. Phys. Chem.* **2003**, *54*, 531–573.

(38) Source: Statistics Calculated for All Chemical Shifts from Atoms in the 20 Common Amino Acids. http://www.bmrb.wisc.edu/ref_info/statful.htm (accessed 2004). For the side-chain amine of lysine the minimum shift reported is 7.77 ppm (relative to liquid ammonia), and the maximum shift is 131.04 ppm, with an average shift of 48.17 ppm and a standard deviation of 36.38 ppm.

Appendix C: Using Solid-State $^{31}P\{^{19}F\}$ REDOR NMR to Measure Distances between a Trifluoromethyl Group and a Phosphorothioate in Nucleic Acids

Using Solid-State $^{31}P\{^{19}F\}$ REDOR NMR to Measure Distances between a Trifluoromethyl Group and a Phosphodiester in Nucleic Acids

Elizabeth A. Louie, Panadda Chirakul, Vinodhkumar Raghunathan, Snorri Th. Sigurdsson[‡], *Gary P. Drobny*[*]

University of Washington, Chemistry Department, Campus Box 351700, Seattle, WA 98195-1700

[*]drobny@chem.washington.edu

[‡]present address: University of Iceland, Science Institute, Dunhaga 3, IS-107 Reykjavik, Iceland

Email address: snorrisi@hi.is

Abstract

REDOR is a solid-state NMR technique frequently applied to biological structure problems. Through incorporation of phosphorothioate groups in the nucleic acid backbone and mono-fluorinated nucleotides, $^{31}P\{^{19}F\}$ REDOR has been used to study the binding of DNA to drugs and RNA to proteins through the detection of internuclear distances as large as 13-14 Å. In this work, $^{31}P\{^{19}F\}$ REDOR is further refined for use in nucleic acids by the combined use of selective placement of phosphorothioate groups and the introduction of nucleotides containing trifluoromethyl ($-CF_3$) groups. To ascertain the REDOR-detectable distance limit between an unique phosphorous spin and a trifluoromethyl group and to assess interference from intermolecular couplings, a series of model compounds and DNA dodecamers were synthesized each containing a unique phosphorous label and trifluoromethyl group or a single ^{19}F nucleus. The dipolar coupling constants of the various ^{31}P and ^{19}F or $-CF_3$ containing compounds were compared using experimental and theoretical dephasing curves involving several models for intermolecular interactions.

Keywords:

Solid-state nuclear magnetic resonance; $^{31}P\{^{19}F\}$ REDOR; Rotational-echo double resonance; Dipolar recoupling; Internuclear distance; Trifluoromethyl group.

Introduction

Solid-state nuclear magnetic resonance (NMR) spectroscopy is widely used to study the structure of biomolecules and biological complexes that are not easily crystallized or dissolved, and thus cannot be conveniently studied by x-ray crystallography and solution-state NMR, respectively. The distance range accessible by REDOR generally exceeds that of NOE or residual dipolar coupling measurements, therefore structural features that must be derived indirectly from short range distance measurements using NOE data can often be directly observed using REDOR [16,17]. For example, $^{31}P\{^{19}F\}$ REDOR has been implemented to measure direct changes in long-range protein structure upon ligand binding [43], and changes in minor groove width of DNA oligomers upon binding distamycin [44,45] with reported ^{31}P to ^{19}F internuclear distances of approximately 16 and 13.5 Å, respectively. These are among the longest internuclear distances measured by NMR methods.

The heteronuclear dipolar coupling constant D_{IS} is directly related to the gyromagnetic ratio (γ_I, γ_S) of the two spins (I, S) of interest and inversely proportional to the cube of the internuclear distance $r_{I\text{-}S}$: $D \propto \gamma_I\gamma_S/r_{I\text{-}S}^3$. Therefore, nuclear spins with larger magnetic moments, and thus the larger gyromagnetic ratios, will result in larger dipolar coupling constants for a given distance than nuclear spins with smaller gyromagnetic ratios. The ^{13}C nucleus is a mainstay for solid-state distance measurements, with the longest ^{13}C distances measured by dipolar recoupling in the neighborhood of 6 Å [43], corresponding to a dipolar coupling of about 35 Hz. In contrast, ^{19}F has a gyromagnetic ratio over 3.5 times the size of ^{13}C and two ^{19}F spins separated by 6 Å have a dipolar coupling of over 490 Hz, while two ^{19}F spins separated by 14.5 Å have a dipolar coupling of about 35 Hz. But in practice, ^{19}F-^{19}F homonuclear recoupling seems limited, at least in nucleic acids, to a maximum distance range of 9-10 Å [36];

recent work by McDermott and coworkers [21] using linear polymers with distally attached trifluoromethyl groups advanced that limit to about 12 Å. A complication that may arise in ^{19}F-^{19}F recoupling that is at least partly responsible for the attenuated upper limit of distance measurement is incomplete decoupling of ^{19}F-^{1}H dipolar interactions.

For the purpose of measuring internuclear distances greater than 12 Å, $^{31}P\{^{19}F\}$ REDOR has shown considerable promise. A ^{31}P spin, with a somewhat smaller magnetic moment, separated by 11 Å from a ^{19}F spin has a dipolar coupling of about 35 Hz. Due to the smaller magnetic moment and because most biologically relevant ^{31}P spins are in phosphate groups, ^{31}P-^{1}H decoupling during $^{31}P\{^{19}F\}$ REDOR is not as problematic as ^{19}F-^{1}H decoupling during ^{19}F-^{19}F recoupling. The long T_2 of ^{31}P under conditions of the REDOR experiment enables the measurement of ^{31}P-^{19}F distances of up to 16 Å (D_{IS} = 11 Hz) as demonstrated by Schaefer and coworkers in a study of a complex of the enzyme 5-enolpyruvylshikimate-3-phosphate (EPSP) and shikimate-3-phosphate (S3P) [43].

In nucleic acids, and especially in DNA, the redundancy of the phosphodiesters in the backbone results in a poorly resolved ^{31}P NMR spectrum [44]. To enable site-specific detection of ^{31}P-^{19}F distances during REDOR, a single phosphate group in DNA or RNA is replaced by a phosphorothioate group. The ^{31}P in a phosphorothioate group is shifted approximately 55 ppm from the ^{31}P phosphate group signal in DNA and RNA [44]. Selective placement of phosphorothioate groups in combination with ^{19}F-substituted nucleotides allows detection of ^{31}P-^{19}F distances site specifically. ^{31}P-^{19}F distances spanning the minor groove of a DNA oligomer have been measured as a function of distamycin-DNA binding stoichiometry [45], and for 2:1 drug:DNA binding stoichiometry a 13.5 Å (D_{IS} = 19 Hz) distance was determined [45].

Even the 16 Å limit achieved by $^{31}P\{^{19}F\}$ may be insufficient for some applications, and the acquisition time necessary to observe the effect of weak ^{31}P-^{19}F dipolar couplings in a REDOR experiment may prove impractical in some cases. For example, it may prove desirable to measure changes in the major groove width of DNA, or changes in RNA tertiary structure as a result of protein binding. Such experiments may require measurement of ^{31}P-^{19}F distances of 16 Å or more. Also, although measurement of ^{31}P-^{19}F dipolar couplings in the 12-16 Å range is feasible, in some cases REDOR measurements are susceptible to interference from intermolecular couplings. One way to extend the range of ^{31}P REDOR is to dephase ^{31}P spins with the fluorines of a trifluoromethyl (CF_3) group. For instance, if an isolated ^{31}P-^{19}F spin pair is separated by 16 Å, the corresponding dipolar coupling constant is about 11 Hz. The corresponding amount of REDOR dephasing is 11% at 30 ms. If instead the ^{31}P spin is coupled to the three ^{19}F spins of a rapidly rotating trifluoromethyl group, REDOR data roughly equivalent to the 16 Å ^{31}P-^{19}F pair is achieved for a distance of 19 Å between the ^{31}P spin and the "pseudo-atom" center of the trifluoromethyl group. Recently, Schaefer and coworkers have determined the conformation of a bound trifluoromethylketal substituted shikimate-based bisubstrate inhibitor (CF_3-SBBI) to EPSP using $^{31}P\{^{19}F_3\}$ REDOR [77] and measured a distance of 8.3 Å. ($\{^{19}F_3\}$ is used to designate the dephasing of the three fluorines from a rotating -CF_3 group.) However, a distance of less than 12 Å is believed to be somewhat moderate for recoupling ^{31}P to the ^{19}F spin of a rotating -CF_3 group due to its high gyromagnetic ratio. Thus, investigating the limitations of dipolar recoupling of ^{31}P and ^{19}F of a rotating -CF_3 group is worth exploring when structural information is desired at the molecular level for large biomolecular systems.

The basic principles of REDOR dephasing by multiple spins in the presence of molecular motion have been discussed by Goetz and Schaefer [20], with specific reference to ^{13}C spins dephased by $-CF_3$ groups. A primary feature of this type of REDOR is that even though the ^{19}F spins are strongly dipolar coupled, the equality of the averaged ^{31}P-^{19}F dipolar couplings which results from the rotation of the trifluoromethyl group removes the effect of the ^{19}F-^{19}F couplings from the REDOR data, at least to second order. Therefore, $^{31}P\{^{19}F_3\}$ REDOR has excellent prospects for applications in nucleic acid problems where a long-range distance measurement is desired.

In this work, we accomplish two objectives. First, we demonstrate the degree of perturbation introduced by trifluoromethyl groups by comparative measurements of DNA helix stability and by direct comparison of distances measured in DNA by $^{31}P\{^{19}F_3\}$ REDOR. Second, we use model compound studies and simulations to assess the degree of interference in REDOR measurements from intermolecular ^{31}P-$^{19}F_3$ dipolar couplings.

Materials and Methods

General. The first four model compounds (**1-4**) shown in Figure 1 were synthesized from 4-fluorophenol **(1a)**, α,α,α-trifluoro-*p*-cresol **(2a)**, 4-fluoro-4-hydroxybenzophenone **(3a)**, and 4-4-(trifluoromethyl)phenoxyphenol **(4a),** which were purchased from Aldrich. Ethylthiotetrazole and 2-cynanoethyl diisopropylchlorophosphoramidite were purchased from Glen Research and Chem Genes, respectively.Acetonitrile and dichloromethane were dried over calcium hydride followed by distillation under argon. Figure 2 shows the general scheme for the synthesis of compounds **1-4**. In general, all reactions were run under argon atmosphere unless otherwise noted. Flash column chromatography was carried out with EM type 60 (230 - 400 mesh) silica gel. Cation exchange chromatography was performed on MP-50 resin, grade 100-20 mesh, hydrogen

form which was pretreated with water, 1.00 N NaOH, then neutralized with water until pH 7.0. Preparative RP-HPLC separations were performed using a Dynamax C18 column (Rainin, 25 cm, 4.6 mm ID, 5 μm, 300 Å) and the solvent gradients for preparative separation, RP-HPLC were run at 10 mL/min as follows: Gradient A: solvent A, 100 mM Et_3NHOAc (pH 7.0); solvent B, CH_3CN; 92% A for initial, 12 min linear gradient to 61% A, 8 min linear gradient to 30% A, isocratic for 3 min, 3 min linear gradient to initial conditions. Gradient B: the same as gradient A except 95% A for initial, 15 min linear gradient to 30% A, isocratic for 10 min, then a 5 min linear gradient to initial conditions.

*Synthesis and Purification of fluorinated DNA Oligomers (**5** and **6**) and their complementary sequence.* The DNA, 5'-d(CGCATT-(pS)-TT-5-FU-GCG)-3' (5), 5'd(CGCATT-(pS)-TT-5-CF3U-GCG)-3' (6), and 5'-(dCGCAAAAATGCG)-3', were synthesized on an Applied Biosystems Model 394 synthesizer. DNA incorporated with 5-fluoro-2'deoxyuridine was achieved by using 5'-(4,4'-dimethoxytrityl)-3'-(cyanoethyl)phosphoramidite-2'deoxy-5-(fluoromethyl)uridine (Glen Research). The usual acetyl (Ac) protected dT, dG, dA, and dC CE phosphoramidites (Glen Research) were used. The DNA incorporated with the -CF3 group was synthesized with 5'- (4,4'-dimethoxytrityl)-3'-(cyanoethyl)phosphoramidite-2'deoxy-5-(trifluoromethyl)uridine [34,78,79], while using using PAC- phosphoramidites and mild deprotection [34].

Incorporation of phosphorothioates into DNAs was done at the oxidation step in which a sulfurizing agent (Glen Research) is used in place of iodine solution. DNAs were deprotected and cleaved from the resin by using concentrated aqueous ammonia at 55 °C for 16 h. DNA were purified by HPLC (gradient and solvent: 10 μmol DNA was brought up to 8 mL by 100 mM

Et_3NHOAc prep-HPLC: buffer A: 100 mM Et3NHOAc, buffer B: Acetonitrile, 10 mL/min, λ 260, 2 ml loop: 0-13 min @ 2% B, 13-25 min @ 2-15% B, 25-35 min @ 15-35 % B, 35-48 min @35% B, 48-53 min @ 35-2 % B, 53-62 min @ 2% B.

Sample Preparation for NMR Studies

Model Compounds. To dilute the spins, 5 – 10 mg of **1-4** were dissolved in deionized water and diluted with solutions of KBr and/or benzoic acid, lyophilized, and packed in a 5 mm rotor. 60 μL H2O was added to 5 mg (3) and the liquid sample was then placed in a 5 mm rotor with tight end caps.

DNA Samples. The DNAs were salted with 10% (w/w) NaCl and 10% (w/w) Na2EDTA, annealed at 85 °C for ten minutes, lyophilized, and packed in 5 mm ceramic rotors, and placed in an 85% hydration chamber to yield at least 11 waters per nucleotide by weight which ensures that the DNA is in B form [35].

NMR Spectroscopy. All $^{31}P\{^{19}F\}$REDOR experiments were performed on a 4.7 T (200 MHz proton Larmor frequency) magnet, homebuilt MAS triple resonance (^1H, ^{19}F, ^{31}P) probe [36,37], and homebuilt console (J. Gladden and G.P. Drobny, Unpublished work). The ^1H $\pi/2$ pulse was set at 5μs and the ^{31}P and ^{19}F πpulses were 10 μs and 7 μs,respectively. The ^1H and ^{31}P cross polarization (CP) time was 2 ms. ^1H decoupling was set at 100-120 kHz during evolution and 80 kHz during acquisition [19,80,81]. Hydrated DNA or samples diluted in water were run at low temperature which ranged from –16° to –27° C with a spinning speed of 5988 Hz. The model compounds **1-4** were spun at 4505 Hz, 5000 Hz or 5988 Hz. The pulse sequence employed was XY8-REDOR [82] as shown in Figure 3. Following generation of ^{31}P magnetization by cross-polarization from the protons, the ^{31}P's are subjected to a series of 180° refocusing pulses. This full echo spectrum is designated So. In the second half

of the experiment, in addition to the ^{31}P refocusing pulses, ^{19}F 180° pulses are added at the middle of the rotor period. These fluorine dephasing pulses reintroduce ^{31}P-^{19}F dipolar couplings averaged by magic angle spinning (MAS), and cause a dephasing of the observed ^{31}P signal. The second half of the spectrum is referred to as S, and the ratio of S/S_0 provides a dephasing curve that can be fit to theoretical equations [16,17] which directly yields the dipolar coupling, D_{PF}, between the ^{31}P and ^{19}F spins. Given the D_{PF}, the internuclear distance, r_{PF}, can be easily calculated from $r_{PF} = [(\gamma_P\gamma_F h)/(4\pi^2 D_{PF})]1/3$ where γ_P and γ_F are the gyromagnetic ratios of the P and F spins, respectively, h is Planck's constant, and D is the dipolar coupling in hertz.

^{19}F observe ^{31}P dephase REDOR can not be exploited due to short T_2 relaxation of the ^{19}F nucleus[83]. Pan reports that after eight-rotor cycles of dephasing the fluorine signal is nearly completely dephased on a fluoroapatite crystal [83]. Dephasing on the ^{31}P nucleus would only be feasible for the small model compounds and not the dsDNA due to the dephasing contribution of ^{31}P nuclei in the phosphate backbone, and thus, the presence of multiple spin dephasers.

Goetz and Schaefer [20] presented closed form numerical algorithms for REDOR dephasing by multiple spins in the presence of molecular motion. The calculation assumes that the ^{19}F -^{19}F homonuclear interaction does not affect REDOR dephasing. For a trifluoromethyl group, fast rotation about the three fold symmetry axis of the CF_3 group ensures that the three fluorine nuclei have identical, motionally averaged chemical shifts and identical motionally-averaged dipolar couplings to the ^{31}P nucleus. In principle, REDOR data will be dependent on the angle between the axis of three fold symmetry of the CF_3 group and the vector pointing from the ^{31}P nuclear coordinate to the "pseudoatom" center of the CF_3 group. The Schaefer group provided

simulations of $^{31}P\{^{19}F_3\}$ REDOR data in this present work include angles of 0° and 90°, the extreme cases.

Determination of error bars in experimental data and uncertainty in distance measurements

The experiments were repeated a minimum of 2-3 times, averaged, and the standard deviation calculated. The error bars in the S/S_0 REDOR dephasing plots were determined by reproducibility of the experiment.

The uncertainty of the distances measured by $^{31}P\{^{19}F$ or $^{19}F_3\}$ REDOR for samples 1-6 were calculated by determining the χ^2 and calculating the variation of χ^2 near a minimum as defined in Bevington [84]. Briefly, the minimum of χ^2 was determined by fitting three points that straddle the minimum of χ^2 vs distance to a quadratic equation, and the uncertainty of the distance was measured by taking the second derivative of χ^2 with respect to the distance [84].

Results and Discussion

Orientation and Theoretical Dephasing Curves of –CF_3 group

The orientation of the fluorines from a $-CF_3$ group with respect to the phosphorous atom can range from 0° to 90°. Figure 4A depicts the 0° orientation where the ^{31}P atom lies along the C_3 axis of the $-CF_3$ group while the 90° orientation shown in Figure 4B is where the ^{31}P atom is in the plane of the three fluorines. In both orientations, the distance simulated is from the center of mass of the three fluorines to the ^{31}P atom.

The simulated ^{31}P-^{19}F REDOR dephasing curves for P-F and P-CF_3 are compared at several distances 6, 9, and 12 Å in Figure 5. For each distance, there are three simulated curves, where the solid line represents the dephasing for a given distance between a ^{31}P atom and a single ^{19}F atom. The short dashed

and dashed lines describe the P-CF_3 simulations where the C_3 axis of the -CF_3 group is oriented at its extreme of either 0° or 90° with respect to the ^{31}P atom, respectively. At 6 Å, the P-F and P-CF_3 dephasing curves are similar to one another. For the 9 and 12 Å dephasing curves, the P-CF_3 curves show greater dephasing dephased than the P-F curves.

At distances greater than 12 Å, the REDOR dephasing curve shows a decreasing dependence upon the orientation of the –CF_3 group to the point that the apparent dephasing is nearly the same. However, at short distances (~ 6 Å), the dephasing is more sensitive to the orientation of the CF_3 group. Figure 5 shows that at 6 Å, the 90° orientation dephases faster than the 0° orientation. At short distances, the difference in distance from the ^{31}P atom to the center of mass of the three fluorines compared to the distance from the ^{31}P atom to any one of the fluorines becomes significant, and thus the orientation of the -CF_3 group is relevant as compared to the distances, where the orientation is irrelevant. At longer distances (>12 Å), the three fluorines of the –CF_3 group collectively can thus be considered as a "pseudo-atom".

Model Compounds

Model compounds were needed to check experimental parameters and to ensure the accuracy of the distances measured by $^{31}P\{^{19}F\}$ REDOR. Several model compounds were synthesized and investigated in this study. Figure 1 shows the model compounds (**1-4**) that were synthesized, each contained either a unique fluorine atom or –CF_3 group and phosphorous atom. The synthetic pathway of compounds **1-4** is shown in Figure 2. **1** and **2** were specifically designed such that the internuclear distance between ^{31}P and ^{19}F does not vary due to bond rotations. **3** and **4** were synthesized to measure a longer distance than **1** and **2**, however, the distance for both **3** and **4** have an approximate 1.5 Å range due to possible rotation of the C-O bond attached to the phosphate group.

The choice of model compounds was based on structural similarity such that the dephasing profile of a compound with one fluorine could be compared to a similar compound where a $-CF_3$ group replaces a single –F spin.

Two separate sources were used to determine the theoretical ^{31}P to ^{19}F distances of the model compounds in the study. The first method involves searching the Cambridge Structure Database (CSD) for compounds or fragments of the compounds similar to **1-4**. The distances based on CSD data for structurally similar fragments were compared with the measured distances of the model compounds (**1-4**). Table 1 shows the structures of the crystal fragment with the CSD codes, as well as the distance measured between the phosphorous and fluorine or $-CF_3$ group labels, which are identified as dots on the structure. The REDOR results are discussed below whereby the change in dephasing between the single –F and $-CF_3$ analogues are compared. The second method was a structural minimization using a semi-empirical AM1 closed shell calculation with software provided by Cambridge Soft Corporation. The calculated measurements were used to approximate intermolecular couplings in the model compounds because the fragments of the crystal structures found were not adequate in determination of the next nearest neighbor.

Dephasing Differences between –F and $-CF_3$

In a ^{31}P - ^{19}F spin system, REDOR recouples the direct dipolar coupling between the two nuclei. This coupling is quantified as a dephasing of spin coherences of the observed nucleus (e.g. ^{31}P) caused by the coupled spin (e.g. ^{19}F). The amount of dephasing observed is directly related to the internuclear distance of the two spins by the heteronuclear dipolar coupling. Figure 6, for example, shows a plot of P-F and P-CF_3 distances for a range of coupling constants. At a dipolar coupling of 3 Hz, the difference in distance measureable by P-F and P-CF_3 methods can be as great as 5 Å. Due to limitations of sample

size or rotor size as in solid-state NMR experiments, evolution times of about 20 ms are needed for complete dephasing of a P-F sample at a modest distance of 9 Å. By replacing a single fluorine spin with three fluorine spins of a trifluoromethyl group, the dephasing is increased, and thus a longer internuclear distance can be measured at a shorter evolution time.

REDOR So (full echo) spectra with eight rotor cycles of evolution are shown in Figure 7A and 7B for compound **1** undiluted and diluted in benzoic acid (1:40 mol/mol), respectively. The REDOR dephasing curves for the model compounds (**1-4**) are shown in Fig 8A and 8B. In Figure 8A, the experimental data are shown for compounds 1 and 2 (both diluted in KBr 1:100), along with the 6 Å calculated dephasing curves for P-F and P-CF_3 simulations at 0° and 90°. The X-ray crystal structure distances for compounds **1** and **2** are 6.66 and 7.08 Å, respectively. For compound **1**, the data points follow the 6 Å P-F dephasing curve. The experimental data for **2** fits the calculated dephasing curve of P-CF_3 at 90° up to about 4 ms, and then at longer dephasing times, the data points no longer follow the 6 Å CF_3 90° dephasing curve and begin to dephase more slowly. In addition, **1** was also diluted in benzoic acid at ratios of 1:5 and 1:20 mol/mol. Regardless of the dilution method, the average distances measured for **1** and **2** were shorter than the X-ray crystal distance as shown in Table 1. The crystal structure distance was within the experimental uncertainty of compound **1** but not within the uncertainty for compound 2.

Compounds 3 and 4 were diluted in deionized water (10 mg/30 μL and 10 mg/60 μL) and 1:40 mol/mol benzoic acid, respectively. Fig 8B shows the dephasing curve for 3 diluted in deionized water at a concentration of 10mg/60 μL and 4 diluted with 1:40 mol/mol benzoic acid. The experimental data for **3** best fits the 9 Å P-F dephasing curve and **4** fits between the 8 and 9 Å 90° P-CF_3 dephasing curves. Similar to compounds **1** and **2**, **3** and **4** also show a shorter

measured distance of about 9.3 Å compared to the crystal structure fragment distance of 10.31 and 11.14 Å, respectively. As longer inter-label distances were measured, there was a larger disparity between the crystal structure fragment measurement and to the $^{31}P\{^{19}F\}$ REDOR distances. In addition, the experimental uncertainty for molecules **3** and **4** in some cases was greater than 1 Å, and probably due to heterogeneity in conformation of the sample from rotation of the phosphate group and perhaps the multiple spin couplings from intermolecular effects. The rotation of the C-O bond of the phosphate group for **3** and **4** can possibly contribute a 1.2 to 1.5 Å range in the observed distance.

McDermott and co-workers have used model fluorinated compounds to measure ^{19}F-^{19}F internuclear distances via RFDR [21]. Their solution for avoiding intermolecular dipolar couplings from neighboring fluorinated compounds was the dilution of fluorinated compounds by co-crystallization with nonfluorinated analogues that were structurally similar. In our study, various dilution methods were attempted. For model compound **1**, the dilution methods used were diluting 1:100 mol/mol in KBr, 1:5 and 1:20 mol/mol in benzoic acid. None of the dilution methods showed a significant change in distance measured as reported in Table 1. Thus for compound **2**, the only dilution method used was 1:100 mol/mol KBr. Another dilution method was tried for compound **3**. In Figure 9A, the REDOR dephasing curves are shown for compound 3 undiluted and diluted in a solution of deionized water at a concentration of 10mg/60μL. Comparison of the undiluted case and the diluted cases of compound **3** demonstrates a distance change from 9.0 to 9.3 Å, respectively. The dephasing curves in Figure 9A show that there is a visible dephasing difference and that dilution of the compound in deionized water has some effect in isolating the phosphorous and fluorine spins. Likewise, Figure 9B shows the dephasing curves of compound 4 undiluted and diluted in 1:40 mol/mol benzoic acids, and

also illustrates that dilution of 4 in 1:40 benzoic acid isolates the phosphorous and fluorine spins to some extent.

Attempts were made to dilute the samples further such that intermolecular couplings might be reduced. However, as dilution of sample increased, the signal to noise diminished and experimental points were more scattered at long dephasing times. It has been noted that small fluorinated compounds tend to aggregate and do not make good model compounds (M.E. Merritt personal communication) [37]. McDermott et al. [21] also encountered inhomogeneous or inadequate dilution of samples with their fluorinated model samples. In addition, halogenated organic crystals are also known to aggregate [49,50]. Thus, it is suspected that these apparent intermolecular couplings may be due to aggregation of the fluorines and use of an insufficient molecular mixing method.

Multiple spin simulations and fits

To address the issue of the experimental distances being shorter than the calculated distances for the compounds **1-4**, simulations using SIMPSON [85] were performed to describe possible packing models of the compounds where the intermolecular effects give rise to a distribution of distances and thus, multi-spin effects.

For compound **1**, the energy minimized structure obtained from the AM1 calculation was put in a fictitious cubic crystal cell (Cell constant 10 Å) in the Weblab Viewerlite Visualization program by Accelerys, Inc. This calculation showed the possibility of an intermolecular ^{31}P-^{19}F distance of 3.5 Å that can be seen in Figure 10A. Assuming partial aggregation causing intermolecular effects, the experimental data was fit to a linear combination of two spin and three spin simulations. The best fit occurred at a 90% of a ^{31}P-^{19}F distance of 6 Å and 10% of ^{31}P-^{19}F distances of 6 Å and 3.5 Å as shown in Figure 10B.

For compound 2, the distances obtained from a semi-empirical AM1 closed shell calculation are 7.26 Å, 7.36 Å, and 7.64 Å for the three fluorine atoms respectively from the phosphorus atom. The simulated result is co-plotted with compound 1 in Figure 10B. The best fit simulation considered the center of the CF3 to be 5.34 Å as opposed to the expected 7.42 Å distance from the AM1 calculation. This discrepancy is mostly due to aggregation leading to spin diffusion. Most recent work shows that in cases where multiple dephasers are involved simulation of data requires the exact molecular geometry [G. Goobes, V. Raghunathan, E.A. Louie and G.P. Drobny unpublished results]. Despite the experimental distances being shorter than the calculated distances, the dephasing of compound **2** was greater than compound **1**, as expected due to the $-CF_3$ group in compound **2**.

The AM1 minimized structure for compound **3** suggested that the P-F distance could range between 9.8 to 11.5 Å depending upon the torsion angle of the phosphate group. The $^{31}P\{^{19}F\}$ REDOR data of the undiluted sample of **3**

much shorter than the expected distance as determined from the AM1 calculation.

Fluorinated and Trifluoromethylated DNA samples

The sequences and labeling scheme of the fluorinated DNA (5 and 6) used in this study are shown in Figure 1. The structure of the DNA sequence was selected because it was not self complementary and the x-ray crystal structure was published in the Protein Data Bank (PDB) [47] as code 1BDN [86]. A self-complementary sequence would complicate the analysis due to inter- and intrastrand interactions. The DNA were synthetically modified to accommodate a fluorine or $-CF_3$ group and phosphorothioate for the $^{31}P\{^{19}F\}$ REDOR dephasing comparison studies. Thermodynamic data for DNA duplexes with and without a trifluoromethylated label were compared and previously reported by Markley et al.[34]. Optical melting experiments were performed and it was found that DNA duplex stability at pH 6.9 was lowered slightly (a T_m difference of 3°) due to the incorporation of the trifluoromethyl group [34].

Based on the crystal structure data, the phosphorothioate and –F or $-CF_3$ labels in the duplex DNA were designed to be 12 Å apart. Figure 11 is the $^{31}P\{^{19}F\}$ REDOR So spectrum of dsDNA **5** showing the phosphorothioate peak chemically shifted upfield 55 ppm from the phosphate backbone. The sample was spun at 5988 Hz in order to allow for adequate resolution between the spinning side band peak of the backbone phosphates and the phosphorothioate peak. For the dsDNA samples, **5** and **6**, the dephasing curves are shown in Figure 12A and 12B, respectively. The data points for the dsDNA sample, **5**, fall between the 11 and 13 Å P-F dephasing simulations. A χ^2 plot vs. distance is shown in the inset of Fig 12A where the equation of a parabola was fit to pass through three points that straddle the minimum. From the parabolic fit, the χ^2 minimum and standard deviation can be determined [84]. The best fit for **5** was

12 ± 1 Å, which is in good agreement with the crystal structure distance of 11.89Å. In the case of the dsDNA with the $-CF_3$ group, **6**, the $^{31}P\{^{19}F\}$REDOR experimental points were between the 10 - 14 Å P-CF_3 90° simulations as shown in Figure 12B. The χ^2 is shown in the inset of Figure 12B, and the minimum χ^2 and standard deviation was determined to be 13 ± 2Å, which is also in agreement with the X-ray crystal structure. In addition, by co-plotting the experimental data points of **5** and **6**, as in Figure 12C, the difference in dephasing behavior between the single –F and $-CF_3$ dsDNA is demonstrated, especially at 20 ms.

The intermolecular coupling effects were not observed in the dsDNA samples, likely due to the oligomers self-diluting. The ratio of distance measured to length of the molecule is smaller than the model compounds 1 - 4. The P-F and P-CF_3 labels were strategically placed so that the distance of the labels would be shorter than the length of the duplex 12 mer DNA. This may have contributed to a more accurate distance measurement by preventing intermolecular couplings and better isolating the P-F and P-CF_3 spin pairs. The distance of the P-F or P-CF_3 labels in **1-4** were essentially the length of the molecule, and therefore contributed to intermolecular effects creating an apparent faster dephasing.

Advantages and Disadvantages of $-CF_3$

In deciding when to include a $-CF_3$ group or –F in a sample, the choice depends on the information desired, the system of interest, and placement of the label. Besides the ability to measure a long-range distance with a $-CF_3$ group, there is an advantage of a $-CF_3$ group at short distances, as well. For distances not more than ~6 Å, dephasing is sensitive to the orientation of the $-CF_3$ group relative to the phosphorous nucleus, if the error in the dephasing data points are low. Fig, 8A illustrates that the 6 Å 0° and 90° dephasing curves are sufficiently

distinguishable to allow determination of the orientation of the -CF_3 group relative to the phosphorous nucleus. The first three experimental points of the dephasing curve of **2**, indicated by solid squares, are in good agreement with the theoretical P-F_3 6Å 90° dephasing curve (long dashes). Due to the C-O-P arrangement as in molecule **2**, the -CF_3 group is situated 90° relative to the phosphate atom, which is in agreement with the experimental result. As a result of intermolecular couplings, at longer dephasing times (greater than 5 ms), the experimental results no longer follow the 6Å 90° dephasing curve. At distances greater than 6 Å, the theoretical P-F_3 0° and 90° dephasing curves begin to converge and the orientation of the –CF_3 group can no longer be distinguished. Thus, as seen in the results, there can be a disadvantage to incorporating a –CF_3 group when the molecule of interest is inadequately diluted and/or the distance measured is large compared to the size of the molecule due to intermolecular effect. Thus, the –F label is best used when measuring short distances in order to avoid intermolecular effects. Despite the inadequate molecular mixing causing aggregation or poor dilution of the spins, for compounds **1-4**, it was shown that replacing a –F with a –CF_3 group allowed the dephasing behavior to increase. This trend of increased dephasing was also seen with the dsDNA samples of **5** and **6**. A greater apparent dephasing due to the CF_3 substitution will allow for longer distance measurement especially when working with biological samples in μmol scale quantities.

Limit of P-CF_3 coupling

Table 2 is a theoretical comparison of the amount of dephasing between P-F and P-F_3 and shows that a distance of 20 Å has 8% dephasing after 30 ms [42,87] evolution for a P-F_3 system, which is an estimate of the upper limit of the distance measurable using a –CF_3 group in place of a –F. The Schaefer group [3] has measured a maximum distance of 16 Å (12 Hz) using P-F

REDOR. According to Table 2, P-CF_3 coupling of 12 Hz correlates to a 19 Å. This implies that it is possible to measure a 19 Å distance with P-CF_3 REDOR.

Effective Gamma for "Super" Fluorine in -CF_3 Group

The same dipolar coupling for P-CF_3 and P-F yield different distances due to their difference in dephasing behaviors. Due to the proportional relationship of the gyromagnetic ratios and the dipolar coupling, an average effective gyromagnetic ratio for the fluorines in the -CF_3 group was estimated using $\gamma_{P\text{-}CF3} = \gamma_{P\text{-}F}\,[(r_{P\text{-}CF3})^3/(r_{P\text{-}F})^3]$. The ^{19}F gyramagnetic ratio is 25182 1/(G s) and for the same dipolar coupling, a ratio of the distances $(r_{P\text{-}CF3})^3/(r_{P\text{-}F})^3$ can be determined. The effective gyromagnetic ratio for the fluorines in a –CF_3 group for several dipolar couplings was averaged to be 42556+/-2000 1/(G s). Thus, the gyromagetic ratios of the CF_3 to F is 1.69:1 which is about a 39% increase.

Conclusion

$^{31}P\{^{19}F\}$ and $^{31}P\{^{19}F_3\}$ REDOR experiments were performed on small model compounds and nucleic acid oligomers. With replacement of a -CF_3 group for –F, the behavior of ^{31}P-^{19}F dephasing was studied. The experimental distances ascertained by $^{31}P\{^{19}F\}$ REDOR for the model compounds, **1-4**, ranged from half to one Angstrom less than the distance calculated from the minimized structure. There was inadequate dilution of the spins and the hindrance was most likely due to the nature of the size of the compound in relation to the distance being measured causing intermolecular effects as well as possible aggregation of the fluorine atoms. The moderate distances measured in the double-stranded 12mer DNA molecules were self-diluting and thus, the experimental distances were in good agreement with the X-ray crystal structure.

Regardless of the intermolecular effects, in all sets of molecules, samples with a -CF_3 group consistently exhibited more dephasing than the -F sample

counterpart. This increase in dephasing indicates that a $-CF_3$ group is a more sensitive measure than a single fluorine, and more accurate distance measurements can be assessed at a shorter dephasing time for distances greater than 12 ′, which can be important when studying large biomolecules or biological complexes.

In summary, long-distance constraints of at most 20 Å are theoretically measureable with the $^{31}P\{^{19}F\}$ REDOR technique in nucleic acids by incorporation of a $-CF_3$ group and slight modification of the phosphate backbone with one phosphorothioate.

Acknowledgment

We thank M.E. Merritt for helpful discussions; J. Schaefer and his group members for P-CF_3 REDOR simulations, helpful discussions, and comments; T.E. Edwards, J. D. Wellhausen, J. C. Markley, and D. Sologub for synthesizing and purifying the DNA; N A. Oyler for the use of his Matlab code for the NMR data workup and the C++ code for the P-F REDOR simulations; James Gibson for reading repeated revisions of the manuscript. This research was supported by the National Institute of Health grant.

References

[1] J.B. Chaires, Drug-DNA interactions, Current Opinion In Structural Biology, 8 (1998) 314-320.

[2] P.B. Dervan, Molecular recognition of DNA by small molecules, Bioorganic & Medicinal Chemistry, 9 (2001) 2215-2235.

[3] S. Neidle, DNA minor-groove recognition by small molecules, Natural Product Reports, 18 (2001) 291-309.

[4] A.L. Lehninger, D.L. Nelso, M.M. Cox, Principles of Biochemistry, (1993).

[5] T.E. Creighton Proteins: Structures and Molecular Properties, Second ed.; W.H. Freeman and Company: New York, 1984.

[6] B.D. Ratner, A.S. Hoffman, F.J. Schoen, J.E. Lemons Biomaterial Science: An Introduction to Materials in Medicine; Elsevier: San Francisco, 2004.

[7] R.R. Sniden, DNA Structure and Function, (1994).

[8] F. Bloch, W.W. Hansen, M. Packard, Phys. Rev., 69 (1946) 37.

[9] E.M. Purcell, H.C. Torrey, R.V. Pound, Phys. Rev., 69 (1946).

[10] D.M. Grant and R.K. Harris Encyclopedia of Nuclear Magnetic Resonance; John Wiley, and Sons: New York; Vol. 1.

[11] E.R. Andrew, A. Bradbury, R.G. Eades, Nature (London), 182 (1958) 1659.

[12] I. Lowe, Phys. Rev. Lett., Phys. Rev. Lett., 2 (1959) 285.

[13] E.O. Stejskal, J. Schaefer, J.S. Waugh, Magic-Angle Spinning And Polarization Transfer In Proton-Enhanced Nmr, Journal Of Magnetic Resonance, 28 (1977) 105-112.

[14] T. Gullion, Introduction to rotational-echo, double-resonance NMR, Concepts In Magnetic Resonance, 10 (1998) 277-289.

[15] G.P. Drobny, J.R. Long, T. Karlsson, W. Shaw, J. Popham, N. Oyler, P. Bower, J. Stringer, D. Gregory, M. Mehta, P.S. Stayton, Structural studies of biomaterials using double-quantum solid-state NMR spectroscopy, Annual Review Of Physical Chemistry, 54 (2003) 531-571.

[16] T. Gullion and J. Schaefer, Rotational-Echo Double-Resonance Nmr, J. Magn. Reson., 81 (1989) 196-200.

[17] T. Gullion and J. Schaefer, Detection of Weak Heteronuclear Dipolar Coupling by Rotational-Echo Double-Resonance Nuclear Magnetic Resonance, Advances in Magnetic Resonance, 13 (1989) 57-83.

[18] T. Gullion and J. Schaefer, Elimination Of Resonance Offset Effects In Rotational-Echo, Double-Resonance Nmr, Journal Of Magnetic Resonance, 92 (1991) 439-442.

[19] J.R. Garbow and T. Gullion, Improvements In Redor Nmr-Spectroscopy - Minimizing Resonance-Offset Effects, J. Magn. Reson., 95 (1991) 442-445.

[20] J.M. Goetz and J. Schaefer, REDOR dephasing by multiple spins in the presence of molecular motion, J. Magn. Reson., 127 (1997) 147-154.

[21] M.L. Gilchrist, K. Monde, Y. Tomita, T. Iwashita, K. Nakanishi, A.E. McDermott, Measurement of Interfluorine Distances in Solids, J. Magn. Reson., 152 (2001) 1-6.

[22] R.W. Glaser, C. Sachse, U.H.N. Durr, P. Wadhwani, A.S. Ulrich, Orientation of the antimicrobial peptide PGLa in lipid membranes determined from F-19-NMR dipolar couplings of 4-CF3-phenylglycine labels, Journal Of Magnetic Resonance, 168 (2004) 153-163.

[23] D.M. Gregory, D.J. Mitchell, J.A. Stringer, S. Kiihne, J.C. Shiels, J. Callahan, M.A. Mehta, G.P. Drobny, Windowless Dipolar Recoupling - The Detection Of Weak Dipolar Couplings Between Spin-1/2 Nuclei With Large Chemical-Shift Anisotropies, Chemical Physics Letters, 246 (1995) 654-663.

[24] P.V. Bower, N. Oyler, M.A. Mehta, J.R. Long, P.S. Stayton, G.P. Drobny, Determination of torsion angles in proteins and peptides using solid state NMR, Journal Of The American Chemical Society, 121 (1999) 8373-8375.

[25] P.V. Bower, E.A. Louie, J.R. Long, P.S. Stayton, G.P. Drobny, Solid-state NMR structural studies of peptides immobilized on gold nanoparticles, Langmuir, 21 (2005) 3002-3007.

[26] M. Gilbert, W.J. Shaw, J.R. Long, K. Nelson, G.P. Drobny, C.M. Giachelli, P.S. Stayton, Chimeric peptides of statherin and osteopontin that bind hydroxyapatite and mediate cell adhesion, Journal Of Biological Chemistry, 275 (2000) 16213-16218.

[27] T. Karlsson, J.M. Popham, J.R. Long, N. Oyler, G.P. Drobny, A study of homonuclear dipolar recoupling pulse sequences in solid-state nuclear magnetic resonance, Journal Of The American Chemical Society, 125 (2003) 7394-7407.

[28] J.R. Long, J.L. Dindot, H. Zebroski, S. Kiihne, R.H. Clark, A.A. Campbell, P.S. Stayton, G.P. Drobny, A peptide that inhibits hydroxyapatite growth is in an extended conformation on the crystal surface, Proceedings Of The National Academy Of Sciences Of The United States Of America, 95 (1998) 12083-12087.

[29] J.R. Long, N. Oyler, G.P. Drobny, P.S. Stayton, Assembly of alpha-helical peptide coatings on hydrophobic surfaces, Journal Of The American Chemical Society, 124 (2002) 6297-6303.

[30] J.R. Long, W.J. Shaw, P.S. Stayton, G.P. Drobny, Structure and dynamics of hydrated statherin on hydroxyapatite as determined by solid-state NMR, Biochemistry, 40 (2001) 15451-15455.

[31] D.M. Gregory The design of new solid-state NMR experiments for use in determining oligonucleotide structure / by David Matthew Gregory, 1996.

[32] N. Oyler. SSNMR methods for determining structure in nucleosides and peptides / Nathan Andrew Oyler, University of Washington, 2000.

[33] S.L. Beaucage and R.P. Iyer, The Functionalization Of Oligonucleotides Via Phosphoramidite Derivatives, Tetrahedron, 49 (1993) 1925-1963.

[34] J.C. Markley, P. Chirakul, D. Sologub, S.T. Sigurdsson, Incorporation of 2 '-deoxy-5-(trifluoromethyl)uridine and 5-cyano-2 '-deoxyuridine into DNA, Bioorganic & Medicinal Chemistry Letters, 11 (2001) 2453-2455.

[35] T.M. Alam and G.P. Drobny, Solid-State Nmr-Studies Of Dna-Structure And Dynamics, Chemical Reviews, 91 (1991) 1545-1590.

[36] J.A. Stringer and G.P. Drobny, Methods for the analysis and design of a solid state nuclear magnetic resonance probe, Rev. Sci. Instrum., 69 (1998) 3384-3391.

[37] J.A. Stringer. The Design and Analysis of Solid State Nuclear Magnetic Resonance Probes for the Determination of Biomolecular Structure, University of Washington, 1998.

[38] J. Gladden and G.P. Drobny. Unpublished work.

[39] C.G. Fields, P.V. Lograsso, T.A. Cross, Solid-Phase Synthesis And Solid-State N-15 Nmr-Spectroscopy Of Gramicidin-A, Gramicidin-B, And Gramicidin-C, Faseb Journal, 2 (1988) A320-A320.

[40] G.B. Fields, C.G. Fields, J. Petefish, H.E. Vanwart, T.A. Cross, Solid-Phase Peptide-Synthesis And Solid-State Nmr-Spectroscopy Of [Ala3-N-15][Val1]Gramicidin-A, Proceedings Of The National Academy Of Sciences Of The United States Of America, 85 (1988) 1384-1388.

[41] K. *Eichele* and R.E. *Wasylishen. HBA ver. 1.4*; *Dalhousie University, 2001.*

[42] L.M. McDowell, A. Schmidt, E.R. Cohen, D.R. Studelska, J. Schaefer, Structural constraints on the ternary complex of 5-enolpyruvylshikimate-3-phosphate synthase from rotational-echo double-resonance NMR, J. Mol. Biol., 256 (1996) 160-171.

[43] D.R. Studelska, C.A. Klug, D.D. Beusen, L.M. McDowell, J. Schaefer, Long-range distance measurements of protein binding sites by rotational-echo double-resonance NMR, J. Am. Chem. Soc., 118 (1996) 5476-5477.

[44] M.E. Merritt, S.T. Sigurdsson, G.P. Drobny, Long-range distance measurements to the phosphodiester backbone of solid nucleic acids using P-31-F-19 REDOR NMR, J. Am. Chem. Soc., 121 (1999) 6070-6071.

[45] G.L. Olsen, E.A. Louie, G.P. Drobny, S.T. Sigurdsson, Determination of DNA minor groove width in distamycin-DNA complexes by solid-state NMR, Nucleic Acids Res., 31 (2003) 5084-5089.

[46] W.S. Enochs, W.B. Hyslop, H.F. Bennett, R.D. Brown, S.H. Koenig, H.M. Swartz, Sources Of The Increased Longitudinal Relaxation Rates Observed In Melanotic Melanoma - An Invitro Study Of Synthetic Melanins, Investigative Radiology, 24 (1989) 794-804.

[47] H.M. Berman, Westbrook, J., Feng, Z., Gilliland, G., Bhat, T. N., Weissig, H., Shindyalov, I. N., Bourne, P. E., The Protein Data Bank, Nucleic Acids Research, 28 (2000) 235-242.

[48] O.V. Grineva and P.M. Zorkii, Isostructural and nonisostructural compounds in series of halogenated organic crystal substances. Structure of Hal-aggregates, Journal Of Structural Chemistry, 42 (2001) 16-23.

[49] O.V. Grineva and P.M. Zorkii, Aggregation of halogen atoms in crystalline isomers, Journal Of Structural Chemistry, 43 (2002) 995-1005.

[50] O.V. Grineva and P.M. Zorkii, Aggregation of halogen atoms in haloorganic crystals with low halogen contents, Russian Journal Of Physical Chemistry, 74 (2000) 1758-1764.

[51] W.R. Veatch and E.R. Blout, Aggregation Of Gramicidin-A In Solution, Biochemistry, 13 (1974) 5257-5264.

[52] J.A. Killian, K.U. Prasad, D. Hains, D.W. Urry, The Membrane As An Environment Of Minimal Interconversion - A Circular-Dichroism Study On The Solvent Dependence Of The Conformational Behavior Of Gramicidin In Diacylphosphatidylcholine Model Membranes, Biochemistry, 27 (1988) 4848-4855.

[53] B.A. Wallace and K. Ravikumar, The Gramicidin Pore - Crystal-Structure Of A Cesium Complex, Science, 241 (1988) 182-187.

[54] S.M. Pascal and T.A. Cross, High-Resolution Structure And Dynamic Implications For A Double-Helical Gramicidin-A Conformer, Journal Of Biomolecular Nmr, 3 (1993) 495-513.

[55] Z.L. Zhang, S.M. Pascal, T.A. Cross, A Conformational Rearrangement In Gramicidin-A - From A Double-Stranded Left-Handed To A Single-Stranded Right-Handed Helix, Biochemistry, 31 (1992) 8822-8828.

[56] S.M. Pascal and T.A. Cross, Structure Of An Isolated Gramicidin-A Double Helical Species By High-Resolution Nuclear-Magnetic-Resonance, Journal Of Molecular Biology, 226 (1992) 1101-1109.

[57] Y. Chen, A. Tucker, B.A. Wallace, Solution structure of a parallel left-handed double-helical gramicidin-A determined by 2D H-1 NMR, Journal Of Molecular Biology, 264 (1996) 757-769.

[58] A.W. Hing and J. Schaefer, 2-Dimensional Rotational-Echo Double-Resonance Of Val1-[1-C-13]Gly2-[N-15]Ala3-Gramicidin-A In Multilamellar Dimyristoylphosphatidylcholine Dispersions, Biochemistry, 32 (1993) 7593-7604.

[59] T.A. Cross, Solid-State Nuclear-Magnetic-Resonance Approach For Determining The Structure Of Gramicidin A Without Model-Fitting, Biophysical Journal, 49 (1986) 124-126.

[60] L.K. Nicholson, F. Moll, T.E. Mixon, P.V. Lograsso, J.C. Lay, T.A. Cross, Solid-State N-15 Nmr Of Oriented Lipid Bilayer Bound Gramicidin A', Biochemistry, 26 (1987) 6621-6626.

[61] F. Moll, L.K. Nicholson, P.V. Lograsso, J.C. Lay, C.A. Guy, J. Petefish, G.B. Fields, H.E. Vanwart, T.A. Cross, Solid-State N-15 Nmr-Studies Of Uniform And Specific Site N-15 Labeled Gramicidin-A' In An Oriented Lipid Bilayer, Biophysical Journal, 51 (1987) A73-A73.

[62] J.A. Killian, L.K. Nicholson, T.A. Cross, Solid-State N-15-Nmr Evidence That Gramicidin-A Can Adopt 2 Different Backbone Conformations In Dimyristoylphosphatidylcholine Model Membrane Preparations, Biochimica Et Biophysica Acta, 943 (1988) 535-540.

[63] Q. Teng, S.M. Pascal, T.A. Cross, Determination Of Torsion Angles In The Backbone Of The Gramicidin Cation Channel By Solid-State Nmr, Biophysical Journal, 57 (1990) A100-A100.

[64] S.W. Chiu, L.K. Nicholson, M.T. Brenneman, S. Subramaniam, Q. Teng, C. North, J.A. McCammon, T.A. Cross, E. Jakobsson, Molecular-Dynamics Computations And Solid-State Nmr Of The Gramicidin Cation Channel, Biophysical Journal, 57 (1990) A101-A101.

[65] R.R. Ketchem, W. Hu, T.A. Cross, Structural Details Of The Gramicidin Channel Conformation By Solid-State Nmr, Faseb Journal, 6 (1992) A526-A526.

[66] R.R. Ketchem, W. Hu, T.A. Cross, High-Resolution Conformation Of Gramicidin-A In A Lipid Bilayer By Solid-State Nmr, Science, 261 (1993) 1457-1460.

[67] S.L. Grage, J.F. Wang, T.A. Cross, A.S. Ulrich, Solid-state F-19-NMR analysis of F-19-labeled tryptophan in gramicidin A in oriented membranes, Biophysical Journal, 83 (2002) 3336-3350.

[68] G.J. Gallagher, M. Hong, L.K. Thompson, Solid-state NMR spin diffusion for measurement of membrane-bound peptide structure: Gramicidin A, Biochemistry, 43 (2004) 7899-7906.

[69] W.R. Veatch, E.T. Fossel, E.R. Blout, Conformation Of Gramicidin-A, Biochemistry, 13 (1974) 5249-5256.

[70] D.W. Urry, D.F. Mayers, J.D. Glickson, J. Haider, Spectroscopic Studies On Conformation Of Gramicidin-A' - Evidence For A New Helical Conformation, Biochemistry, 11 (1972) 487-&.

[71] J.D. Glickson, D.F. Mayers, D.W. Urry, J.M. Settine, Spectroscopic Studies On Conformation Of Gramicidin A' - Proton Magnetic-Resonance Assignments, Coupling-Constants, And H-D Exchange, Biochemistry, 11 (1972) 477-&.

[72] V.F. Bystrov, A.S. Arseniev, I.L. Barsukov, A.P. Golovanov, I.V. Maslennikov, The Structure Of The Transmembrane Channel Of Gramicidin A - Nmr-Study Of Its Conformational Stability And Interaction With Divalent-Cations, Gazzetta Chimica Italiana, 120 (1990) 485-491.

[73] W.F. Degrado and J.D. Lear, Induction Of Peptide Conformation At Apolar Water Interfaces.1. A Study With Model Peptides Of Defined Hydrophobic Periodicity, Journal Of The American Chemical Society, 107 (1985) 7684-7689.

[74] R.R. Ketchem, K.C. Lee, S. Huo, T.A. Cross, Macromolecular structural elucidation with solid-state NMR-derived orientational constraints, Journal Of Biomolecular Nmr, 8 (1996) 1-14.

[75] B.M. Burkhart, N. Li, D.A. Langs, W.A. Pangborn, W.L. Duax, The conducting form of gramicidin A is a right handed double-stranded double helix, Proceedings Of The National Academy Of Sciences Of The United States Of America, 95 (1998) 12950-12955.

[76] R.R. Ketchem, B. Roux, T.A. Cross, High-resolution polypeptide structure in a lamellar phase lipid environment from solid state NMR derived orientational constraints, Structure, 5 (1997) 1655-1669.

[77] L.M. McDowell, D.R. Studelska, B. Poliks, R.D. O'Connor, J. Schaefer, Characterization of the complex of a trifluoromethyl-substituted shikimate-based bisubstrate inhibitor and 5-enolpyruvylshikimate-3-phosphate synthase by REDOR NMR, Biochemistry, 43 (2004) 6606-6611.

[78] W.H. Gmeiner, R.T. Pon, J.W. Lown, Synthesis, Annealing Properties, F-19 Nmr Characterization, And Detection Limits Of A Trifluorothymidine-Labeled Antisense Oligodeoxyribonucleotide 21-Mer, J. Org. Chem., 56 (1991) 3602-3608.

[79] P.D. Cook and Y.S. Sanghvi. US Patent 5,614,617, 1992; *Chem. Abstr.* **1992**, 117, 111996., 1992.

[80] A.K. Mehta, D.J. Hirsh, N. Oyler, G.P. Drobny, J. Schaefer, Carbon-proton dipolar decoupling in REDOR, J. Magn. Reson., 145 (2000) 156-158.

[81] F.G. Vogt, J.M. Gibson, S.M. Mattingly, K.T. Mueller, Determination of molecular geometry in solid-state NMR: Rotational-echo double resonance of three-spin systems, Journal Of Physical Chemistry B, 107 (2003) 1272-1283.

[82] T. Gullion, D.B. Baker, M.S. Conradi, New Compensated Carr-Purcell Sequences, J. Magn. Reson., 89 (1990) 479-484.

[83] Y. Pan, P-31-F-19 Rotational-Echo, Double-Resonance Nuclear-Magnetic-Resonance Experiment On Fluoridated Hydroxyapatite, Solid State Nuclear Magnetic Resonance, 5 (1995) 263-268.

[84] P.R. Bevington and D.K. Robinson, Data Reduction and Error Analysis for the Physical Sciences, (1992).

[85] M. Bak, J.T. Rasmussen, N.C. Nielsen, SIMPSON: A general simulation program for solid-state NMR spectroscopy, J. Magn. Reson., 147 (2000) 296-330.

[86] A.D. Digabriele, M.R. Sanderson, T.A. Steitz, Crystal-Lattice Packing Is Important In Determining The Bend Of A Dna Dodecamer Containing An Adenine Tract, Proc. Natl. Acad. Sci. U. S. A., 86 (1989) 1816-1820.

[87] A.K. Mehta and J. Schaefer, Rotational-echo double resonance of uniformly labeled C-13 clusters, J. Magn. Reson., 163 (2003) 188-191.

List of Tables

Table 1 Comparison of distances measured of **1-6** by X-ray crystal structures and $^{31}P\{^{19}F\}$REDOR. The distance between ^{31}P-^{19}F/$^{19}F_3$ of compounds **1-4** and molecules **5** and **6** were measured using ^{31}P-^{19}F REDOR without and with dilution. Fragments of crystal structures found in the Cambride Structural Database (CSD) to be similar to compounds **1-4** are shown with their corresponding CSD code. The crystal structure for molecules **5** and **6** was found in the Protein Data Bank (PDB). The dots in the structures represent the placement of the ^{31}P and ^{19}F or center of mass of the CF_3 group. The distance from the crystal structures were tabulated. The DNA samples were hydrated and in B-form. W represents the hydration amount and is equivalent to the number of water molecules per nucleotide

Table 2 A comparison of the percent dephasing of P-F and P-CF_3 at 30 ms evolution.

List of Figures

Figure 1. Compounds and molecules (**1-6**) with unique phosphorous and -F or -CF_3 group, used in this study where the distance between the phosphorous atom and -F or -CF_3 were measured by $^{31}P\{^{19}F\}$ REDOR.

Figure 2. Synthetic pathway of compounds **1-4**.

Figure 3. The XY8-REDOR pulse sequence for measuring ^{31}P-^{19}F dipolar couplings. **A)** The S_o (full echo) experiment shows that following cross

polarization (CP) from ^{1}H to ^{31}P, the phosphorus signal is refocused by a series of π pulses following the XY8 phase cycling. **B)** On alternate scans, the S (reduced echo) experiment is collected. The ^{19}F π pulses are used to recouple the fluorine to the phosphorous nuclei. N is the number of XY8 cycles.

Figure 4. The orientation of the $-CF_3$ group with respect to the phosphorous atom. **A)** The P-CF_3 0° orientation is defined as the phosphorous atom being along the C3 axis of the $-CF_3$ goup. **B)** The P-CF_3 90° orientation is defined as the phosphorous atom being in the plane of the three fluorines.

Figure 5. $^{31}P\{^{19}F\}$ REDOR dephasing curves for P-F and P-CF_3 simulations at 6, 9, and 12 Å. Dashed lines P-CF_3 90°; dotted line P-CF_3 0°; and solid line P-F. The dephasing curve is the ratio of the S and So experiments as a function of NcTr which is the number of rotor cycles(Nc) multiplied by the rotor period (Tr).

Figure 6. Comparison of P-F and P-CF_3 distances for a range of coupling constants. As the coupling constant decreases, the difference in distance measureable between the P-F (solid triangles) and P-CF_3 (solid squares) increases to a maximum of 5 Å. Solid diamond shows difference in distance between P-F and P-CF_3.

Figure 7. A) REDOR So (full echo) spectrum with 8 rotor cycles of evolution for compound **4** undiluted spinning at 4kHz, 2048 scans. **B)** REDOR So (full echo) spectrum with 8 rotor cycles of evolution for compound **4** spinning at 5 kHz diluted 1:40 mol/mol benzoic acid.

Figure 8. Overlay of $^{31}P\{^{19}F\}$ Redor dephasing curves of samples with -F and $-CF_3$ and simulations. **A)** Experimental data for molecules **1** (filled circles) and **2** (filled squares). Both samples were diluted with KBr (1:100). The lines are simulated REDOR curves where the solid line is P-F at 6 Å, short dashed lines are P-CF_3 at 6 Å 0°, long dashed lines are P-CF_3 at 6 Å 90°. **B)** Experimental

data for molecules **3** (filled circles) diluted 1:40 in benzoic acid and **4** (filled squares) diluted 10 mg/60 μL in H_2O. The lines are simulated REDOR curves, solid line is P-F at 9 Å , short dashed lines are P-CF_3 at 9Å 90°, and long dashed lines are P-CF_3 at 8 Å 90°.

Figure 9. A) Experimental data for compound **3** undiluted (solid squares) and diluted (solid-circles) in distilled water at 10mg/60μL. The lines are simulated REDOR curves for P-F at 7, 8 and 9Å. **B)** Experimental data for compound **4** undiluted (solid triangles) and diluted (solid-diamonds) in 1:40 mol/mol benzoic acid. The lines are simulated REDOR curves for P-CF_3 90° at 8, 9 and 10Å.

Figure 10. Multi-spin model, simulations, and dephasing curves. **A)** Model for multi-spin simulation of **1** where the ^{19}F atom is coupled to ^{31}P at 6.0 Å and 3.5 Å. **B)** Experimental data for **1** (solid square) diluted with KBr (1:100). The dashed line represents the best fit to a linear combination of two spin (90% 6 Å) and three spin simulations (10% of 6 Å and 3.5 Å). Experimental data for **2** (solid triangle) diluted with KBr (1:100). The best fit simulation considered a -CF_3 at a distance of 5.34 Å. **C)** Experimental data for **3** (solid circle) diluted 10 mg/30 μL in H_2O. The curve was fit to a linear combination of two REDOR effects, one due to a single spin at 9.8 Å distance contributing 67% and another due to two spins at distances 9.8 Å and 9.0 A respectively, with the 9.0 Å being the distance between the phosphorus and a fluorine from another molecule. Experimental data for **4** (solid diamond) diluted with benzoic acid (1:40). The dashed line represents the best fit to a four spin simulation (89, 93, 122 Hz).

Figure 11. REDOR So (full echo) spectrum with 8 rotor cycles of evolution for 5'd(CGCATT-(pS)-TT$^{5\text{-F}}$UGCG)•d(CGCAAAAATGCG) where $^{5\text{-F}}U$ denotes 2'deoxy-5-fluorouridine and (pS) denotes a phosphorothioate (SPO_3^-) in place of a phosphate (OPO_3^-) group. Magic-angle spinning was performed at 5988 ± 2

Hz. Three sets of 6144 scans were acquired. The spinning side bands are labeled ssb. Inset shows phosphorothioate peak and spinning sideband.

Figure 12. $^{31}P\{^{19}F\}$REDOR dephasing curves for dsDNA **A)** Dots are experimental data for dsDNA with single fluorine (**5**). The lines are simulated ^{31}P-^{19}F dephasing curves: dots 11 Å (34 Hz), solid line 12 Å (26 Hz), and dashed lines 13 Å (21 Hz) **B)** short dashed lines are P-CF_3 at12 Å 0°, long dashed lines are P-CF_3 at 12 Å 90°. **C)** Co-plot of $^{31}P\{^{19}F\}$REDOR dephasing curves for dsDNA **5** (solid circles) and **6** (solid squares) where the DNA with the –CF_3 (**6**) incorporated shows more dephasing than the DNA with a single fluorine (**5**) especially the data points at 20 ms shows the increase in dephasing due to the CF_3 group. CF_3 dephased 60%, CF dephased 35% at 20 ms

Tables

Table 1.

Sample from Figure 1	Measured Distance r_{P-F} (Å)[†]	X-Ray Crystal Structure, Code, and Distance r_{P-F} (Å)
1	6.0 ± 0.9 (1:100 mol/mol KBr) 6.2 ± 1.0 (1:5 mol/mol benzoic acid) 6.0 ± 1.0 (1:20 mol/mol benzoic acid)	HOGDOW[a] 6.66 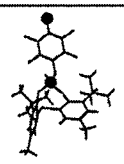
2	6.0 ± 0.8 (1:100 mol/mol KBr)	FIPXIL[b] 7.08 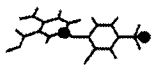
3	9.0 ± 0.9 (undiluted) 9.5 ± 1.1 (10mg/30µL) 9.3 ± 1.8 (10mg/60µL)	WADBEI[c] 10.31* 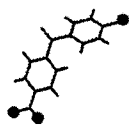
4	8.3 ± 3.7 (undiluted) 9.3 ± 2.7 (1:40 mol/mol benzoic acid)	IBOMUH[d] 11.14* 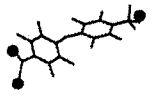
5	12 ± 1 (W=14)	1BDN[e] 11.89 
6	13 ± 2 (W=14)	1BDN[e] 11.16 

[†] Distance measured using $^{31}P\{^{19}F\}$ REDOR
* Distance was averaged due to phosphorous atom could be in either position.
[a] P. Sood, A. Chandrasekaran, R.O. Day, R.R. Holmes, Inorg. Chem (1998) 37, 6329.
[b] C.H. L. Kennard, G. Smith, T. Hari, Aust J. Chem. (1987) 40, 1131.
[c] S. Guo, G. Su, F. Pan, Y. He, Z. Kristallogr. (1992) 202, 296.
[d] T.M. Klapotke, B. Krumm, P. Meyer, H. Piotrowski, Z. Anorg. Allg. Chem. (2001) 627, 1983.
[e] A.D. DiGabriele, M.R. Sanderson, T.A. Steitz, Proc. Natl. Acad. Sci U.S.A. (1989) 86,1816.

Table 2

	Percent Dephasing	
Distance (Å)	P-F	P-CF_3
6	100	100
9	100	100
11	73	80
13	50	60
15	15	35
16	11	26
18	5.5	15
20	3	8
23	1.2	4
27	0.5	1.5
30	0.3	0.8

Figures

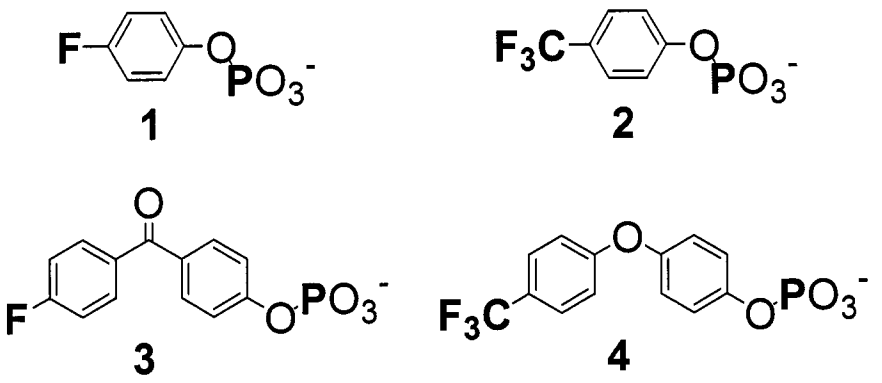

Figure. 1

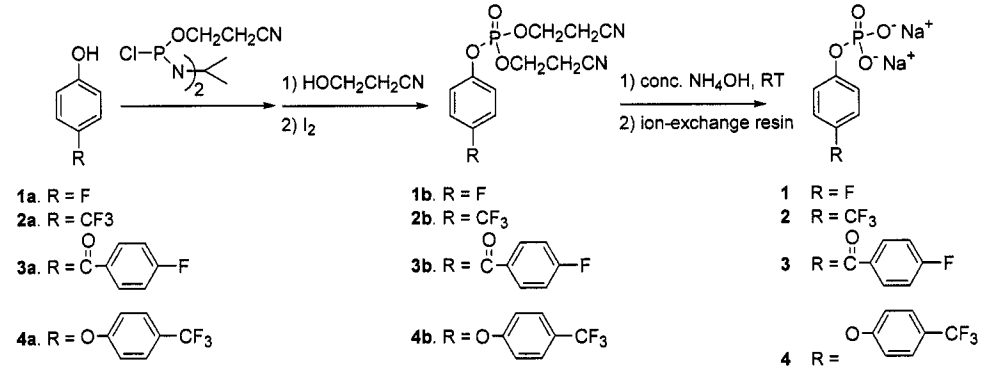

Figure 2.

A) S_o experiment

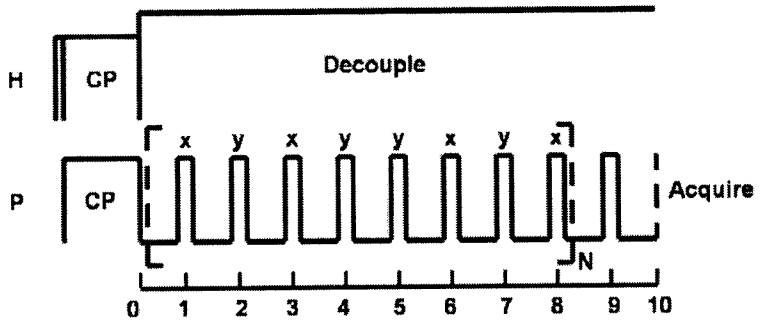

B) S experiment

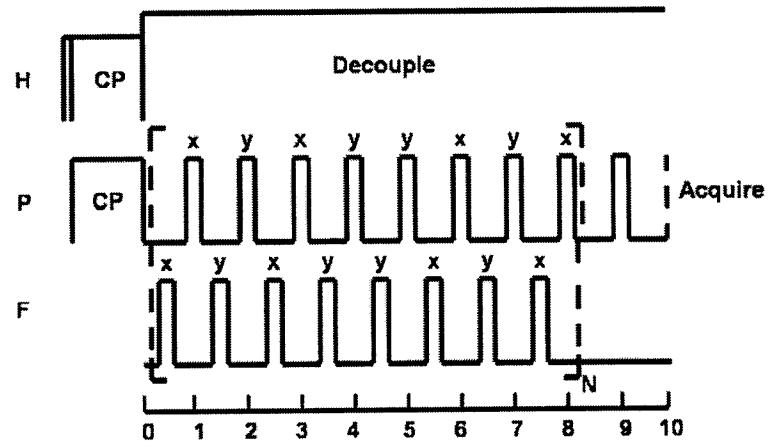

Figure 3.

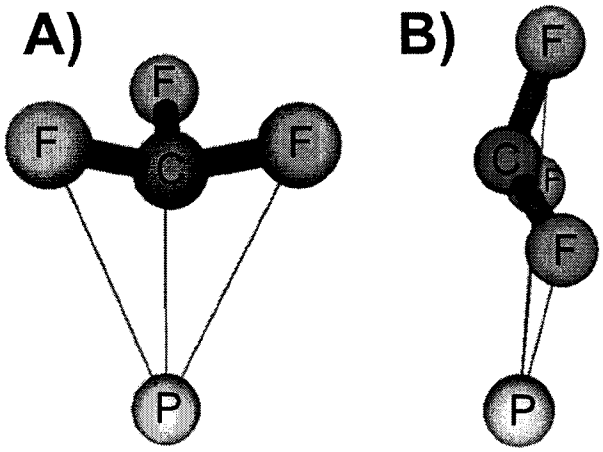

Figure 4.

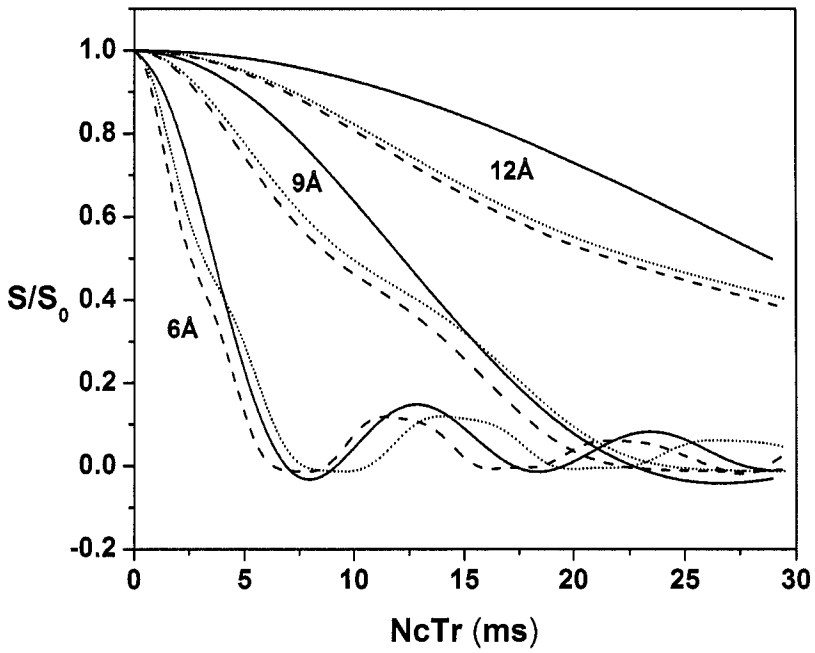

Figure 5

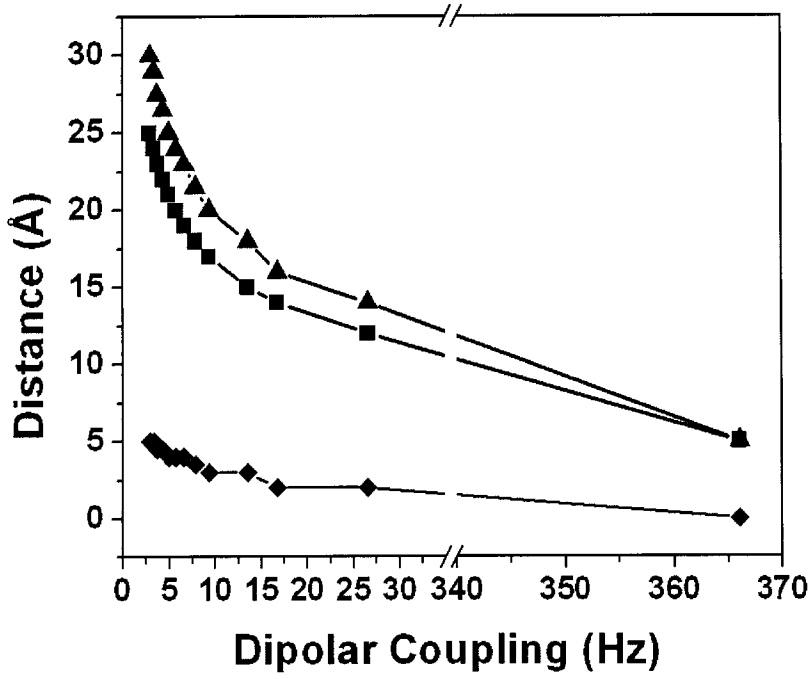
Distance (Å)
30
25
20
15
10
5
0
0 5 10 15 20 25 30 340 350 360 370
Dipolar Coupling (Hz)

Figure 6.

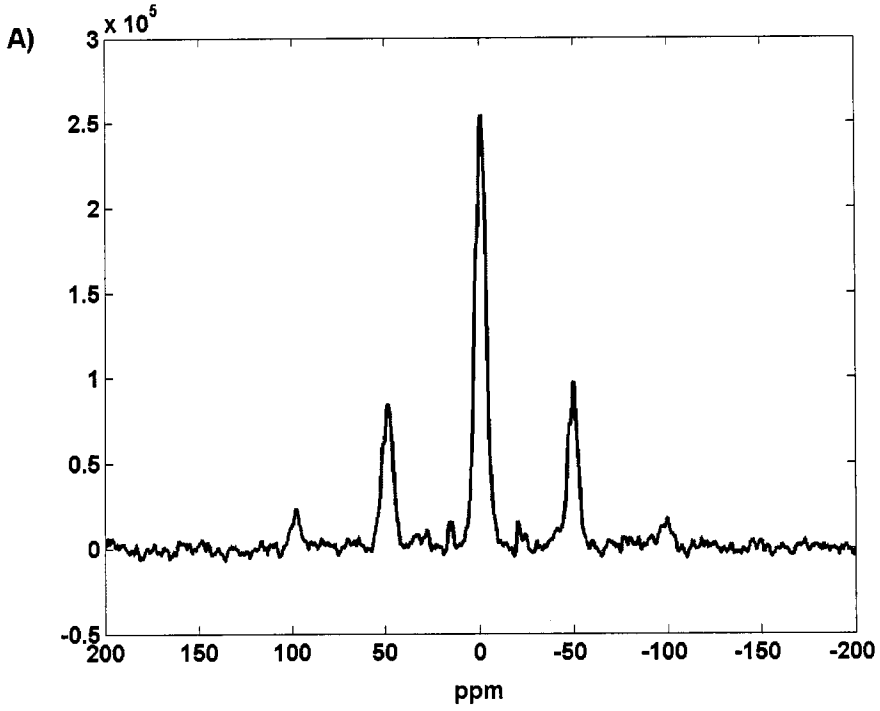

Figure 7A

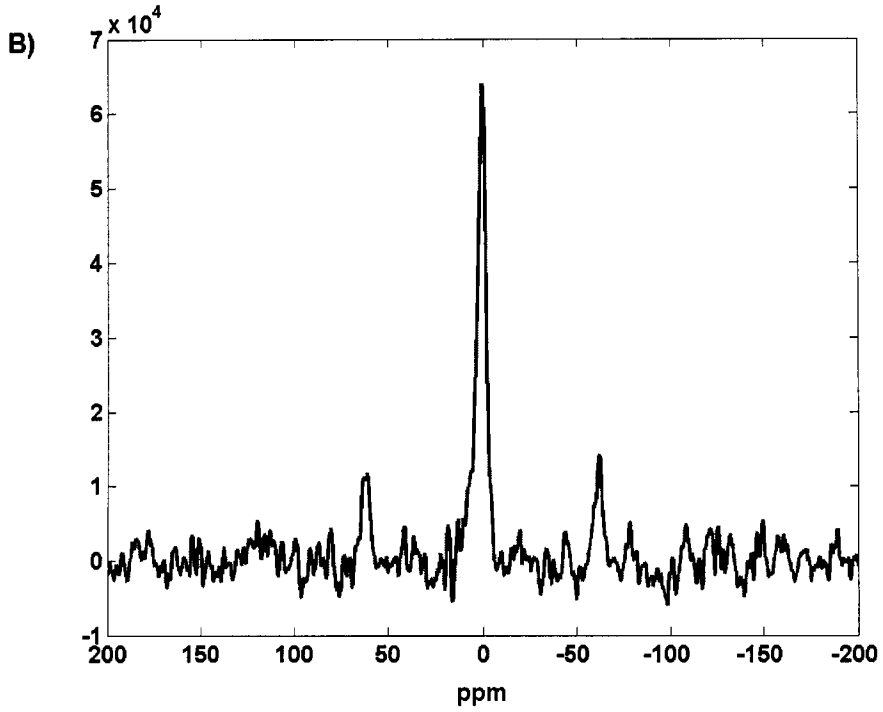

Figure 7B

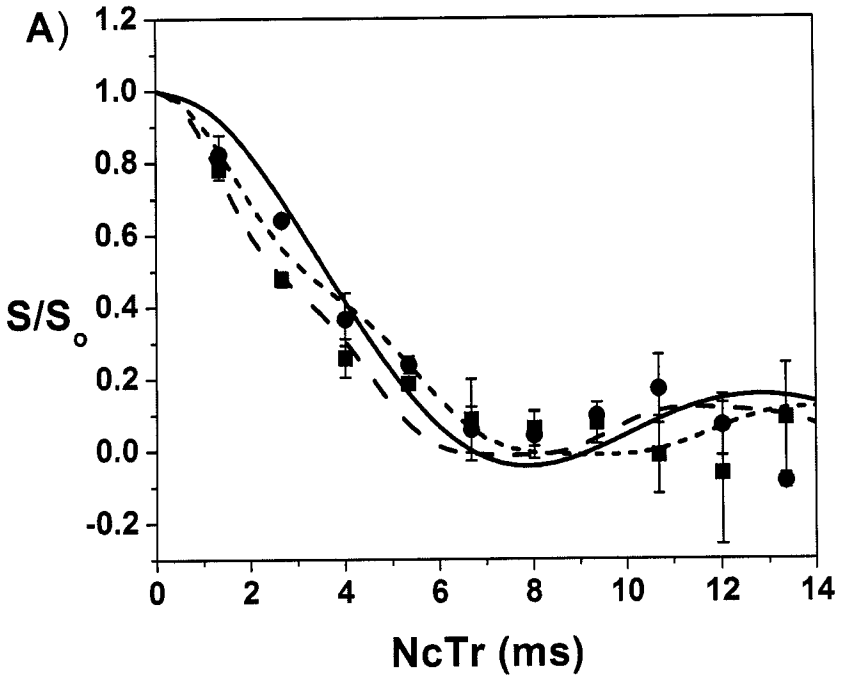

Figure 8A

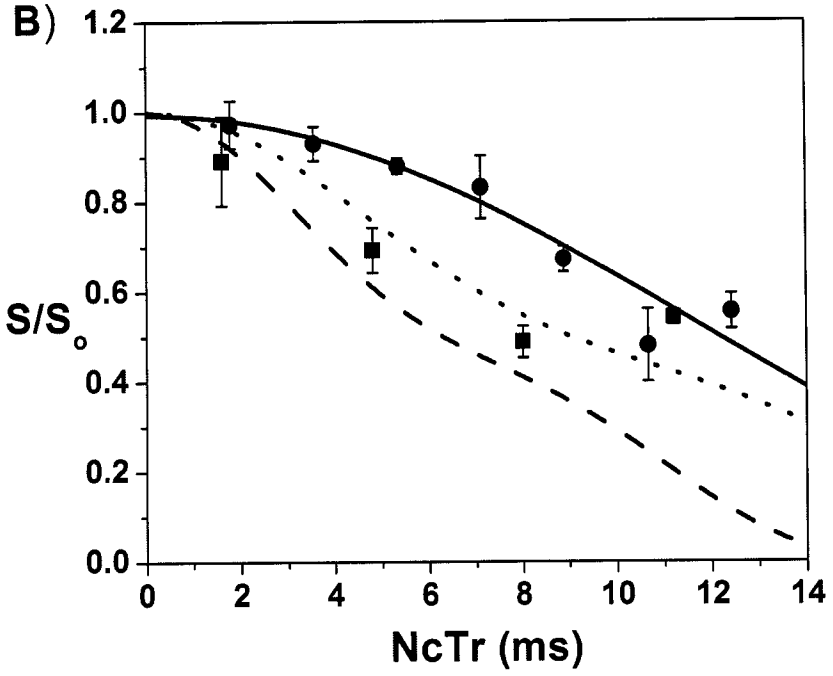

Figure 8B

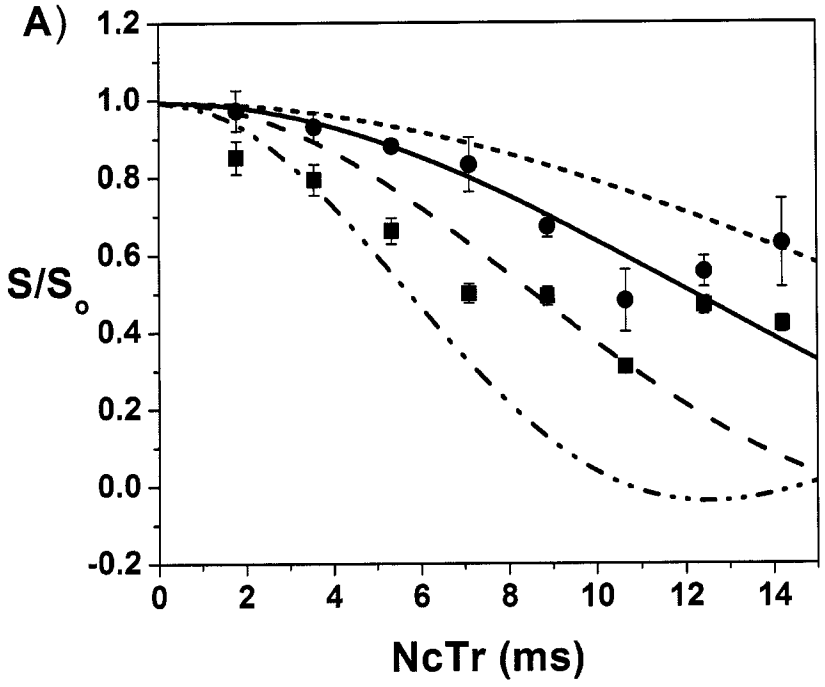

Figure 9A

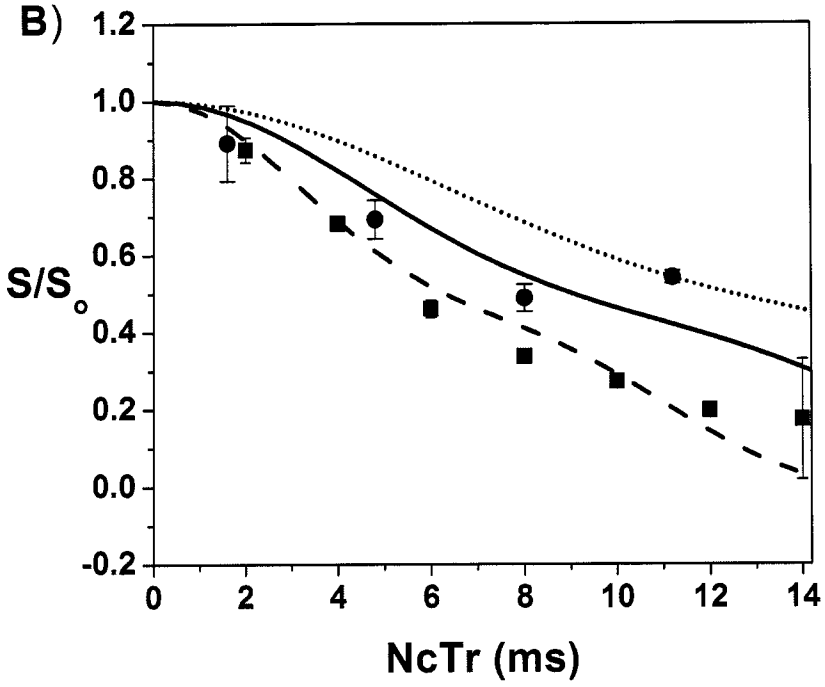

Figure 9B

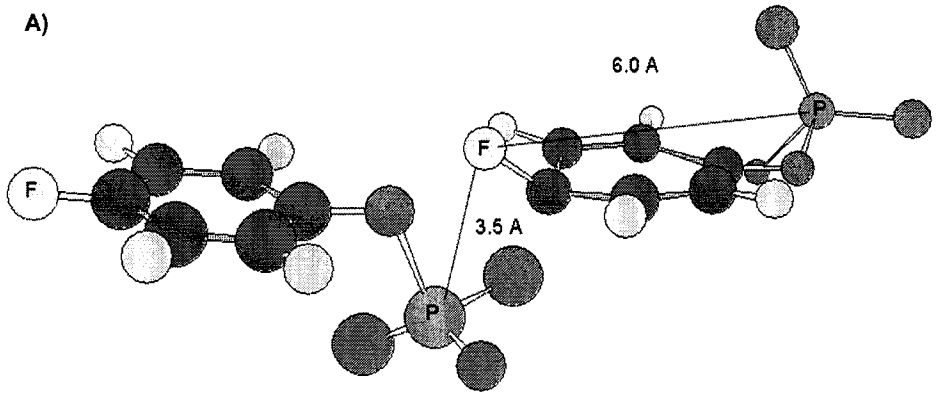

Figure 10A

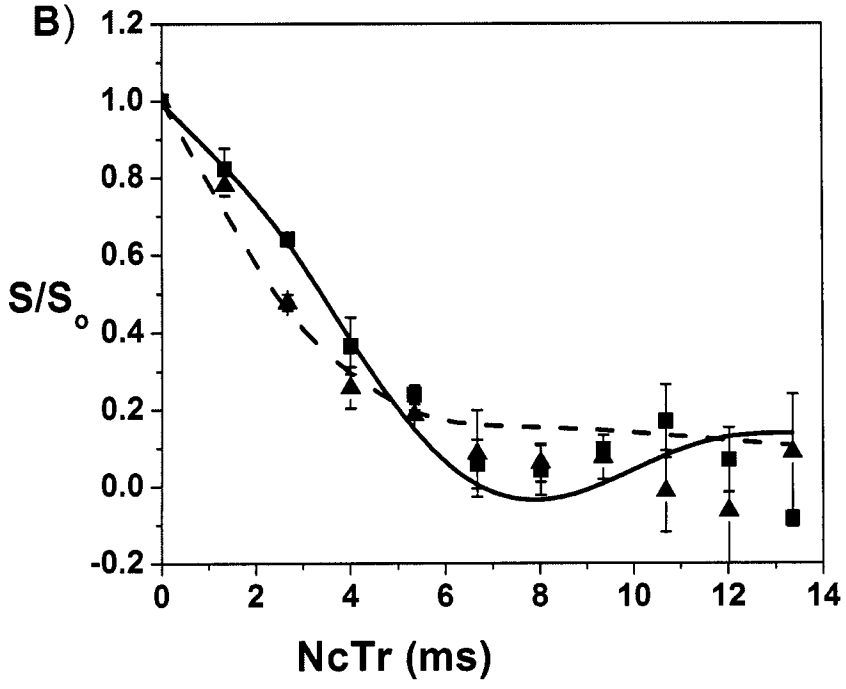

Figure10B

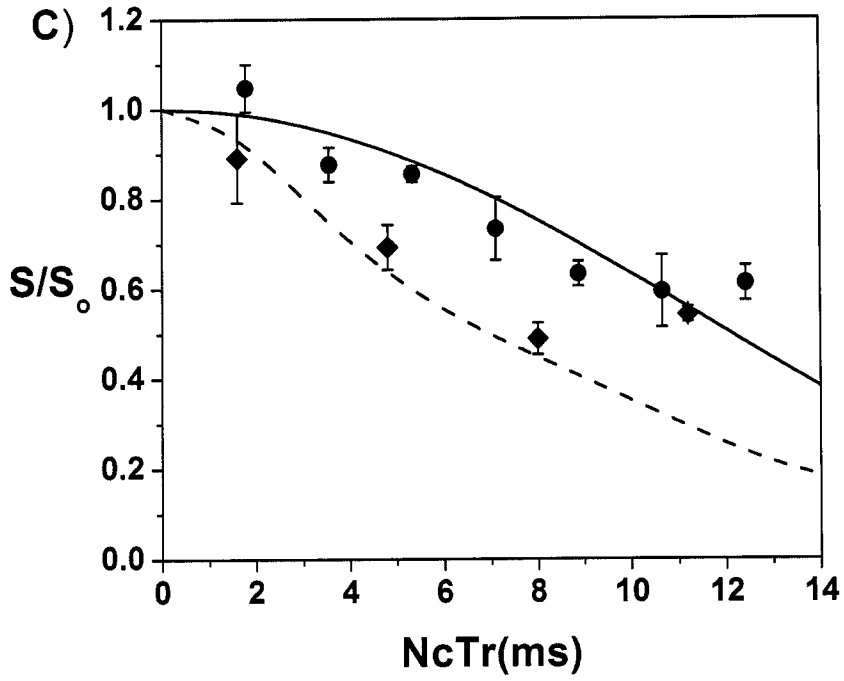

Figure 10C

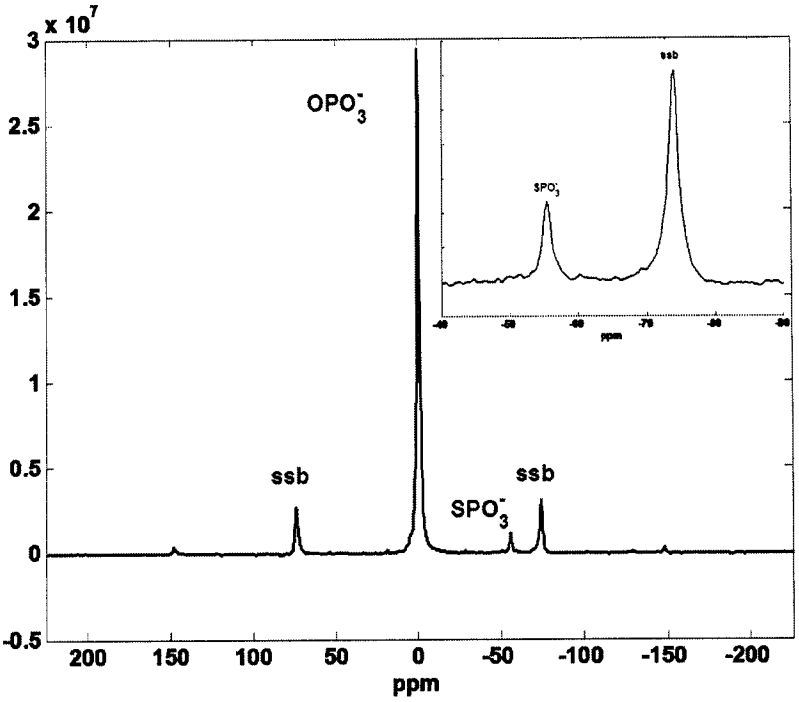
x 10^7
3
2.5
2
1.5
1
0.5
0
-0.5
OPO3-
ssb
SPO3-
ssb
200
150
100
50
0
-50
-100
-150
-200
ppm

Figure 11

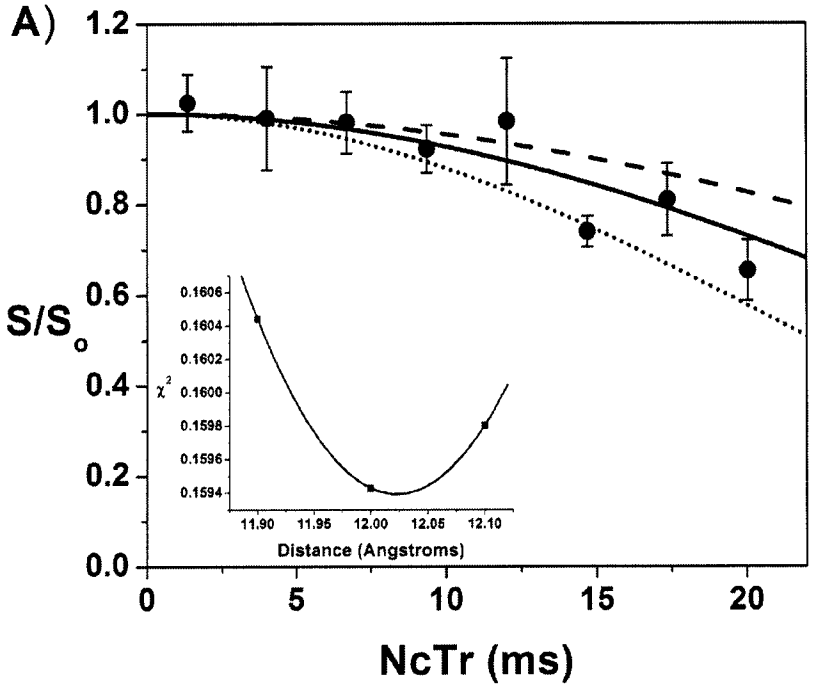
A)
1.2
1.0
0.8
0.6
0.4
0.2
0.0
S/S0
0
5
10
15
20
NcTr (ms)
0.1606
0.1604
0.1602
0.1600
0.1598
0.1596
0.1594
χ2
11.90
11.95
12.00
12.05
12.10
Distance (Angstroms)

Figure 12A

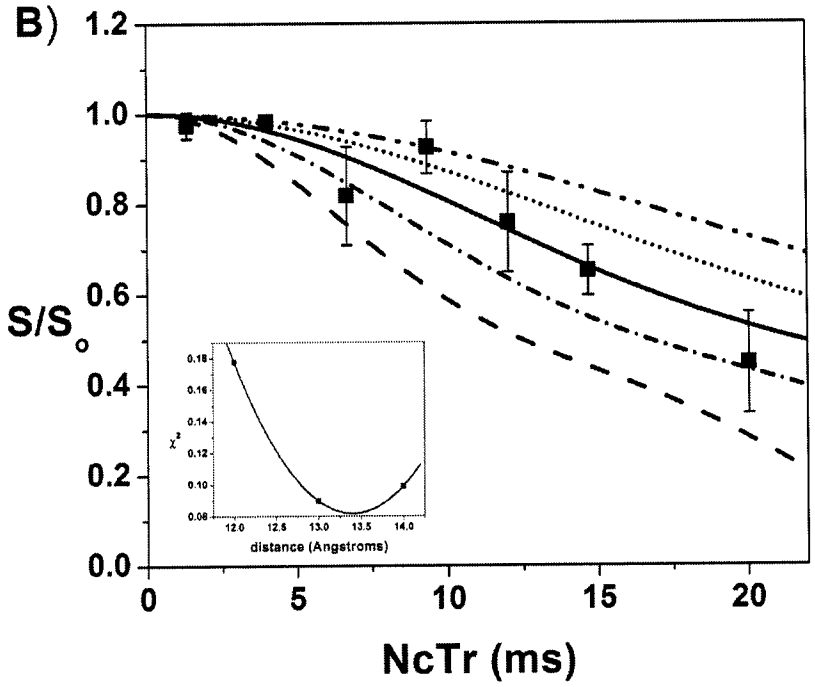
B)
1.2
1.0
0.8
0.6
0.4
0.2
0.0
S/S$_o$
0
5
10
15
20
NcTr (ms)
χ^2
0.18
0.16
0.14
0.12
0.10
0.08
12.0
12.5
13.0
13.5
14.0
distance (Angstroms)

Figure 12B

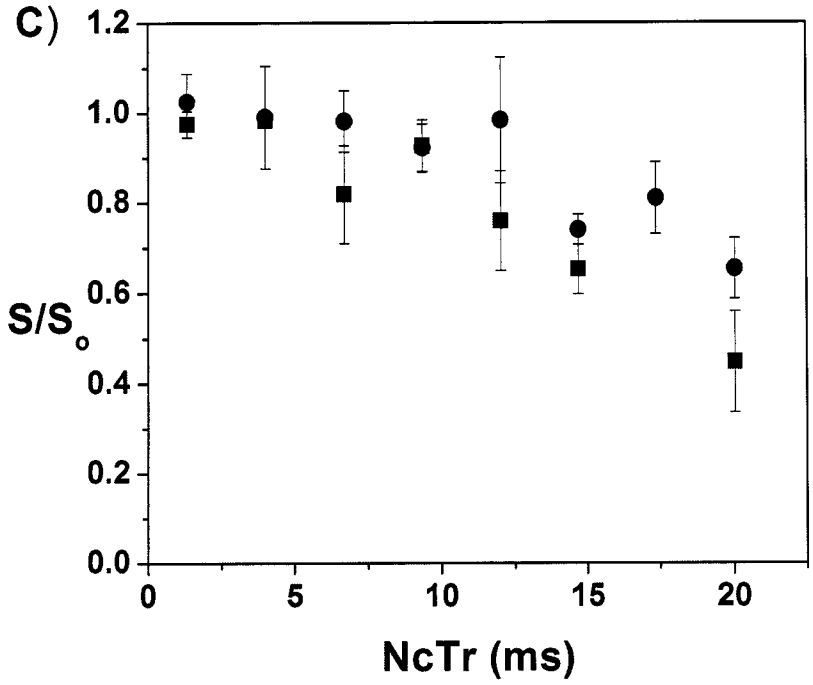

Figure 12C

Vita

Elizabeth April Louie

Education

June 2005 University of Washington, Seattle, WA
Ph.D., Chemistry

1993-1998 San Francisco State University, San Francisco, CA
Chemistry undergraduate and graduate coursework

May 1987 University of California Berkeley, Berkeley, CA
B.A., Physiology

Research Experience

1999 – present University of Washington, Seattle, WA
Structure determination of biomolecules using heteronuclear and homonuclear techniques in solid state nuclear magnetic resonance:

- Measuring long-range internuclear distances in DNA labeled with a trifluoromethyl group using ^{31}P-{^{19}F} REDOR NMR
- Determining torsion angles of membrane peptide using DQ-DRAWS, 2D-DQDRAWS
- Characterizing secondary structure of an amphipathic peptide on a charged surface
- Collect, process, and analyze experimental data
- Synthesis, purification, and preparation of biological samples, DNA and peptides
- Maintain, troubleshoot, and repair SSNMR probes, homebuilt spectrometers, and equipment

Research advisor: Gary P. Drobny, Ph.D.

1994 - 1998 San Francisco State University

- Studying the orientation and interaction of polar porphyrins and their iron complexes with micelles using NMR
- Synthesizing, purifying, and characterizing unsymmetrically substituted tetraphenylporphyrins and their iron complexes

Research advisor: Dr. Ursula Simonis

Teaching Experience

1998 - present University of Washington

- Graduate grader/teaching assistant: Undergraduate physical/biophysical chemistry, graduate quantum mechanics, graduate statistical mechanics
- Graduate teaching assistant: Undergraduate general chemistry labs and discussion sections

1996 - 1998 San Francisco State University

- Graduate teaching assistant: introductory and general chemistry labs
- Organic graduate assistant: Assist undergraduate organic students with use of instruments: FT-NMR, GC, FT-IR, and UV-vis
- Graduate grader: Organic chemistry, analytical chemistry, and general chemistry
- Participation in Math and Science Teacher Education Program (MASTEP) Teaching and Learning Workshops

Work Experience

1989 - 1998

- In-patient I.V. pharmacy technician at California Pacific Medical Center in San Francisco, CA and Seton Medical Center in Daly City, CA
- Out-patient pharmacy technician at University of California San Francisco Out-patient Pharmacy in San Francisco, CA

1981 -1989

- Medical records file clerk and birth certificate coordinator at California Pacific Medical Center in San Francisco, CA

Awards

- Ringold Fellowship, University of Washington (2002)
- Klaus A. and Mary Ann Saegebarth Fellowship, University of Washington (1999)
- Achievement Award, San Francisco State University (1998)
- Graduate Assistance in Areas of National Need (GAANN) Fellowship (1997)

- Student Research Competition, San Francisco State University (1997)
- Achievement Rewards for College Scientists (ARCS) Scholarship (1996, 1997)
- Women and Minority Participation in Graduate Education (WMPGE) Grant (1995)
- Florence Haimes Scholarship, San Francisco State University (1995)
- Summer Research Scholarship, San Francisco State University (1995)
- California Alumni Association Scholarship, University of California Berkeley (1983)

Publications

- Louie, E. A.; Stayton, P. S.; Drobny, G. P. "Solid State NMR Structural Studies of Peptide Adsorption on a Carboxylated Polystyrene Bead." (*in preparation*)
- Louie, E. A.; Cotten, M.; Drobny, G. P. "Using Solid State NMR to Determine Secondary Structure of Peptides in Lipids." (*in preparation*)
- Goobes, G., Raghunathan, V., Louie, E. A., Gibson, J. M., Olsen, G. O., Drobny, G. P. "A Redor Study of Diammonium Hydrogen Phosphate: A Model for Distance Measurements from Adsorbed Molecules to Surfaces." *Solid State Nucl. Magn Reson., 2005 (submitted)*
- Louie, E. A.; Chirakul, P., Raghunathan, V., Sigurdsson, S. Th.; Drobny, G. P. "Using Solid-State $^{31}P\{^{19}F\}$ REDOR NMR to Measure Distances between a Trifluoromethyl Group and a Phosphorothioate in Nucleic Acids." *J. Magn. Reson. 2005 (accepted).*
- Bower, P. V.; Louie, E. A.; Long, J. R.; Stayton, P. S.; Drobny, G. P. " Solid-State NMR Structural Studies of Peptides Immobilized on Gold Nanoparticles." *Langmuir* 21(7) 3002-3007, 2005.
- Olsen, G. L..; Louie, E. A..; Drobny, G. P.; Sigurdsson, S. Th. "Determination of DNA Minor Groove Width in Distamycin-DNA Complexes by Solid State NMR." *Nucleic Acids Research*, 31, 5084-5089, 2003.

- Vermathen, M.; Louie, E. A.; Chodosh, A. B. Ried, S.; Simonis, U. "Interactions of Water Insoluble Tetraphenylporphyrins with Micelle Probed by UV-visible and NMR Spectroscopy." *Langmuir*, 16, 210-221, 2000.

Posters and Presentations

- Biophysical Society Meeting (February 2005)

  Poster: "A Study of Secondary Structure of Peptides in Various Environments by Solid State NMR."
- Experimental Nuclear Magnetic Resonance Conference (April 2004)
- Poster: "Studying Biomolecules with Solid State NMR on Surfaces and in Biological Settings."
- Biophysical Society Meeting (February 2002)

  Poster: "Measuring Long-Range Internuclear Distances with a Trifluoromethyl Group in Biomolecules using ^{31}P-{^{19}F} REDOR."
- American Chemical Society National Meeting (August 1998)

  Poster: "The Orientation and Interaction of Polar Porphyrins and Their Iron Complexes with Micelles."
- Research Infrastructure in Minority Institutions (RIMI) Summer Research Conference (August 1997)

  Presentation: "The Design, Synthesis, and Characterization of Porphyrins with Polar Properties."
- California State University Research Competition (April 1997)

  Presentation: "Synthesis and Characterization of Sulfonated Tetraphenylporphyrins."
- American Chemical Society National Meeting (April 1997)

  Poster: "Synthesis and Characterization of Porphyrins Bearing Polar Substituents and Their Metal Complexes."
- American Chemical Society National Meeting (April 1995)

  Poster: "Characterization of Unsymmetrically Substituted Model Hemes by NMR Spectroscopy."

Affiliations

- American Chemical Society
- Biophysical Society

References

- Gary P. Drobny, Ph.D., Professor, Department of Chemistry at University of Washington in Seattle, WA, drobny@chem.washington.edu, 206-685-2052.
- Myriam Cotten, Ph.D., Assistant Professor, Department of Chemistry at Pacific Lutheran University in Tacoma, WA, cottenml@plu.edu, 253-535-7555.
- Joanna R. Long, Ph.D., Assistant Professor, Department of Biochemistry and Molecular Biology at University of Florida in Gainesville, FL, jrlong@mbi.ufl.edu, 352-846-1506.
- Matthew E. Merritt, Ph.D., Assistant Professor, Rogers NMR Center at Southwestern Medical Center in Dallas, TX, matthew.merritt@utsouthwestern.edu, 214-648-5863.